CRANFIELD UNIVERSITY

Chuanliang Guo

Effects of Turbulence Modelling on the Analysis and Optimisation of High-Lift Configurations

School of Engineering
MSc by Research

Master of Science
Academic Year: 2010 - 2011

Supervisor: Dr Evgeniy Shapiro

Dr Timos Kipouros

September 2011

CRANFIELD UNIVERSITY

School of Engineering
MSc by Research

Master of Science

Academic Year 2010 - 2011

Chuanliang Guo

Effects of Turbulence Modelling on the Analysis and Optimisation of High-Lift Configurations

Supervisor: Dr Evgeniy Shapiro

Dr Timos Kipouros

September 2011

ABSTRACT

Due to the significant effects on the performance and competitiveness of aircraft, high lift devices are of extreme importance in aircraft design. The flow physics of high lift devices is so complex, that traditional one pass and multi-pass design approaches can't reach the most optimised concept and multi-objective design optimisation (MDO) methods are increasingly explored in relation to this design task.

The accuracy of the optimisation, however, depends on the accuracy of the underlying Computational Fluid Dynamics (CFD) solver. The complexity of the flow around high-lift configuration, namely transition and separation effects leads to a substantial uncertainty associated with CFD results. Particularly, the uncertainty related to the turbulence modelling aspect of the CFD becomes important. Furthermore, employing full viscous flow solvers within MDO puts severe limitations on the density of computational meshes in order to achieve a computationally feasible solution, thereby adding to the uncertainty of the outcome. This thesis explores the effect of uncertainties in CFD modelling when detailed aerodynamic analysis is required in computational design of aircraft configurations. For the purposes of this work, we select the benchmark NLR7301 multi-element airfoil (main wing and flap). This flow around this airfoil features all challenges typical for the high-lift configurations, while at the same time there is a wealth of experimental and computational data available in the literature for this case.

A benchmark shape bi-objective optimization problem is formed, by trying to reveal the trade-off between lift and drag coefficients at near stall conditions. Following a detailed validation and grid convergence study, three widely used turbulence models are applied within Reynolds-Averaged Navier-Stokes (RANS) approach. K-ε Realizable, K-ω SST and Spalart-Allmaras. The results show that different turbulent models behave differently in the optimisation environment, and yield substantially different optimised shapes, while maintaining the overall optimisation trends (e.g. tendency to maximise camber

for the increased lift). The differences between the models however exhibit systemic trends irrespective of the criteria for the selection of the target configuration in the Pareto front. A-posteriori error analysis is also conducted for a wide range of configurations of interest resulting from the optimisation process. Whereas Spalart-Allmaras exhibits best accuracy for the datum airfoil, the overall arrangement of the results obtained with different models in the (Lift, Drag) plane is consistent for all optimisation scenarios leading to increased confidence in the MDO/RANS CFD coupling.

Keywords:

High lift devices, turbulent models, multi-objective optimisation, Tabu search, optimal quality

ACKNOWLEDGEMENTS

Firstly I would like to express my sincerest gratitude to my supervisors, Dr Shapiro and Dr. Kipouros for their continual advice, guidance and support throughout the past year. With their kind and patient help, I enhance the understandings on high lift flows and multi-objective optimisation quite a lot and broad the visions.

I would like to save my deepest gratitude for my family, especially for my wife Ying Cai, without their love and support, it would be impossible for me to finish my study in a foreign country for the whole year.

I also would like to deliver great thanks to Dr. Savvaris, Dr. Zhong for their stable support to me and all COMAC students.

I also wish to express my thanks to my friends for their assistance and encouragement.

Finally I would like to express my heartfelt thanks to my sponsor, COMAC Company and all the personalities involved.

TABLE OF CONTENTS

LIST OF FIGURES

LIST OF TABLES

LIST OF EQUATIONS

Chapter 1 Introduction

Multi-objective optimization is becoming more promising and realistic to aid the design optimization for high lift devices. In this study, an investigation of compatibility between three Reynolds Average Navier-Stokes (RANS) models and a Multi-Objective Tabu Search algorithm (MOTS) has been performed in terms of wall clock time and optimal quality.

The introduction begins with an exploration of the importance of high lift devices followed by a brief review of the history and classification of high lift devices. Flow physics are then discussed and a brief overview of the CFD investigations on high lift flows given. Optimizations of high lift devices are also introduced. The excellent capability of multi-objective optimization (MOO) on high lift devices design optimization shapes the objectives of the study along with consideration of the previous work [1]. Finally the case study NLR 7301 two element high lift configuration is introduced.

1.1 High lift devices in Aerodynamic design-history, classification and importance

1.1.1 Importance of high lift devices design

High lift systems are complicated and expensive to manufacture. According to [2], high lift systems account for about 6% to 11% of the total cost of production for a commercial aircraft. Such high expenses are mainly caused by:

1) The developing approaches, which include experiments and numerical computations, are highly expensive to apply;

2) The structure, which includes a number of actuation and support parts, is heavy and complex.

Moreover, high lift devices have a dominating effect on the field performance of aircraft during take-off and landing conditions. Figure 1 shows the requirements

of velocity and climb rate for a commercial aircraft based on the airworthiness regulation of FAR-25 in take off condition. As explained in [3], the take-off field length is defined as the total of ground roll distance which is required to accelerate from the resting position to the lift-off speed V_{LOF} plus an airborne distance to overfly an obstacle height of 35ft. According to the FAR, V_{LOF} has to be 1.1 times the minimum 'unstick' speed V_{MU}, which is defined as the minimum speed at which the aircraft can safely take-off with one engine inoperative. V_{MU} is not only a function of the aircraft maximum lift capability, but also can be limited by the usable angle of rotation which reduces the usable lift coefficient. Therefore, if V_{MU} is increased, the required ground roll distance inevitably will be increased, too. After lift-off, the next speed of interest is the take-off climb speed V_2, which must be achieved when the aircraft reaches 35ft height above the ground. V_2 must be greater than 1.2 times the minimum dynamic stall speed V_{Smin}, and greater than 1.1 times the minimum control speed V_{MC}. V_{Smin} is usually 0.94 times the stall speed in a 1g steady flight. Hence, V_2 must be greater than 1.13 times V_{S1g}, or in terms of lift coefficients: C_{Lv2} must be below $C_{Lmax}/(1.13)^2$. After take-off, the second segment climb begins when the undercarriage is retracted. According to the FAR, the minimum second segment climb-rate with one engine inoperative must be greater than 2.4% for aircraft with two engines (3.0% for aircraft with four engines) and the minimum speed must be V_2. Approximately the climb rate (CR) is a function of the thrust to weight and the lift to drag (L/D) ratio as defined by the following equation:

CR= Thrust/Weight -1/ (L/D) (1)

It is normal that a higher lift coefficient can be achieved with a higher flap setting which decreases the L/D and consequently climb rate simultaneously. High lift coefficient can reduce the ground-roll distance but reduced L/D can increase airborne distance. Therefore the aerodynamic optimization of the take-off configuration is aimed at finding the best compromise between lift capability and L/D efficiency to satisfy the requirements for both the takeoff field length and the climb rate.

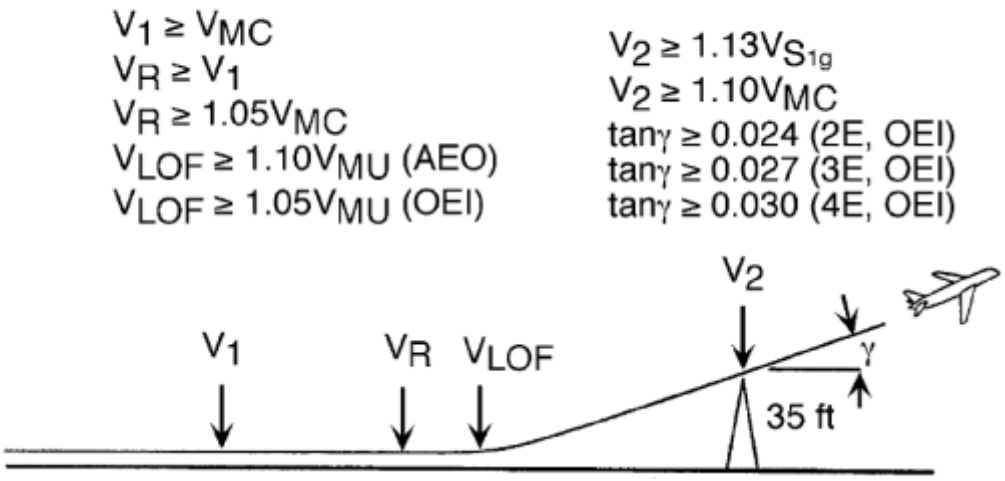

Figure 1 The requirements of commercial aircrafts in take-off condition [2]

Except for the direct influences on field performance, high lift devices have comprehensive impacts on the whole performance of aircrafts. High lift devices can affect the load capability, cruise performance, maintainability, and noise level which cover some most important aspects for the competitiveness of aircrafts. For example, high lift devices can affect cruise performance directly and indirectly. Firstly, the weight of high lift devices and the drag caused by flap kinetic mechanism faring have direct impacts on the cruise efficiency. On the other hand, the C_{Lmax} can affects the maximum take-off weight (MTOW) which inversely may present requirements to wing planform and hence affect the cruise L/D and sequentially cruise performance. Reference [4] shows that for a Boeing 777 class aircraft, 0.1 increments in maximum lift coefficient can save empty weight of 1400 lb. A 1.5% increase in maximum lift coefficient is equivalent to 6600 lb increase in payload at a fixed approach speed. A 1.5% increase in L/D at take-off condition equals to 2800 lb increase in payload or a 150 nm increase in range. Following dependencies were found in reference [5] for the impact of the high-lift capability on the total aircraft performance for a typical twin-engine jet transport aircraft such as A320 and B737:

- 5% increase in maximum lift leads to 12-15% increase of payload.

- 5% increase of take-off L/D leads to 20% increase of payload.
- 5% increase of *maximum lift in landing* configuration lead to 25% increase of payload.

From the data mentioned above it can be deduced that the effects of high lift devices on the aircraft are dependent on the size and range of aircrafts and clear significance of high lift devices range from small size aircraft to mega liners.

1.1.2 History and classification

Generally, high lift devices contain leading edge devices; trailing edge devices and main element. Figure 2 gives a brief schematic of a typical high lift configuration.

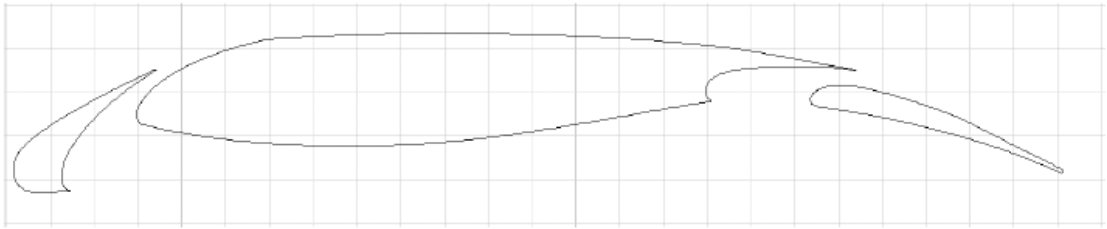

Figure 2 A typical high lift configuration with leading slat and trailing single slot flap

High lift devices began from slats. It is a variant of leading edge devices. The first slats were developed by Gustav Lachmann in 1918 and were patented by Handley-Page in 1919 and by the 1930s had developed into an automatically operated system driven mostly by hydraulic systems and were widely used in military aircrafts in World War II.

The first trailing edge flaps were used just before World War II, a result of efforts by Arado, a Germany aircraft company, and have been followed by increasingly complex systems made up of several parts with gaps in between, known as slotted flaps. [6]

Leading edge devices are used to increase the stall attack angle by postponing the occurrence of separation, and hence, increase the maximum lift coefficient. Trailing edge devices are used to produce higher lift by increasing the camber and length of chord of airfoil. It should be noted that the deployment of trailing edge devices reduce the stall angle of attack to some extent, owing to the high adverse pressure gradient over the trailing edge flaps. Figure 3 demonstrates the effects of leading edge devices and trailing edge devices on lift curves for a typical multi-elements airfoil [7]. It shows clearly that the leading edge devices can significantly increase the stall attack angle and reduce the CL slightly in linear range. Trailing edge devices can increase the CL significantly in linear range but reduce the attack angle of stall to some extent. It also can be found that multi-element slotted flaps are much more efficient than plain or split flaps in aerodynamics. However their application has been limited by their structural complexity.

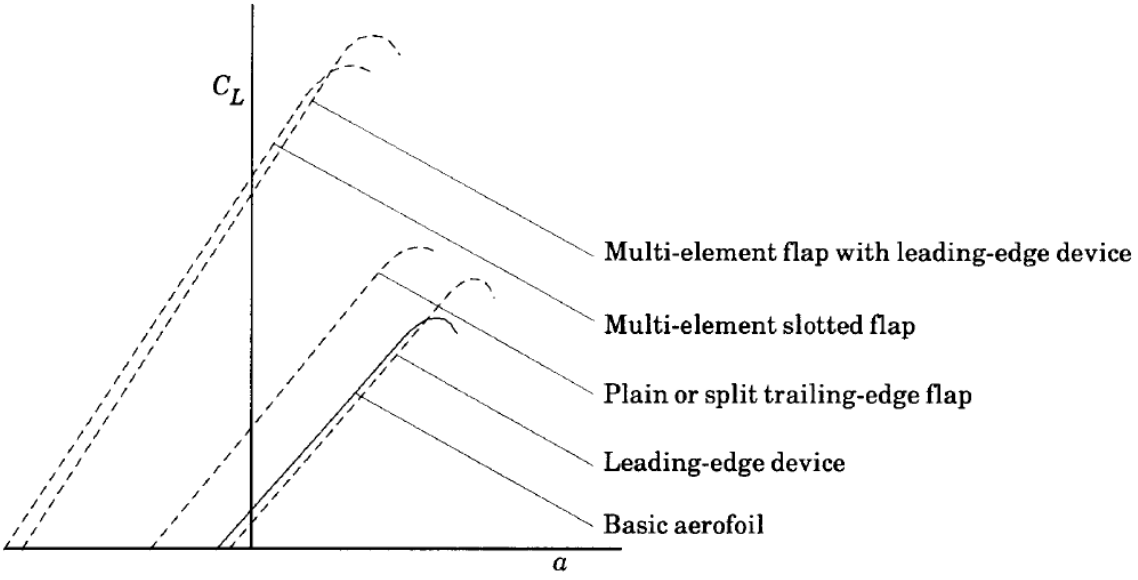

Figure 3 Typical effects of leading edge devices and trailing edge devices on lift curves [7]

The important parameters of high lift devices include chord ratio, deflection angle, gap and overlap. Figure 4 gives the definition of gap; overlap and deflection angles of high lift devices [8]. Normally the increasing of deflection

angle results in higher lift and low L/D. Figure 5 shows how the deflection angles of trailing edge devices affect the take off CL and L/D for a typical aircraft [9]. There are three settings of flap deflection angle in takeoff condition: 5 degree, 10 degree and 15 degree. When deflection angle increases, CL increases; L/D and stall angle of attack reduce relatively. So the trade off should be made between CL and L/D by designers to select proper deflection angle.

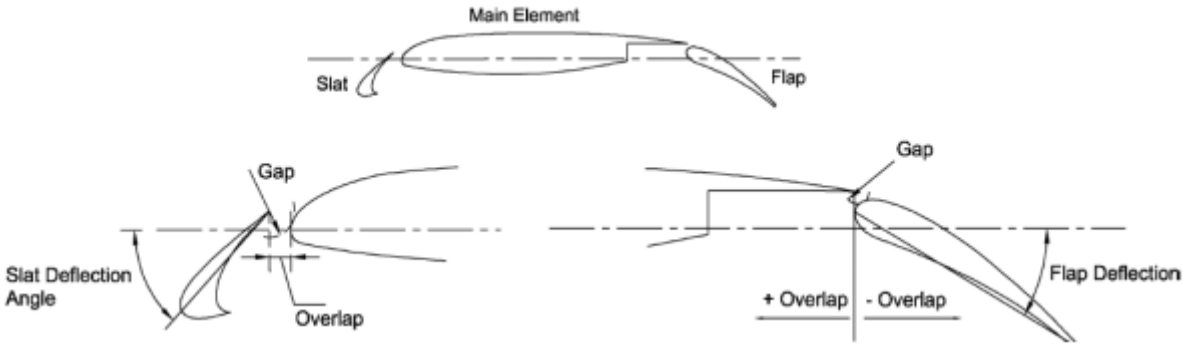

Figure 4 The definition of Gap, Overlap and Deflections for high lift devices [8]

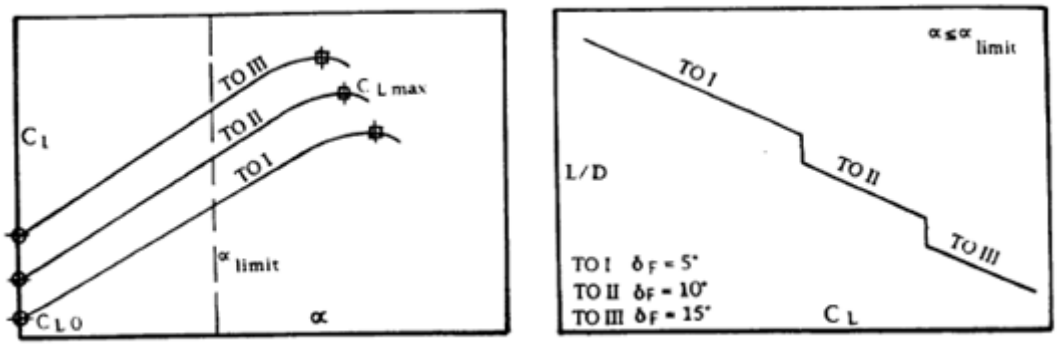

Figure 5 lift and L/D characters for a set of take-off configurations [9]

The effects of gap and overlap on performance of high lift devices are not only important but also difficult to capture. Changing the values of gap and overlap slightly can result in a significantly different aerodynamic performance for high lift devices. Thus the design of gap and overlap is an art in aerodynamics and requires careful verifications and validations. In [10], a wind tunnel study had

been performed on a low-speed single slotted flap high-lift configuration at a constant deflection angle of 40 degrees with the objective of reaching maximum lift coefficient. The results demonstrate that the configuration of the gaps which can reach a maximum CL is neither the biggest nor the smallest; rather it is a medium configuration that produces the maximum lift coefficient in which wake between flap and main element interplays reasonably to reduce the suction of peak and keep the flow attached over flaps.

The detailed classification of leading edge devices can be found in [9]. Current leading edge devices include Kruger flaps, slat and dropped leading edge devices. Kruger flaps can postpone the stall to higher attack angle but require a more complex structure to support the system. Slats have moderate aerodynamic performance and reasonable structure complexity, and can be actuated by a kinetic mechanism with less complexity and less weight compared with the Kruger flap system. Dropped leading edge is a new concept which can maintain the good aerodynamic performance such as high lift drag ratio, but its structure may be more complex and other factors may need to be considered, such as how to prevent the air leakage from lower surface to upper surface.

For commercial airliners, slats are more favourably viewed and are selected as leading edge device. The main aircraft supplier Airbus use slats for almost all Airbus aircrafts; another giant company Boeing has also selected slats as the leading edge devices for the latest B777 and B787 series despite having over thirty years' experience of Kruger flaps as leading edge devices.

Nevertheless, the probability of the revival of Kruger flaps may exist in the future. If natural laminar flow wing technology matures, Kruger flaps may become the only reasonable choice for leading edge devices for wings as only Kruger flaps do not affect the upper surface geometry quality, an unavoidable consequence of other leading edge devices such as slats.

Slotted flaps are the main variants of current trailing edge devices. At the early stages of aeronautics the split flaps and simple flaps were used frequently in aircraft design. Later the slotted flaps which include single slot flaps, double slot flaps and triple slots flaps were developed and used widely. Figure 6 shows deployed flaps for Airbus 340 aircraft and Boeing 777 aircraft. The full single slot flaps for Airbus 340, as well as inboard double slotted flaps and outboard single slotted flap for Boeing 777 aircraft, can be identified clearly. These two main trunk line aircrafts use slotted flaps.

Figure 6 The flap settings for Airbus 340(upper one) and Boeing 777 (lower one)

More slots produce higher C_{Lmax}, as well as higher complexity. Figure 7 shows an 8 element flap system that can reach a very high C_{Lmax} [11]. The model is at 42° angle of attack, the angle for maximum lift. Pressure distributions are theoretical. They were made at α = 36° to correspond to local angle of attack of the AR = 6 wind tunnel model. Theoretical CL of ensemble is 4.33, which is much higher than that of the single element. Nonetheless, is too complex to put into real production.

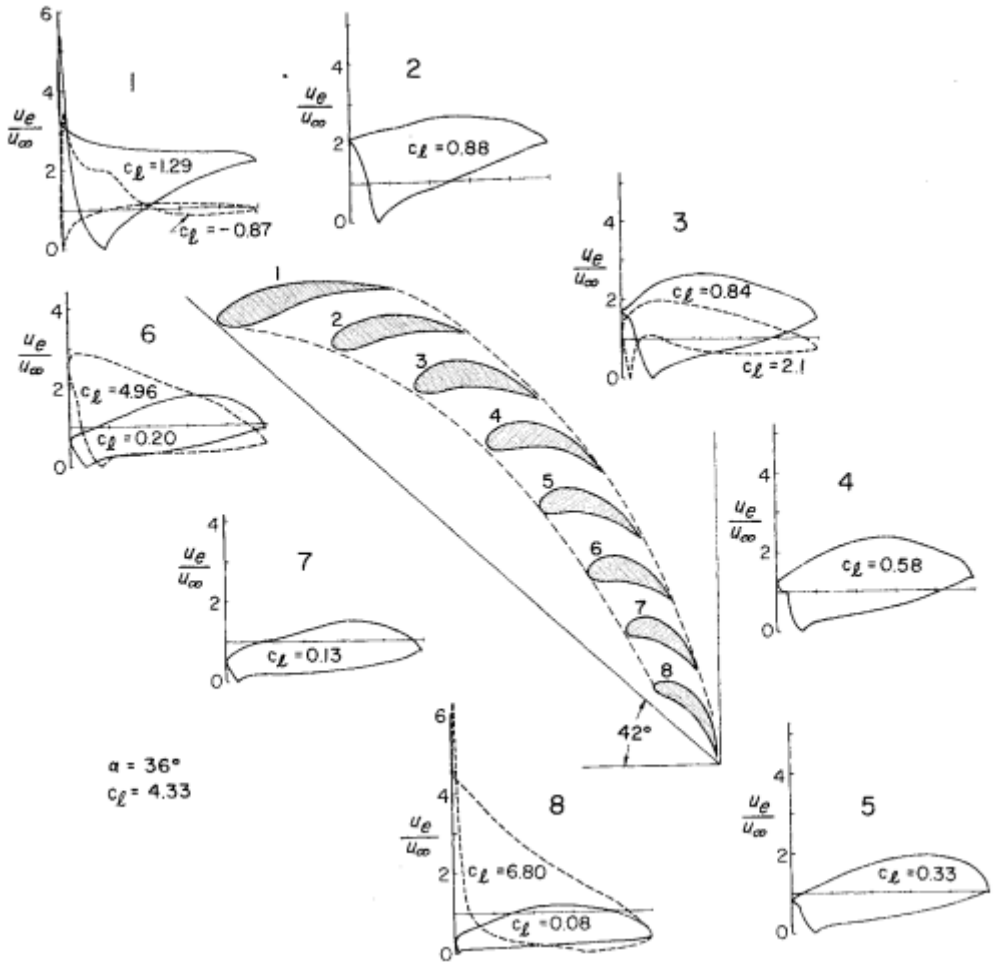

Figure 7 Handley Page's eight-element airfoil modified from an RAF 19 section [11]

At present aircraft companies do not only pursue the aerodynamic performance but also consider other aspects such as complexity, weight and maintainability. For aerodynamic efficiency, a philosophy that is “not better than necessary “is

held for aerodynamic performance by designers. One tendency for developments for future high lift devices is the simplification of trailing edge devices. Figure 8 shows the design evaluation of trailing edge systems for both inboard high lift configuration (the upper one in the pair on the left side) and outboard high lift configuration (the lower one in the pair on the left side) for Airbus and Boeing/Douglas. It can be found that the single slotted flap system is the most favourable choice for current Airbus aircrafts and for Boeing/Douglas aircrafts to be developed.

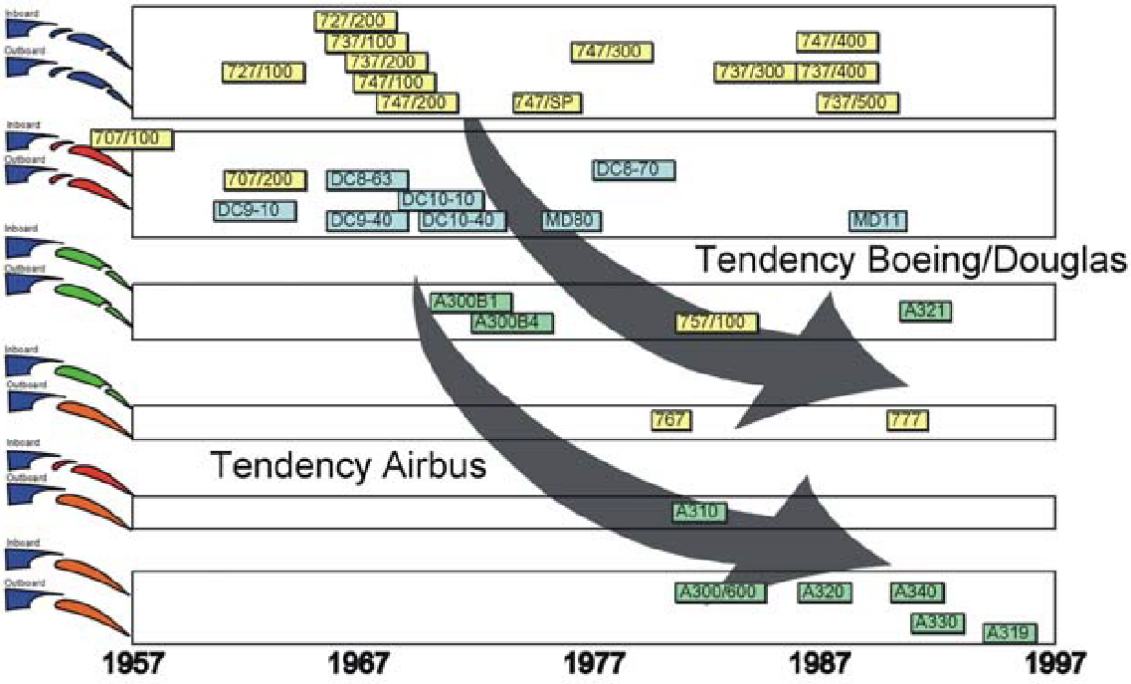

Figure 8 Design evolution of high-lift wing trailing edge systems [9]

New concepts have been developed recently based on the principles of reducing complexity. Dropped hinge flaps system is a newly developed flap concept which has been adopted by Airbus 350XWB aircraft [12]. This kind of flaps system is not preeminent in aerodynamics but very simple to manufacture and maintain, by using a relatively simple mechanics to support and drive. Fig 9 depicts the comparison between dropped hinge flaps and traditional track kinematics flap. It can be seen that the track of dropped hinge flaps is much more regular which will make the manufacture and maintenance easier.

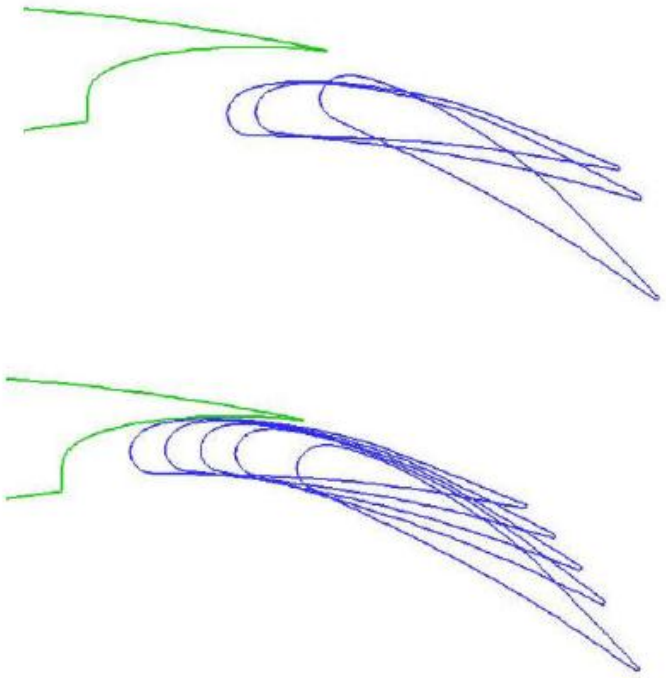

Figure 9 Comparison between track kinematics (upper one) and dropped hinge (lower one) [12]

Another new technique of high lift devices is the usage of collaborative moves between spoilers and flaps. Recent research has identified that the collaborative moves will benefit the lift without damage to the drag. It is reported that this technology has been applied in the Airbus 350XWB project. [13]

Except these conventional trailing edge devices, powered high lift system is an alternative concept to reach high lift. Powered high lift devices generally use the high energetic air flow withdraw from engine to shape the flow around the wing instead of the flaps. Considering its complexity, reliability and effects on thrust, powered high lift devices are sometimes used in military transporter but little used in civil aircraft. Global master C-17 military transporter is an example of powered high lift devices.

The developments of high lift devices can be summarized as following:

- Conventional concepts that include leading edge devices and trailing edge devices have experienced different concepts and are still developing.
- For leading edge devices, it seems slats are the most favourable choice for commercial aircraft. But the revival of Kruger flaps may come if nature laminar flow wing technology is matured.
- For trailing edge devices, the tendency of simplification of flaps is inevitable. The philosophy that is “not better than necessary” dominate the design for high lift devices at present.
- Some new concepts such as drop hinged flaps and collaborative moves for flaps and spoilers have been developed.

However, the development of qualified high lift devices for aircrafts is far from straightforward work owing to their complex flows.

1.2 Flow physics- flow structure and challenge

High lift devices are comprised of multi-elements such as leading edge device, main element and trailing edge device. A good high lift device should utilise favourable effects of the interactions between different elements. It is these favourable interactions that make multi-element wings reach higher lift. A.M.O.Smith identified five favourable effects inherent in a slotted configuration of a 2-D high lift airfoil and stated that in reference [11]:

“(a) The presence of the downstream elements, e.g. wing relative to slat or flap relative to main wing, induces considerably greater circulation on the upstream elements,

(b) The trailing edges of the forward elements are in a region where the local velocity is appreciably higher than free-stream and this, therefore, reduces the

pressure-rise to be negotiated by the boundary layer on the upper surface of the upstream elements,

(c) The presence of the upstream element reduces the peak suctions on the downstream element,

(d) The development of the wakes of the forward elements -mostly in an accelerating flow as a result of the inviscid flow field around the slotted multiple aerofoil layout - occurs off-the-surface of the rear elements and hence in a more efficient manner than if it was occurring on the surface,

(e) Each new element starts out with a fresh boundary layer at its leading edge which, being relatively thin, is better able to withstand a given adverse pressure gradient."

On the other hand, multi-element interactions cause the flow physics more complications than that of a single element. Figure 10 shows typical flow characters of a 2-D multi-element airfoil. It can be found that confluent wake, cover separation which cannot be found in single element airfoil and trailing edge separation dominate the flow. Confluent flows which are formed by the wake of forward elements significantly increase the expansion and irregularity of viscous flow over the rear elements. Cove separations are also difficult for the prediction of the flows. Firstly cove separations contribute their wakes to form confluent flows; on the other hand the separation their selves are difficult to simulate and predict.

In addition, the continuous acceleration on leading edge will produce suction peak and great adverse pressure gradient; this will cause the laminar bubble separation owing to the fact that laminar boundary layer is easier to separate than turbulent flow. In more serious conditions on the leading edge surfaces of heavily loaded slats transonic flow can easily be found with Mach number over 1 and cause shockwave and shockwave/boundary interactions.

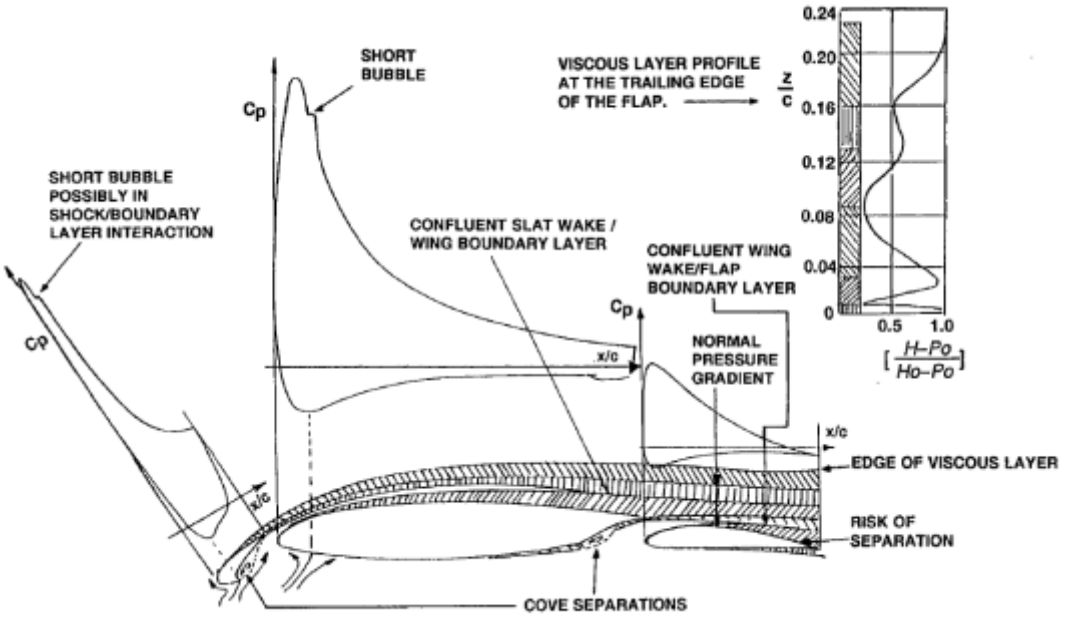

Figure 10 The flow character of a typical multi-element airfoil [14]

The 3-D high lift flows are even more complex. Except for the complex characters of 2-D high lift flows, complexities of 3-D high lift wings mainly arise from reasons listed below:

1) The spanwise flows on 3-D wing surfaces affect the confluent flow and cove separations with even different mechanisms compared with 2-D flows.[15]

2) The interference from other components of aircraft such as fuselage and nacelle and pylon introduce much more complex flow backgrounds compared with 2-D flow; which inevitably affect the viscous behaviour of the trailing edge flaps.

3) In 3-D wings high lift devices are normally of part span. The part span flaps shed a strong vortex at the outboard end and cause the effects on the flows nearby.

Figure 11 shows an experimental investigation of high lift wings on a BAE aircraft in landing condition.[16] It can be seen that the 3-D effects include the

transverse flows and the interferences from fuselage are very clear; these 3-D phenomena affect the flows over flap and cause the flow streamlines more irregularities. Experimental investigations have been applied to a complete commercial aircraft configuration with high lift devices. [17] Flow visualisation results were achieved to enhance the understanding of 3-D high lift flows. Figure 12 presents a picture of the oil visualization on this high lift configuration with nacelle and pylon assembled [17]. The vortices arisen from nacelle and wing body conjunction on flap area can be found clearly changing the direction and magnitude of the velocity and making the flows in front of the flap more irregular and the confluent flows over flap more complicated, affecting the pressure gradient of boundary layer of flap and reshaping the style of separation at the trailing edge of flap.

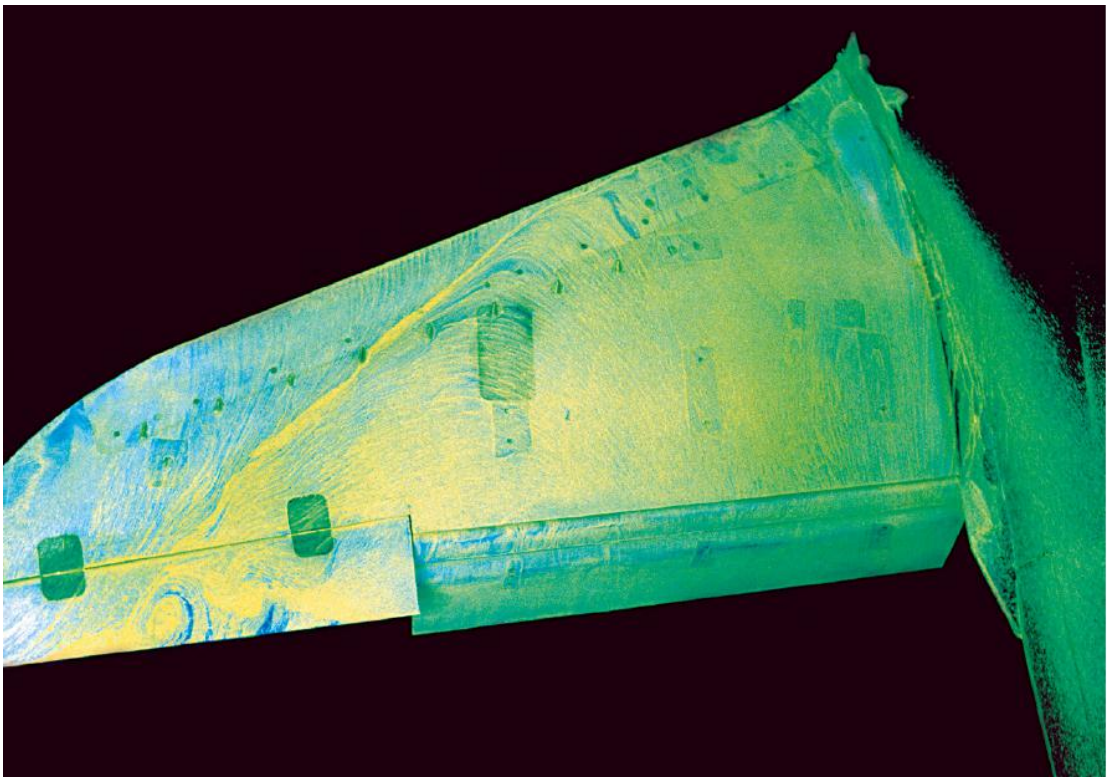

Figure 11 Surface oil visualization on a 3-D wing high lift configuration [16]

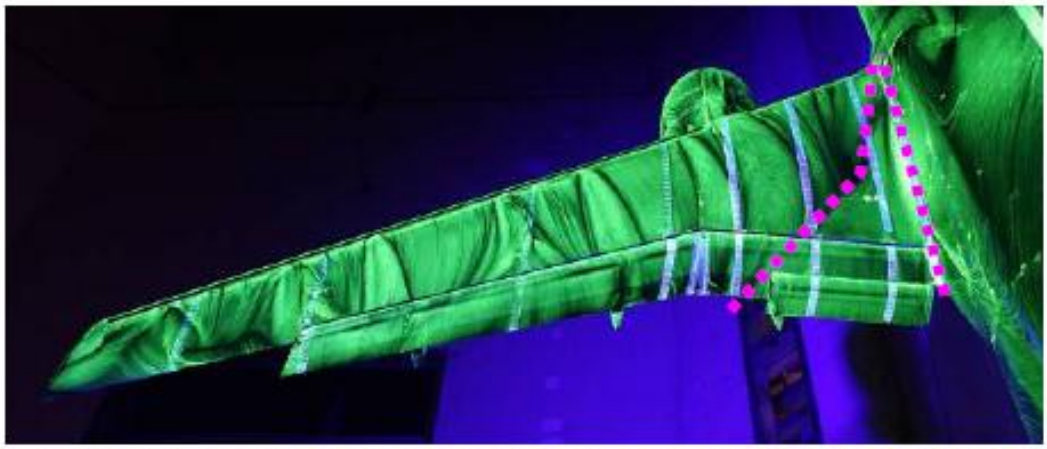

Figure 12 Surface flow pattern at post-stall conditions (V=60m/s, α=21°) [17]

For both 2-D and 3-D flows, the complexities of high lift flow are from viscous flows, which are much more sensitive and complex than inviscid flows. Typical viscous flow phenomena of high lift devices include:

1) Laminar boundary layer; turbulent boundary layer and the transition between them. They are difficult to predict and have significant impacts on the high lift aerodynamics.

2) Laminar bubble separations and turbulent separations. It is really difficult to predict these unstable flows, especially turbulent separations which are caused by adverse pressure gradient.

3) Confluent flows. They are combinations of turbulent boundary layers of forward elements and separation flows. These flows are irregular and the interactions between layers are disordered and non-constant. The shear stress characters of this flow are very difficult to predict.

These viscous high lift flows are sensitive and more locally dependent. They are easier to be affected by some variables such as Reynolds number and M number. To obtain a good understanding of complex high lift flows, high

requirements should be presented on high fidelity computational calculations and experiment techniques.

1.3 State of the art – computational and experimental studies – examples

The complexity of the high lift flow physics makes it a most challenging area in aerodynamic design. Current approaches investigating high lift flows are wind tunnel experiment and computational fluid dynamics（CFD）simulations.

Wind tunnel experiment is the conventional approach to investigate high lift flows. It is an actual physical simulation of flows on ground. Within wind tunnel experiments, the model should be manufactured to represent the real shape of high lift devices; supporting systems are necessary to fix the model in the test section hence the corrections for the interferences caused by supporting system should be applied to final results. Moreover, wall interferences should also be corrected. During the test, Mach number should be accurately simulated and Reynolds number should be setup as close as real fight configurations.

One difficulty of wind tunnel experiment is the simulation of flight Reynolds number, which has the most impact on the viscous behaviour of boundary layer. Most current wind tunnels are conventional ambient pressure facilities which cannot simulate the flight Reynolds number; it is difficult for them to predict accurately the aerodynamic characters such as stall behaviour for high lift devices. For these wind tunnels it is necessary to apply scale effects corrections which need high level experiences yet simultaneously introduce the uncertainties. Only few high Reynolds number wind tunnels such as national transonic facility (NTF) in USA and European transonic wind tunnel (ETW) in Europe can simulate the full scale Reynolds number of flight. But the utilization of these facilities is limited owing to the very high running cost.

Computational fluid dynamics (CFD) is a promising tool to research high lift flows. It uses the numeric technology to simulate the high lift devices in a

computer corresponding to the real flight condition. Compared to wind tunnel experiments, it is cost and time effective and can reduce the time and cost significantly for developing high lift devices.

In industries, wind tunnel tests and CFD calculations are combined to make clear the understanding of high lift flow. CFD solvers are widely used in the early stage design phase and wind tunnel experiments are more likely to play roles of validation. Figure 13 shows a typical design process for the high lift design of an Airbus megaliner civil aircraft [18]. It can be found that 2-D and 3-D CFD solvers are used to design the high lift devices and wind tunnel tests are used to design and verify the concepts and produce the data base of high lift devices.

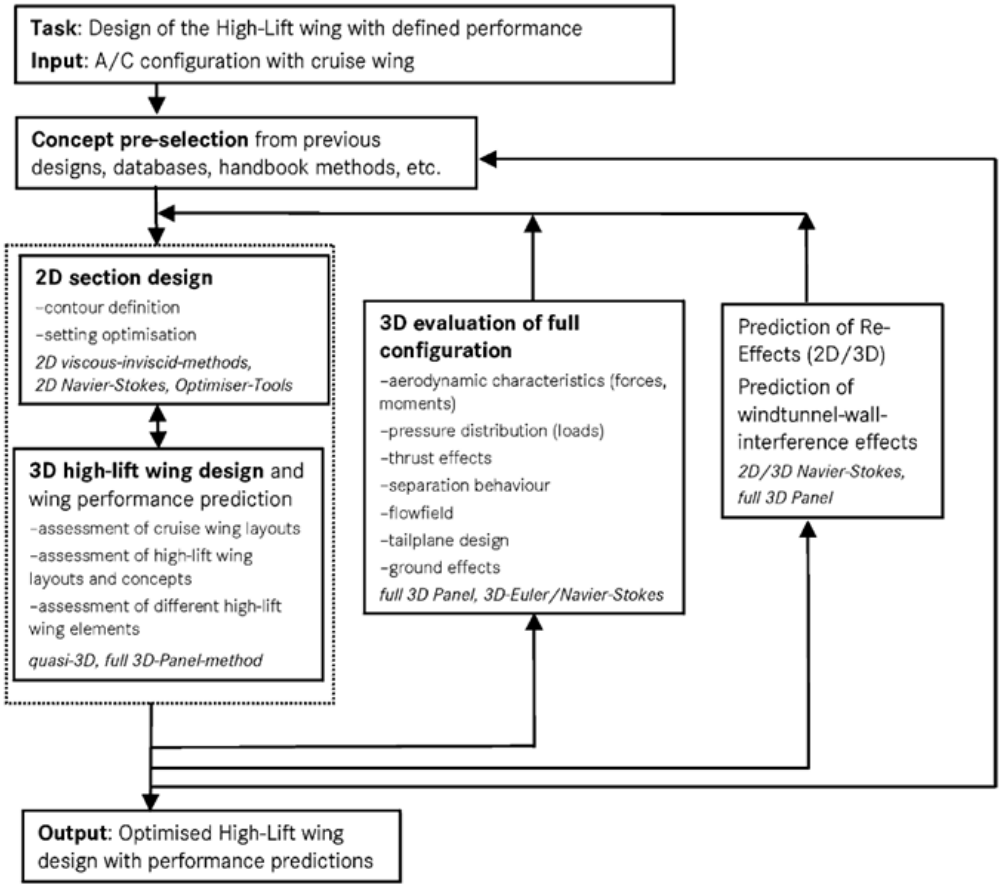

Figure 13 Sequence of the CFD-based high-lift design process [18]

Initially CFD methods served as analysis tools. At present they have become the main design tool for high lift devices and are responsible for most of the design works, owing to their increasing ability for the prediction of flow physics and availability to use. Figure 14 shows data from Boeing that illustrates the clear reduction in tested numbers of wings in the past thirty years owing to the development of CFD.[19]. It is shown that the wings needed to be tested in wind tunnels are reduced from 77 at the end of the 70s to 10 at the end of the 90s and maybe 5 in the coming years. The reduction in wind tunnel testing is converted to CFD.

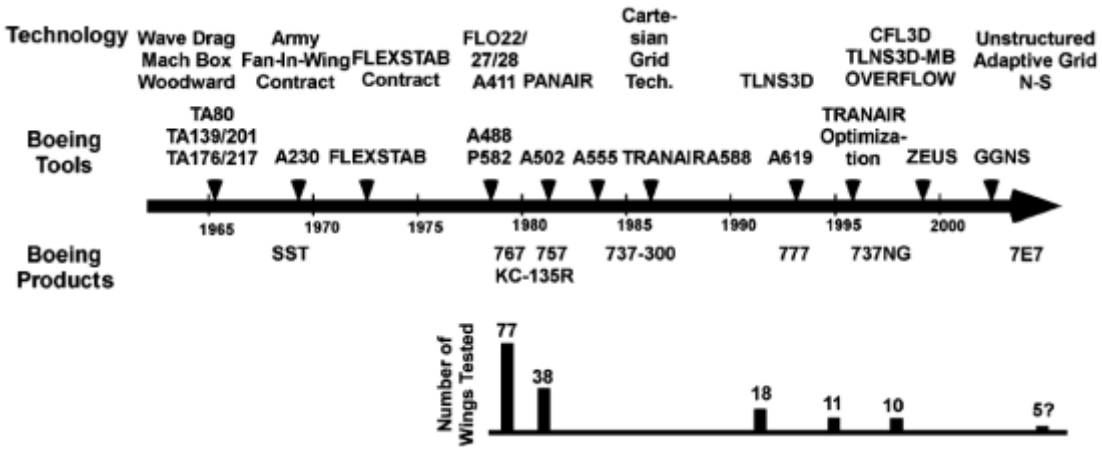

Figure 14 Effect of CFD on configuration lines wind tunnel development testing [19]

The next chapter offers a brief overview of the research of CFD on high lift devices according to 2-D cases and 3-D cases.

1.3.1 Computational simulations

Due to the importance of the high lift devices for the overall performance of aircraft, there have been great efforts in the investigation on high lift devices using CFD significant achievements have been reached.

Two aspects contributed to the progress made. The first is the development of turbulent models. As introduced in [15], the method for dealing with high lift flows experienced several stages listed below:

1. Coupled attached-flow methods;
2. Coupled separated-flow methods;
3. Navier-Stokes (N-S) methods;
4. Design and optimisation methods.

Navier-Stokes methods become the most used owing to its robustness and reasonable capability in current. One equation turbulent model Spalart-Allmaras is a routine tool for design engineers. Two equation k-w models are also widely used by industries and academies. The k – w model is increasingly considered as a viable alternative to the one-equation model because it provides better representation of the physics, in particular for shockwave-boundary layer interactions [20].

Recent developments of LES and multi-objective optimization have enhanced the ability to predict high lift flows and achieve optimised high lift designs. LES is considered a reasonable turbulence model for the computation of farfield flows, [21] but it is still not widely used owing to its higher computation cost and lack of modelling of small dimensional turbulent flows.

The developments of the computational hardware have also contributed strength to the predictions of high lift flows. The capability of the simulations on high lift devices has been strongly enhanced by the application of significantly increasing high performance computers. Considering time improvement and cost effectiveness, CFD has been applied widely in aerodynamic design and played a more important role than ever in the design for high lift devices.

In 2-D conditions, CFD has established solid reliability to predict high lift flows before stall in 2-D cases. Surface pressures, skin friction, lift can be predicted reasonably well before the stall [22]. Figure 15 and Figure 16 show the comparison of pressure coefficient and velocity profile between computations and experiments respectively for GA (W)-1 two element airfoil configuration at a

low attack angle of 4 degree.[23] In this case, Mach number is 0.15; Reynolds number is 0.62 million. The numerical calculations were applied by Menter model and Spalart-Allmaras (S-A) model. It can be found that two turbulence models have similar capability to predict high lift flows; agreements of Cp between experiments and computations are reasonable good in Figure 15 where most differences of Cp are less than 0.1. Figure 16 shows that prediction of velocity is generally good on trailing edge stations of main element and flap where confluent occurs. It can be seen the main features of confluent have been captured.

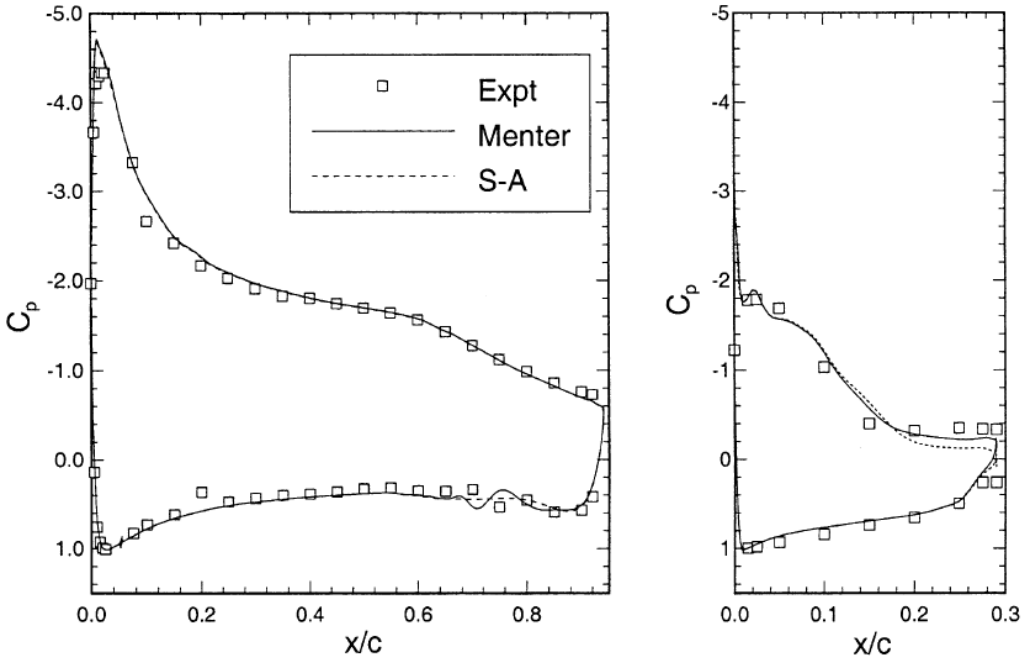

Main airfoil flap

Figure 15 Pressure distributions for the GA(W)-1 airfoil, from Godin et al. [23]

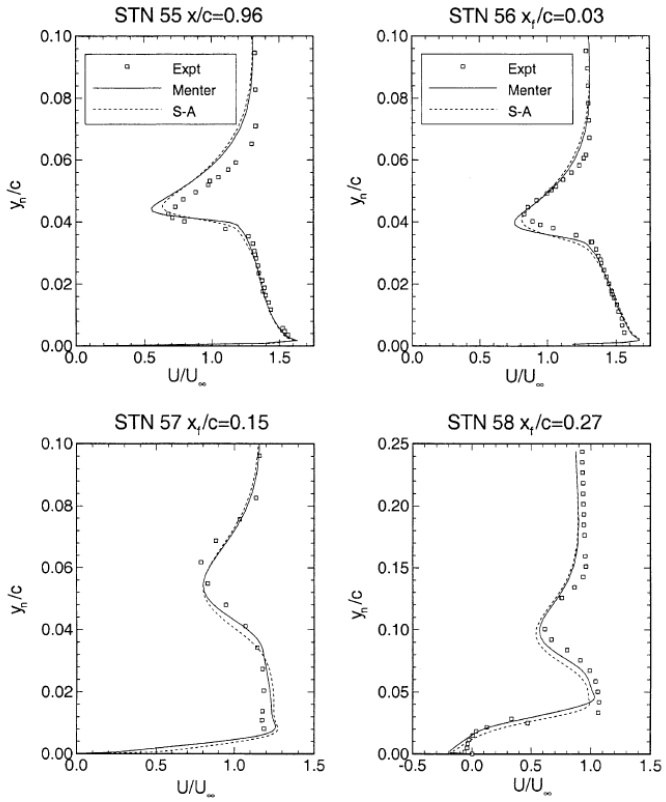

Figure 16 Velocity profiles for the GA (W)-1 airfoil, from Godin et al. [23]

Referring to the integrated force coefficient as CL, CFD express excellent ability for prediction on CL before stall in 2-D conditions. Figure 17 depicts the simulation results on NHLP-2D high lift airfoil; the flow conditions were defined as Mach number0.2, and Reynolds number 3.52×10^6. A curve of CL vs attack angle had been gained and was compared with experiment results; agreements of CL and CD between experiments and computations of S-A model can be found. SST model and EASM model are similarly close with the differences less than 0.05 in linear range.

Referring to the prediction on CD, the ability of CFD is not as reliable as that on CL. Figure 17 presents the NHLP-2D case, where the agreements between simulations and experiments are reasonably good with differences of about 5% before stall. But in references [22], a factor of 2-3 which represents the times of magnitude by simulated CD over tested CD are common in some cases. The difficulties of the prediction on CD might arise from these aspects:

1. CD is calculated by integrating the skin friction force and pressure force; this means it is highly sensitive to the density of grids and tends to produce a substantial discrepancy. In [22] it shows that cell numbers of at least 90000 are necessary to have an accurate prediction on drag for 2-D high lift configuration.

2. The simulations of the boundary layer and wake flow by different turbulent models are still insufficient. The mathematic equations representing boundary layers characters used in turbulent models are still ideally setup and cannot cover all the realistic flows exactly.

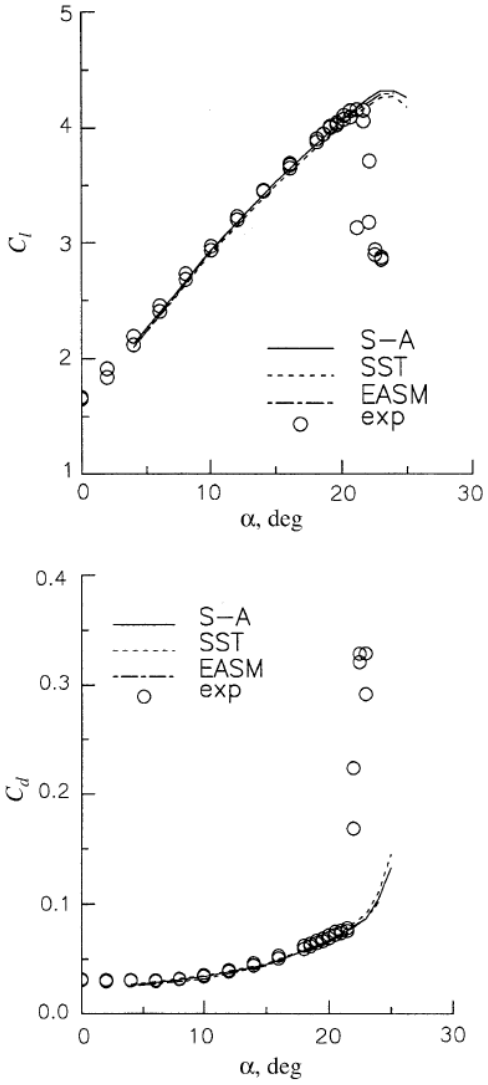

Figure 17 The integral force of NHLP-2D three element airfoil [24]

The biggest challenge of 2-D high lift flows is the prediction of stall and after. In this range flows are dominated by strong separations and the wakes from upstream parts are unstable and highly interplayed and currently used CFD methods are still lacking in accuracy to capture them reliably. This insufficiency can also be clearly observed in Figure 17 by checking the discrepancy after stall between simulation results and experiment results which may become hundreds times greater than in linear range.

On the prediction of high lift flows in 3-D conditions, RANS methods are still the most dominant. Owing to more complex flow physics and higher requirements of the computational hardware, the simulations of 3-D high lift flows are more difficult than for 2-D flows. It had been noted that for 3-D flows, the discrepancies between RANS simulations and experiments increase with the angle of attack. As a result, RANS simulations are more likely to be used as a means to improve the physical understanding rather than as a design tool in the optimization procedure. [21] In fact, nowadays it is possible to use RANS models to get the accurate CL and CD for some 3-D configurations by using high quality mesh with adequate cell numbers. This conclusion can be found in Drag prediction workshop III and Drag prediction workshop IV. But it has also been noted that it is neither practical nor necessary to predict CL and CD the same level in accuracy with experiments because of the giant computational cost and time consuming and the strategy of using CFD to capture the accurate increments between concepts can fulfil the requirements of aircraft design well. [25]

Recent significant progress from the diligent efforts of industries and academics have resulted in the completion and launch of EU projects EUROLIFT, EUROLIFT II and the German national project MEGAFLOW. In U.S.A, the first AIAA High lift Prediction workshop has been started. These projects promote the design capability for high lift devices and significantly strengthen the understanding of 3-D complex flows.

In 3-D conditions generally, current CFD methods have strengthened their capacity to capture the main flow features and can identify the increments of different configurations. However accurate prediction on high lift devices is still dependent on the complexity of the configurations. For simple configurations it is reasonable for CFD to predict accurately. One example is the prediction on the AFV model which was tested in ONERA F1 wind tunnel and shown in Figure 18, the flow conditions of the case were defined as Ma 0.20 and Re 2.8×10^6 with the configuration of sweep angle 40 degree and flap deflection 20 degree; the comparison of lift and drag coefficient between CFD results and experimental results are presented in Figure 19. Transition has been simulated in this case by elsA Turbulent (k-l) and elsA+Transition models developed by ONERA [26]. It can be found that the lift and drag in linear range agree quite reasonably in magnitude and pattern between simulations and experiments. For a more complex configuration, the trap wing configuration which was used as the datum model for 1st AIAA high lift prediction work shop shown in Figure 20. An investigation has been done with the Mach number 0.2 and Reynolds number 4.3 million, the comparison of pressure coefficient which is shown in Figure 19 notes that the pressure coefficient can be fairly accurately predicted; lift and drag have generally good agreement with experiment data before stall, see Figure 21 [27]. For more realistic configuration such as the KH3Y model, which was selected in EUROLIFT II project shown in Figure 22, the comparison of this configuration between computation and experiment on the lift and drag polar curves had been performed corresponding to a free-stream Mach number M=0.176 and a Reynolds number of 1.33 million. It can be found that even in linear range lift was obviously under predicted and drag levels were over predicted. These examples clearly demonstrate that the accuracy of prediction decreases along with the increasing of configuration complexity. Nevertheless, the effects of the configurations difference can be identified clearly by the computations [28].

Figure 18 The AFV model in ONERA-F1 wind tunnel [26]

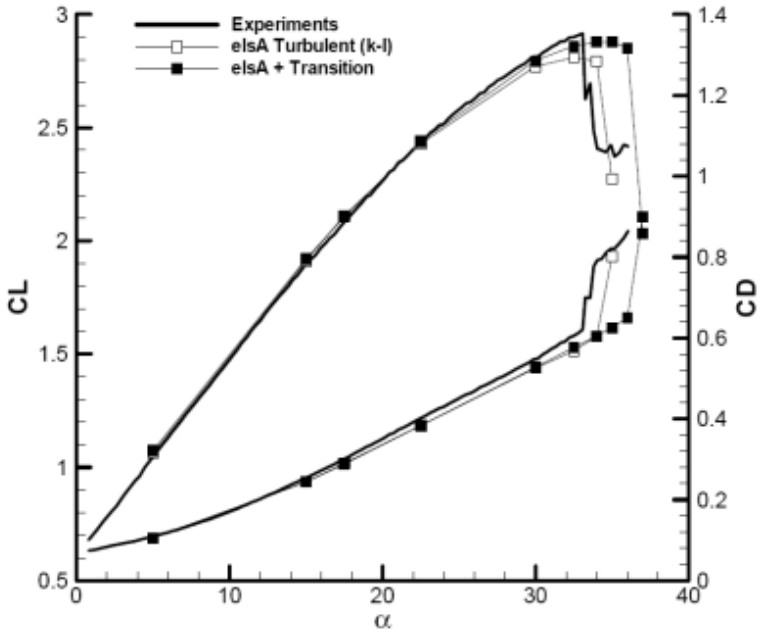

Figure 19 Comparison of ONERA CFD results with experiments for AFV model [26]

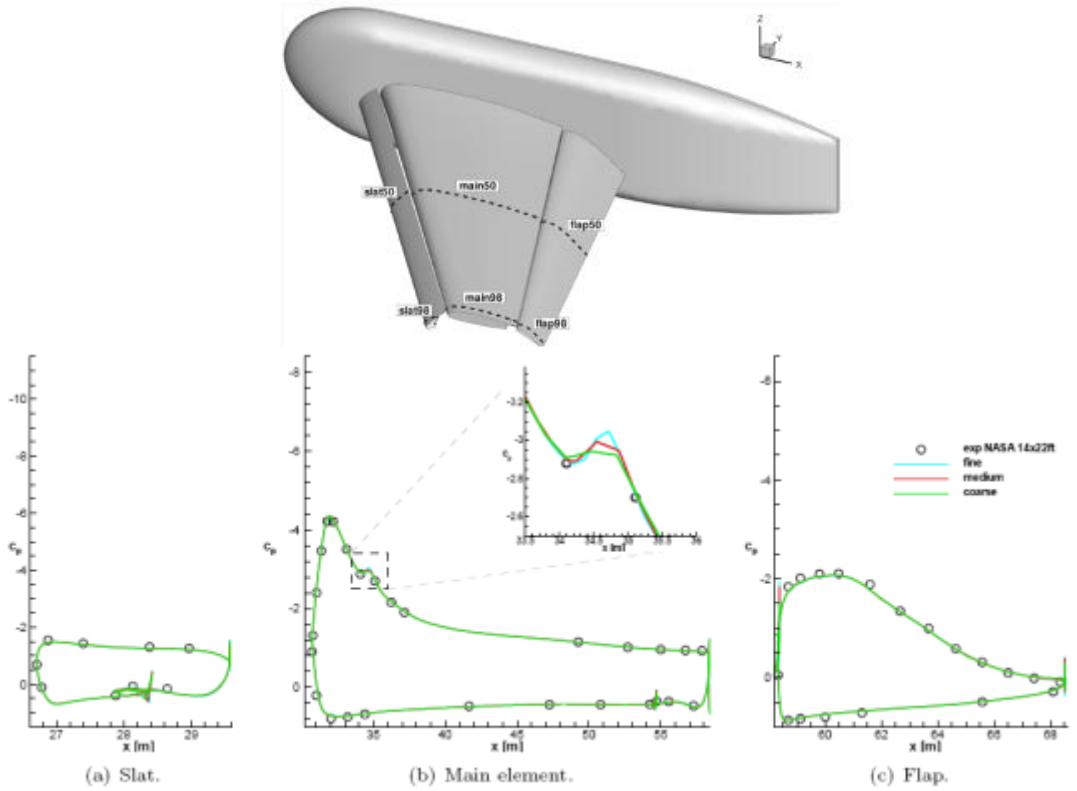

Figure 20 Surface pressure coefficient for computations on solar grids at alpha=13 deg, n=50% for trap wing model [27]

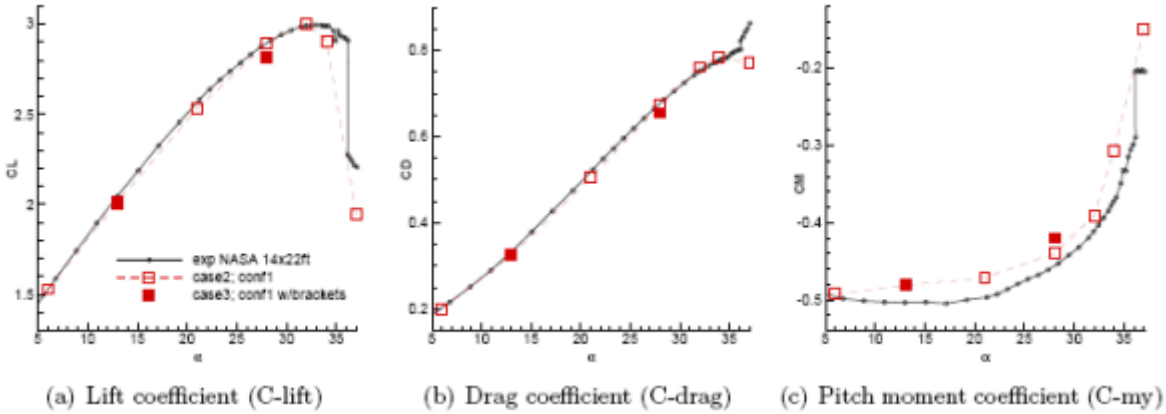

Figure 21 Angle of attack sweep of CL, CD and Cm for trap wing [27]

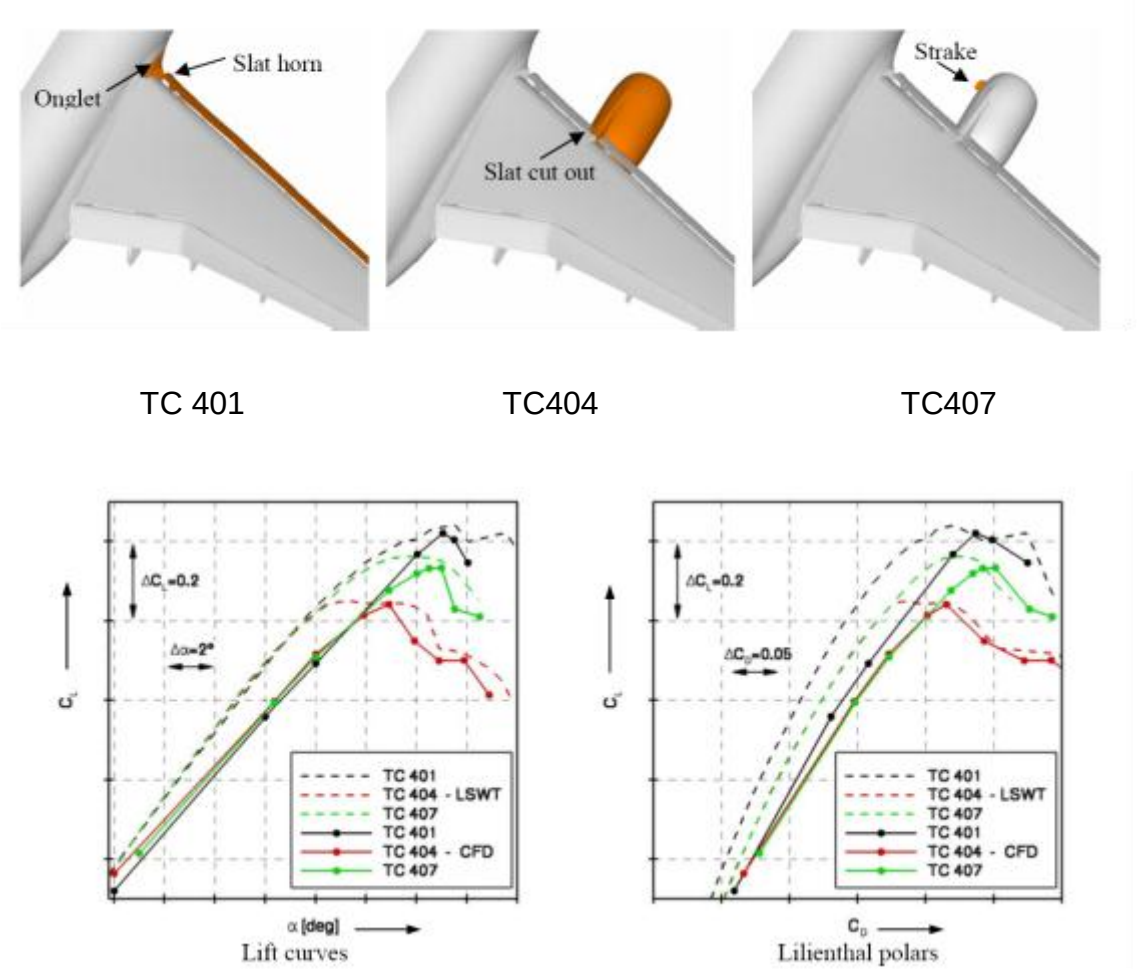

Figure 22 Comparison computed and measured lift curves and polars for three configurations for KH3Y model [28]

Similarly with 2-D cases, the prediction at stall and after is still inconsistent for 3-D conditions due to the extreme complexity caused by severe separations spread from trailing edge even to the whole upper surface of elements. CFD tools are still lacking capability to get reliable results in this area owing to insufficient modelling of turbulence behaviour for viscous flows. It can be clearly found from Figure 17 and Figure 22 that the discrepancies increase significantly at stall and beyond for both lift and drag.

It is impossible to make quantitative prediction of separation flows. Hirschel suggested five hypotheses for the failure of statistical turbulence models in predicting separated flows [29]:

1. Turbulence models do not sufficiently consider the flow topology

2. Transition phenomena are not properly taken into account in turbulence models

3. Role of dynamic phenomena, as for example vortex shedding, may restrict the applicability of turbulence models

4. Influence of three-dimensional effects in the so-called two-dimensional experiments with strong separation is not clear

5. The question whether it is allowed to apply turbulence- model constants and boundary conditions, experimentally obtained from attached 2D flows, to attached and separated 3D flows has not been verified systematically.

The bottlenecks may also be from RANS models themselves. As noted by Lindblad and de Cock [30], turbulence modelling becomes more difficult when strong adverse-pressure gradients are present in the flow field.

Referring to the grids for 3-D computations, the requirements of cell numbers are significantly increased because the complexity of the geometry and flow features requires time consuming pre-processing work to generate grids of sufficient quality. Typical grid sizes of Navier – Stokes calculations for 3-D high-lift configurations are in the order of 10 – 20 million grid points [21].

In general, regarding the computation ability of CFD, following conclusions can be made:

1) For 2-D cases, pressure, lift, skin friction can be reasonably predicted and velocity profiles can be captured with normally good accuracy before stall.

2) For 3-D cases, the prediction quality is dependent on the complexity of configurations and flow features: for simple configuration the lift and drag can be predicted well in linear range; for complex configuration, the lift and

drag is difficult to predict even in linear range. However, configuration difference can be clearly identified by CFD.

3) RANS methods are the widely selected turbulent models to predict 2-D and 3-D high lift flows in current. One equation model Spalart-Allmaras and two equation models K-ω and K-ε are routinely used.

4) Referring to the grids, for 2-D case: both structured grids and unstructured grids were used and could predict reasonable results. Normally the grids numbers were ranged from 12000 to 180000. The grids dependency should be necessary to select a proper cell numbers of the grids. For 3-D cases: the typical cell numbers are about 10-20 million.

5) Applications of transitions have obvious impact on the accuracy of CFD prediction of high lift flows. The transition should be simulated properly to get accurate simulations.

6) For both 2-D cases and 3-D cases, the predictions at stall and after are much more unreasonable than in linear range. It is still impossible to make quantitative prediction for high lift flows in this area.

1.4 Optimisation – methods, state of the art studies (computational)

Conventionally the aerodynamic design problems are tackled in two levels. The first level is the overall configuration design mostly based on the previous design experiences. The second level is the detailed component design in which some 2-D and 3-D CFD codes are used to understand the flows. But this two-level approach is a one- pass or multi-pass method. The quality of design is seriously dependent on the experience and the results are not highly optimized.

Conventional design process for high lift design is also of one pass or multi pass. The designs are normally initialized from existed configurations and

directed by the experiences. With the applications of high fidelity CFD calculations and wind tunnel tests, long time and great number of cost are consumed to reach qualified concepts which still have the room to be improved owing to the very limited exploration of the whole design space.

Optimizations are different. They have strategies to search the design space automatically and can identify the most competitive design from a group of concepts effectively. Thus, it can search the optimal results according to the objective functions applied. Due to the developments of computational capacity and optimization methodologies, optimization codes have displayed strong advantages and might be the future tools for high lift devices design.

Another advantage of optimizations is their openness and ability to generate more novel design concepts. In contrast, traditional design methodologies based on the previous experience of the designers tend to be limited.

1.4.1 Automatic computational design tools

Since the appearance of computational techniques in aerodynamics, continuous developments has been reached for automated numerical aided design tools in last thirty years.

Computational fluid dynamics (CFD) emerged in late 1960s and has become a principle aerodynamic technology for aircraft configuration development. [31] The substantial of turbulent models and numerical discretization techniques have enabled CFD to predict accurately on most aerodynamic flows, and promote CFD to a promising role in the aerodynamic design in recent years. As a result, certain aerodynamic designs can pass through from CFD to real flight without any validations from wind tunnel testing. By reducing the requirement for experiments, these applications both shorten the length of design cycle and minimize the cost.

The capability of optimisation algorithms have also emerged significantly. Kinds of algorithms were developed to tackle with different problems. Effectiveness

and quality are focused to enhance the ability of optimisation systems. In aerodynamic design area, the combination of optimisation systems and CFD tools formed the strong CFD based automatic computation design tools.

Started from sole discipline design, the automated computational design tools can deal with multi-discipline or multi-objective problems in current and can be described as multi-objective optimisation (MOO) systems. For high lift devices design, conventional design approaches are seen as time and cost ineffective owing to the complexity of flow features and the automated MOO systems are expected as a more effective method to deal with the challenging high lift devices design .

Comparative advantages of automatic computational design tools over conventional design approaches are listed below:

1) Automatic computational design tools can improve the efficiency and quality dramatically due to their essences of can utilizing rapid computation and catching global optimal;
2) The data exchanges between input and output in the process of automatic computational design tools are more reliable and prompt than the human dominated design systems.
3) They can produce more novel solutions than human experienced-based design system.

In parallel, the higher requirements of aircraft design have been presented and called for the assistance of more effective design tools. Recent requirements for aerodynamic design are dictated largely by environmental concerns. With the objective to minimize the impacts on climates, 50% reduction in emissions of nitro oxide, carbon oxide and carbon dioxide are required by 2020. [32] Additionally, due to the tendency for higher population density in the vicinity of airports, strict limits on noise emissions from aircraft are also required. Additionally, the fierce completions between aircraft suppliers present very high requirements for aircraft performances. Design techniques are also highly

focused to supply perfect products with excellent performances. The CFD based optimization systems supply promising choices for this task.

Different from conventional CFD design tools, the CFD based optimization integrates geometric parameterizations, CFD solvers and optimization algorithm. Geometric parameterization methodology is used to generate new geometries according to the new design vectors; CFD solvers is responsible for the solution of flows; optimization algorithm can set up the objective functions and receive the design parameters from CFD results and generate new design vectors to geometry parameterization. According to the design variables to be tackled, optimization can be categorized as single-objective optimization and multi-objective optimization (MOO).

Aerodynamic designs are always highly constrained, nonlinear and multidisciplinary. Thus the meanings of single-objective optimization are always limited to validation of the ideas and far removed from the practical fulfilment to real design. MOO systems are needed to tackle these challenging problems.

The history of MOO applications on aerodynamics has been explored by Kiporous [33]. Regarding to the fact that it is becoming clearer that MOO systems are more likely to be applied in practical industrial problems rather than for the simplified researches in academic lab, hence, the overview of the applications of MOO systems are emphasised on 3-D real world aerodynamic designs problems and high lift devices design.

Both non-gradient based algorithms and gradient based algorithms are widely applied. For gradient based algorithms, the primary advantage is effectiveness. Owing to the character that the time consuming is independent on design variables, some gradient based algorithms can solve aerodynamic problems with high numbers of design variables. This assists presentation of the gradient based algorithms as a promising application in aerodynamic design optimization.

Leovirijakit and Jameson [34] used a gradient based MOO system of adjoint algorithms based on control theory with an inviscid compressible Euler equation to optimize a realistic Boeing B747-200 wing-fuselage configuration. In the study, structure weight had been considered to make the design more practical and meaningful. The results show that 12.3% reduction of drag has been reached at Mach number 0.87 and a lift coefficient CL 0.42, by the optimization of 8 design iterations. Another case maximized the flight range and allowed changes in sweepback, span, root chord, mid-span chord and tip chord; with these 8 design iterations 12.7% reduction in weight was reached. The optimizer reduces the sweepback to reduce the weight and increase the span and lengths of chord to reduce drag, which are reasonably correct compared to aircraft design experiences. Nevertheless, two points listed below have not been simulated realistically:

1. The structure model is only a function of planform variables but has not considered the impacts of aerodynamic loading.

2. Viscous effects have not been considered.

Kim and Jameson [35] used an adjout-based Navier-Stokes design and optimization method for two-dimensional multi-element high–lift configuration investigation. Spalart-Allmaras turbulence model is selected to account for high lift flows. Airfoil shape, element positioning and angle of attack are selected as design variables. Optimized results have been reached and the potential of this methodology has been verified. For the high lift configuration 30P30N selected for the reason of availability of experiment data, 157 design variables, a very high number, were set up to optimize the lift coefficient . Though the base line configuration is a highly optimized configuration in lift, the optimized results have still been reached. These results show that the adjoint method has great potential for the design of high lift devices.

Driver and Zingg [36] applied a two dimensional Newton-Krylov discrete adjoint optimization algorithm to selected aerodynamic problems where the position of

transition from laminar to turbulence is free. The transition location is predicted by the coupled Euler and boundary layer solver MSES through the e^N method. The flows are solved by a Spalart-Allamas model. The design functions are set up to maximum lift to drag ratio, endurance factor and lift coefficient. The results show that the algorithm can generate the expected design shape.

In aerodynamic design, single point design constantly introduces a worse design performance. Hence the design should ideally be applied under a range of operating conditions. Zingg and Elias [37] used a Newton-Krylov discrete adjoint gradient based optimization algorithm to manage some multi-points problem. A technique has been developed to select sampling points automatically within the operating range and their weights to obtain the desired performance. The design constraints are relative to lift constrained drag minimization. The results show that a multi-points optimization is apparently different from the single point optimization. Still the potential of multi-objective optimization has been achieved.

Genetic algorithm (GA) is an alternative approach to tackle multi-objective problems in aerodynamic. One obvious advantage of GA is that it can be easily adapted to different CFD solver as it is separated from flow solvers compared to the gradient based method. The other advantage is the capability to capture global optimal design. In contrast, the gradient based methodologies are easily trapped by local optimal. Nonetheless, one deficit that hinders wide acceptance of GA by real world designers is its inefficiency. It requires an evaluation iteration to solve every different design variable. However, developments of innovative efficient variants of GA and hard computational resources have enabled GA to be applied to real world aerodynamic design optimizations.

Peigin and Epstein [38] applied an optimization tool OPTIMAS based on Genetic Algorithm and coupled with a full Navier-Stokes computation code to solve some multi-points aerodynamic design problems for a business jet aircraft. The results demonstrate that significant drag reduction has been achieved on and off-design flight points.

Vankam, Lammen and Mass [39] combined advanced meta-models and MOO and then applied the system to a range of aerodynamic design problems. The epsilon-NSGA-ll algorithm which is the new variant of the benchmark NSGA-II demonstrates great efficiency for calculating the Pareto optimal design points for a complete aircraft optimization in VIVACE (Value Improvement through a Virtual Aeronautical Collaborative Enterprise) research project.

1.4.2 Multi-objective optimization systems

According to the number of objective functions used in the system, optimization approach can be categorized to single objective optimization and multi-objective optimization. Single objective optimization, as its name means, overcomes the problem with sole objective and obtains the minimum value as the optimal result. Multi-objective optimization treats the problems of multi-discipline; during these problems two or more objectives should be set up as the optimization criteria.

Normally an optimization design system consists of three essential components: geometry parameterization; optimization algorithm and an underlying simulation tool. One criterion to mark a MOO is the design quality. A qualified optimization should avoid the trap of local optimal and reach the global optimality. Another criterion to estimate the quality of MOO is the effectiveness. To reach an acceptable effectiveness to treat a real-world problem within a reasonable time frame, a proper geometry parameterization scheme should be selected to generate new design shape accurately, effectively and feasible for real physics. The optimization algorithm should also be robust and intelligent enough to complete the exploring of the whole design space. On the other hand, simulation solvers should also be speeded up by computational techniques such as parallel method.

1.4.3 Pareto-optima

Normally there are two approaches to solve multi-objective optimizations. The first is the composite objective function method, which integrates different design functions into a sole one and then treats it as a single objective optimization. For this method, the weight factor of different design vectors should be pre-set. Inevitably, the final composite function includes the preferences of the designers for different design variables.

The second approach is to utilize Pareto-optimal sets. Within this strategy all the design variables are kept alone and optimized to minimum simultaneously. As the output of the optimization, a number of Pareto-equivalent should be reached and can form the Pareto-optimal set. Then designer can make his choice according to this set of design vectors.

Consider first for n objective functions f(x1),f(x2),…,f(xn), where n is more than 2, an objective function vector F(x), where F (x) ={f(x1),f(x2),…,f(xn)}, A point x1, with an objective function vector F1, is said to dominate point x2, with an objective function vector F2, if no component of F1 is greater than its corresponding component in F2, and at least one component is smaller. Similarly, x1 can be said to be Pareto-equivalent to x2 if some components of F1 are greater than F2 and some are smaller. Pareto-equivalent points represent a trade-off between the objective functions, and it is impossible to say that one point is “better” than another Pareto-equivalent point without introducing preferences or relative weighting of the objectives.

1.4.4 Classification of MOO

There are a number of MOO algorithms available for engineers each suited to a different problem. According to the different types of characteristics of problems, optimization problems can be classified as in Table 1:

Table 1 The classification of optimization problems [40]

Characteristic	Property	Classification
Number of control variables	One	Univariate
	More than one	Multivariate
Type of control variables	Continuous real numbers	Continuous
	Integers	Integer or Discrete
	Both Continuous real numbers and integers	Mixed Integer
Problem functions	Linear functions of the control variables	Linear
	Quadratic functions of the control variables	Quadratic
	Other nonlinear functions of the control variables	Nonlinear
Problem formulation	Subject to constraints	Constrained
	Not subject to constraints	Unconstrained

In aerodynamic shape design area, gradient-based algorithms cannot well suited for all problems as there are a number of constraints as well as a lack of information about the gradient. However, the popularity of the application of gradient–based algorithms has still been gained owing to their advantage of cost effective. Genetic Algorithms is another principle algorithm of the MOO in this area. SA algorithms are used but less.

1.4.5 Existing MOO algorithms

1.4.5.1 Genetic algorithms

Genetic algorithms are search algorithms based on theory of adaptive system. There are good reasons for the widespread use of GA in various application domains. The most important among them are listed below [41]:

(a) They are robust and may capture the global optimal solution, without being trapped to local optima,

(b) They may readily incorporate any existing evaluation software, like CFD, CEM, etc. solvers, with the minimum effort,

(c) They may handle either single- or multi-objective problems,

(d) The only information they require is one payoff value per objective for each candidate solution, according to a pre-defined cost function and

(e) They can easily be parallelized, so that different members of the current population may run concurrently on different networked processors.

In [42] it can be found that GA algorithm captured really global optimal; whichever datum shape was started; the final optimized shapes were really the same.

On the other hand, an obvious drawback of GA is the high number of calls to the evaluation software they require, which correspond to a considerable computing cost.

The work flow of genetic algorithms is presented in Figure 23.

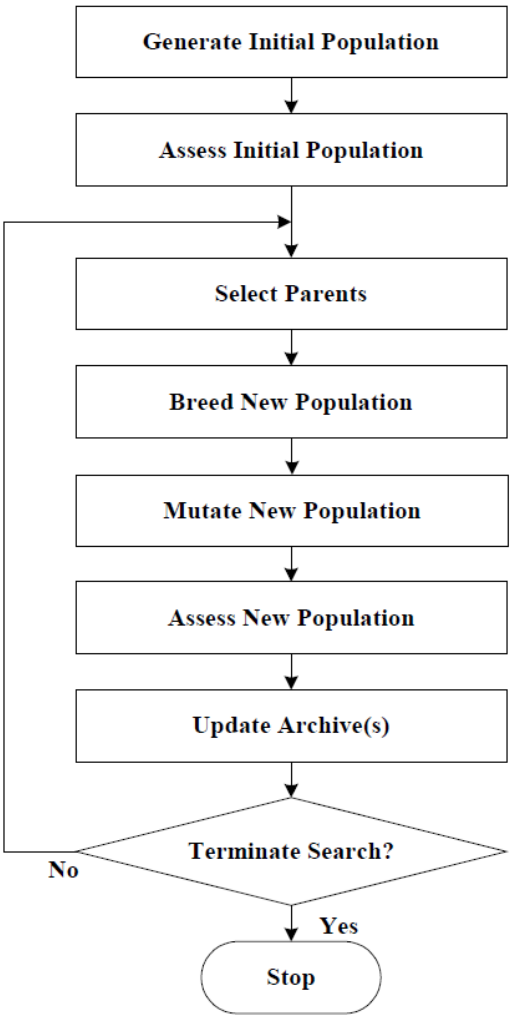

Figure 23 The flow diagram of genetic algorithms [43]

1.4.5.2 Simulated Annealing algorithms

The Metropolis algorithm is the base of the Simulated Annealing approach. It exploits an analogy between the search for a minimum in a general system and the way in which a minimum energy crystalline structure is generated when a metal cools.

The flow charter of simulated annealing algorithms is shown in Figure 24.

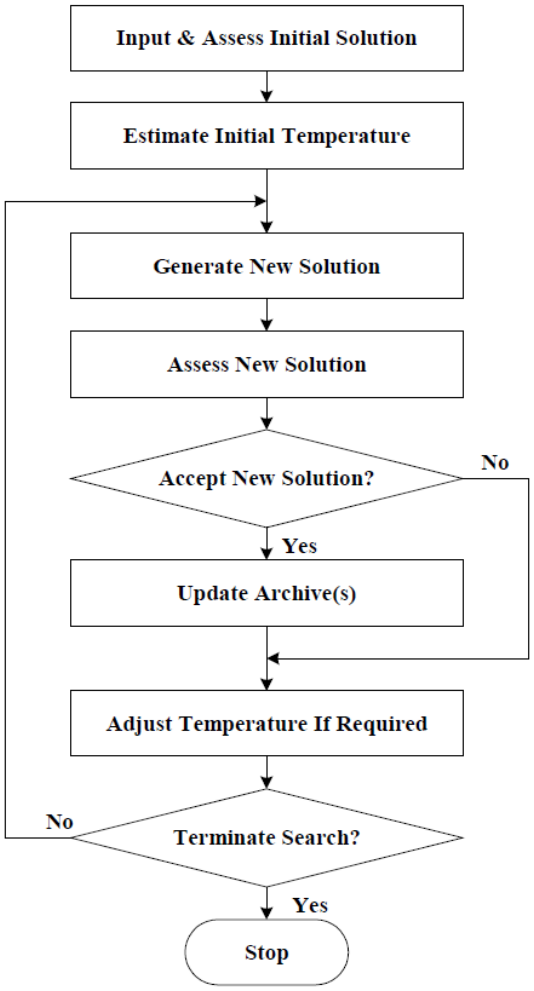

Figure 24 The flow diagram of Simulated Annealing algorithms [43]

1.4.5.3 Tabu Search algorithms

Compared to GA and SA algorithms, Tabu search algorithms had received much less attention in the past. Only a few of the investigations using TS were published with an aerodynamic aspect. But a literature survey shows that TS algorithms are especially effective in an aerodynamic shape design owing to their advantage in overcoming highly constrained and continuous problems. Several TS codes have been developed and excellent results have been achieved, showing their reasonable compatibility to deal with aerodynamic shape design problems.

Tabu search algorithm is the combination of local search and some intelligent strategies, such as the efficient Hooke & Jeeves which can move both down-hill and up-hill to avoid the trap of local optimal and innovative memories strategy which ensure the coverage of the whole design space. The typical flow charter is shown in Figure 25:

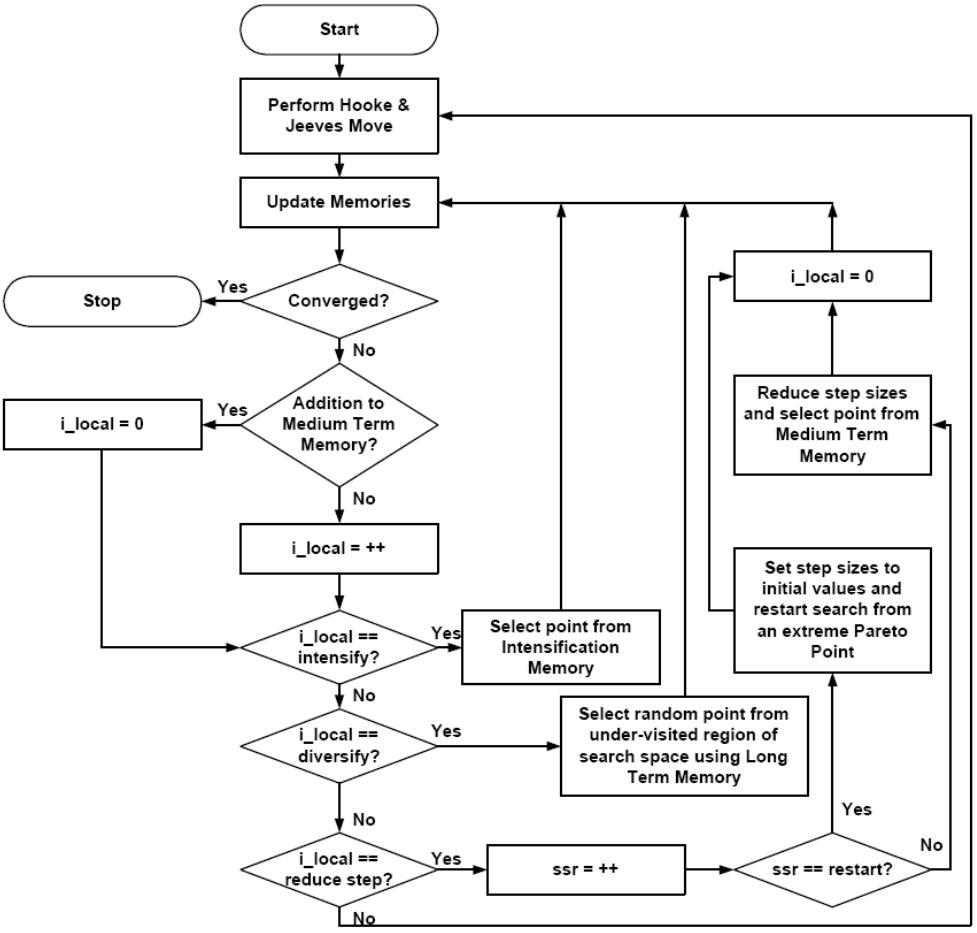

Figure 25 The flow diagram of multi-objective Tabu search algorithms [33]

During the optimization for a problem of n design variables, we may choose a reasonable step size to increase and decrease the variables, so after that we can have 2n design vectors maximally. During the moves, the dominated design vectors will be removed and stored in short term memory. The Pareto-equivalent design vectors will be selected and stored in medium memory. The

point selection of H&J moves and different Tabu Search memories is depicted in Figure 26.

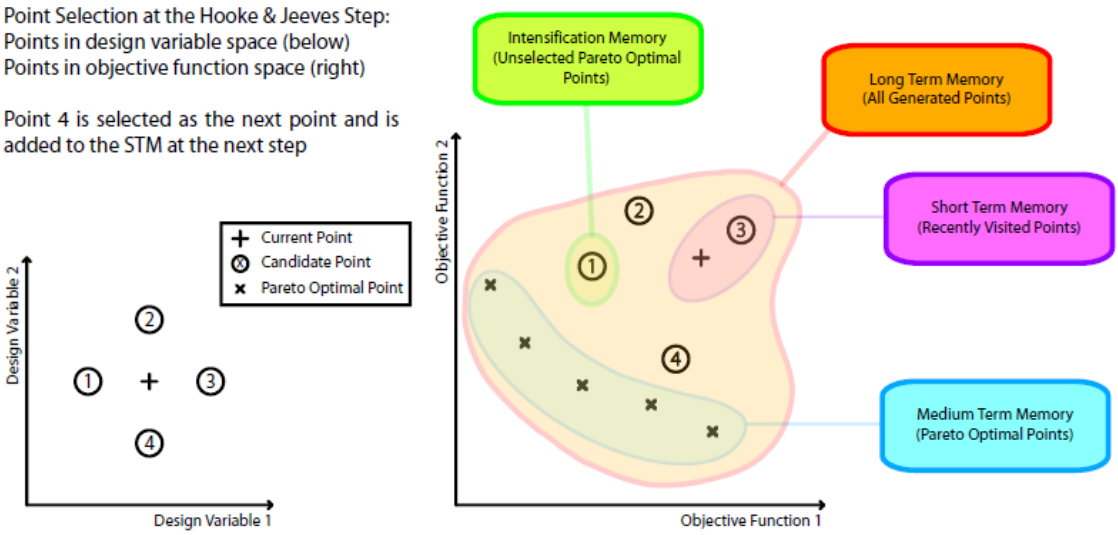

Figure 26 point selection for Hooke&Jeeves Move and Tabu search memories [33]

Short term memory is used to store the dominated solutions visited. These dominated points are defined as tabu and cannot be revisited. By this strategy the design variables and calculation time are reduced. In constraints handling process if the designated constrains are violated by some design variables; these variables are also stored in short term memory.

Medium term memory is used to store the Pareto-optimal sets.

Long term memory records all the information explored. This memory is used to realize “search diversification”. If there is no suitable Pareto-optimal produced after several iterations, this strategy will be arose to direct the evaluation to these under explored areas for the search.

During certain iterations, more than one design vector is better than the current and is not dominated by other design vectors. But only one of them should be selected as the next datum; the remains should be stored into intensification memory. In the coming iterations if there is no Pareto-optimal solution

produced, the search will be move to intensification memory to select randomly one point as the new datum to start the search.

Step size reduction is a strategy which can focus on the area with high density of Pareto-optimal by reducing the step size of the move for design variables. If the search move cannot continue in normal search, they may orientate to these space with high density of Pareto-optimal by step size reduction. With this strategy the global optimal search will be enhanced. It is the final step of the tabu search algorithm.

In real word problems, some considerations should be given in relation to the feasibility of the geometry, the generation of grids and the solution of the CFD solver:

1) Geometry considerations. During the optimization unrealistic geometry may be produced to be physically impossible. Such as negative volume or surfaces. So constraints should be necessary to avoid the occurrence of this kind of problems;
2) Mesh considerations. Even the geometry is physically valid, the problems of mesh generation may occur owing to some aspects from the complexity of geometry or the limitation of the meshing software itself. So constraints should also be handled for these problems;
3) Simulation considerations. Even the valid geometry and mesh are given, there may be still some problems relative to the simulation solver such as convergence. So considerations should be needed to tackle these problems.

There are two main approaches to set up the constraints for optimization. One approach is the penalty function; that is, any design vectors which violates the constraints will be penalized to reduce its possibility to be accepted as pareto-optimal. The other method is the hard constraints which mean any design vectors violating the constraints will be deemed to be Tabu and sent to short term memory.

Computation parallelization ensures the potential of rapid calculation for the optimization and benefits the efficiency of optimization. There are three kinds of parallelization schemes in MOO:

1) Function decomposition;
2) Domain decomposition; and
3) Multi-thread search.

1.4.6 The application of optimization on high lift devices design

In realistic applications, concerned with multi-objective meta-heuristics for both discrete and continuous problems, it had been found that 70% of the articles used GA or ES as their primary meta-heuristic; 24% SA and 6% TS. [44]

Owing to its advantage of global optimal and robustness, GA was becoming the main multi-objective optimization approach. In aerodynamic design area, it also widely used in the range of multi-objective.

Gianankou had investigated the optimization on three element airfoil using Genetic Algorithm. See Figure 27. Using a lower cost GA method, an optimal configuration for slat and flap had been worked out with higher CLmax. [41]

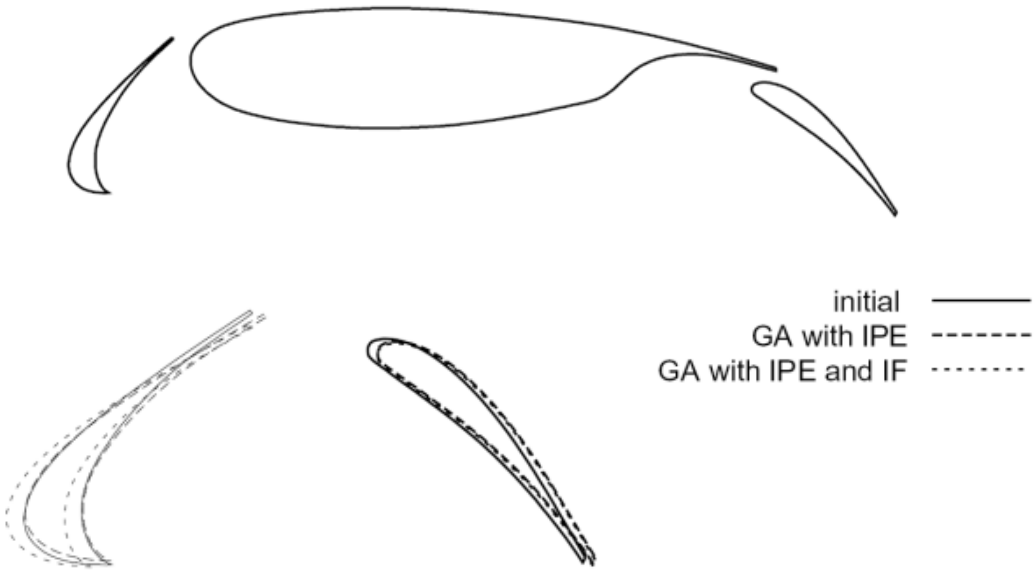

Figure 27 An optimization example for 3-element airfoil [40]

Tabu search has also shown its capability. In [45], the comparison of the optimization quality on a case between a Tabu search algorithm PRMOTS and a leading GA algorithm; NSGA-II had been performed. The results show that Tabu search algorithm was wholly competitive with NSGA-II algorithm.

In reference [46], an Airbus 2-D GARTEUR (Group for Aeronautical Research and Technology in EURope) case was optimized by Tabu algorithm. The comparison of the datum and optimization geometry for the case is shown in Figure 28. After the multi-objective optimization, the three element airfoil can reduce the airfoil drag about 10% with the constant lift which significantly benefited the airfoil performance.

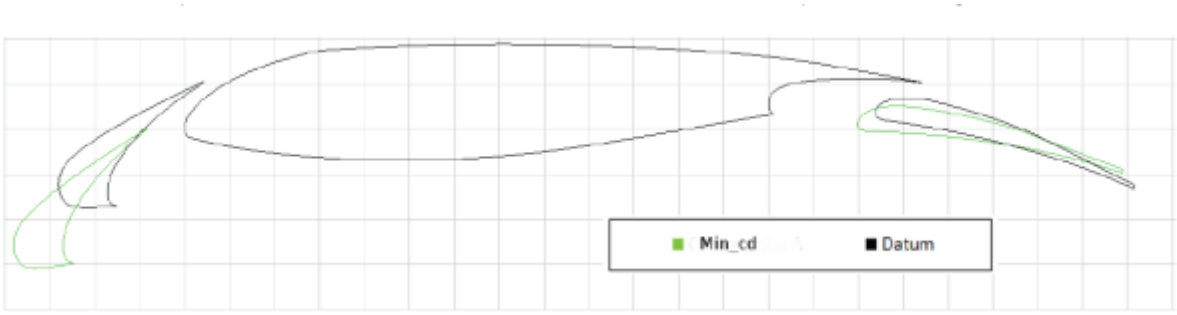

Figure 28 Datum and optimized geometry for lowest Cd [41]

1.5 Aims and Objectives

Due to the significant effects of high lift devices on aircraft performance and competitiveness, the design of high lift devices are highlighted as significant. CFD has the advantage of being cost effective and time effective compared to a wind tunnel test and becomes the main approach for high lift devices design. Nevertheless, the traditional design process which is one pass or multi-pass cannot obtain the optimal results by applying CFD only. The multi-objective optimization coupled with CFD codes shows a promising approach to solve this problem. The global optimal results for high lift devices can be achieved by the applications of multi-objective optimization.

Generally, the criteria to judge the quality of the combination of multi-objective algorithm and CFD solvers are that optimality can be reached and wall clock time needed for the optimizations achieved. The next question regards the choice of CFD solvers to best fit multi-objective optimization. Previous study has identified the appropriateness and significance of higher order CFD discretization methods in the aerodynamic design optimization on morphing airfoil sections. It was identified that the most accurate and most computationally expensive models are not the most preferred during the optimization cycle in terms of overall wall clock time required and quality of optimality that can be achieved. [1]

This thesis is a comparative investigation of how three current main horse RANS codes, S-A, K-w SST and K-epsilon Realizable, each combines with a Tabu search Multi-objective optimization approach.

To complete the objective, a mature case which is NLR 7301 two element airfoil with 2.6% gap at attack angle of 13.1 degree is selected for investigation. It should be emphasized that the main aim is not the optimization of NLR 7301 airfoil shape but the investigation of which turbulence model can best couple with optimization with the criteria of wall clock time cost and quality of optimality.

The main works are listed below:

- To generate structured grids suitable for MOP,
- To establish credible CFD modelling for the airfoil NLR 7301 ,
- To evaluate the sensitivity of the results to turbulence modelling.
- To modify a multi-objective optimization software.
- To analyze the results of optimization.

1.6 Baseline configuration - NLR, geometry description, existing experimental and CFD studies

1.6.1 Geometry and case description

In this study NLR7301 two-element configuration which is a 2-D supercritical airfoil including a main airfoil and a flap with a moderate 20 degree deflection angle is selected. They are two configurations having different flap gaps which are 1.3% and 2.6% respectively for this high lift airfoil. In this study the 2.6% gap configuration is selected. The geometry is shown as Figure 29. The detailed coordinates of NLR 7301 are presented in Appendix A.

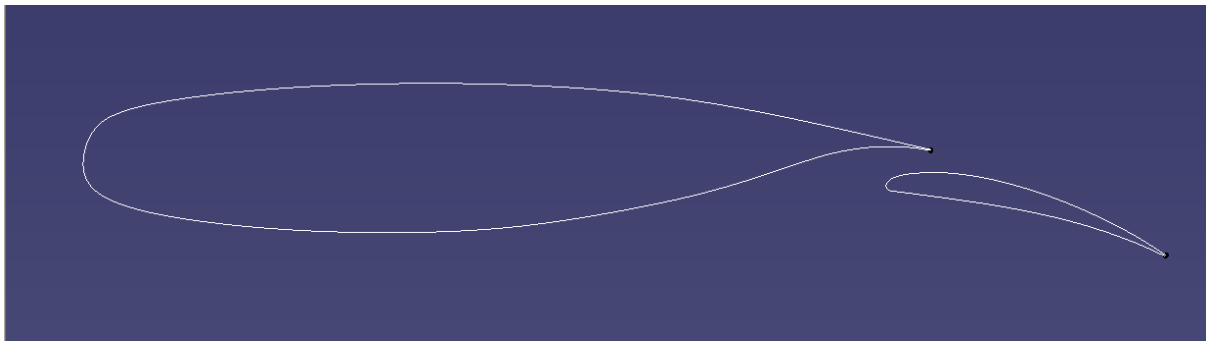

Figure 29 The NLR 7301 geometry

The Mach number is 0.185 for the case, which is typical in take-off conditions. The Reynolds number is 2.51 million based on the retracted airfoil chord 0.57 m. Attack angle is 13.1 degree. [47]

1.6.2 The experimental study on NLR 7301

NLR 7301 two- element configuration was designed as an attached flow case by NLR, with the objective to serve as the validation of CFD codes. This configuration was tested mainly in NLR 3m*2m low speed wind tunnel in Amsterdam and some additional runs were tested in new NLR 3m*2.25m low speed wind tunnel for verification in Northeast Polder at the end of the 70s.

The test configuration was manufactured as a cylinder model and was supported by the walls of the wind tunnels. Surface pressures were measured by traditional pressure tapings, and force and drag were integrated by surface pressure. A specially manufactured boundary layer probe was used to measure the velocity profile and hence to calculate the skin friction coefficient indirectly. In addition, flow visualizations were performed to reach a better understanding of the flow.

Free transition was applied in the test. The transition position was investigated by sublimation method and the results of the transition position are listed in Table 2:

Table 2 the transition position of NLR 7301 2 element airfoil [48]

Element and side	x/c (Attack angle 13.1degree, 2.6% gap)
Main element upper side: Laminar bubble location	0.024-0.035
Main element lower side	0.710-0.740
Flap upper side	1.065-1.080

Figure 30 shows the pressure tapping distribution in a typical section. Figure 31 shows the pressure results at two different attack angles which are 6 degree and 13.1 degree respectively for the 2.6% gap configuration. From the test results it can be found that the laminar flow bubble exists on the leading edge of the main element caused by very high adverse pressure, hence triggering transition in the upper surface. No obvious trailing edge separation occurs by the estimation of pressure coefficient.

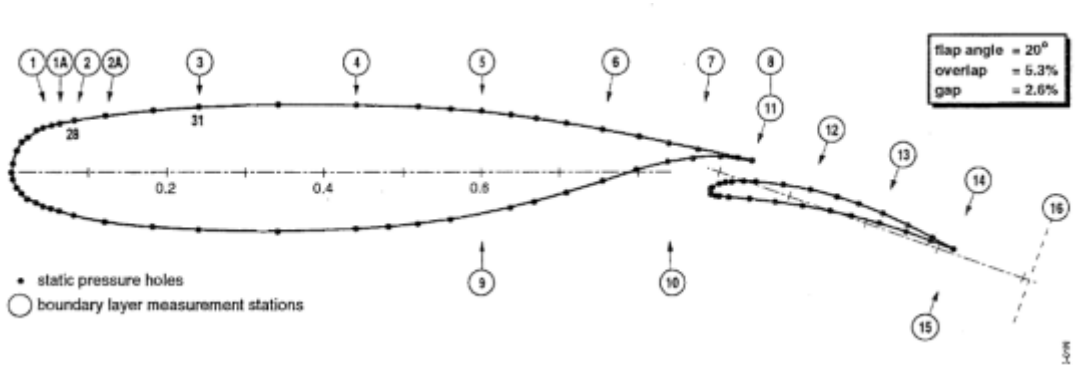

Figure 30 The pressure tappings distribution of the NLR 7301 airfoil [47]

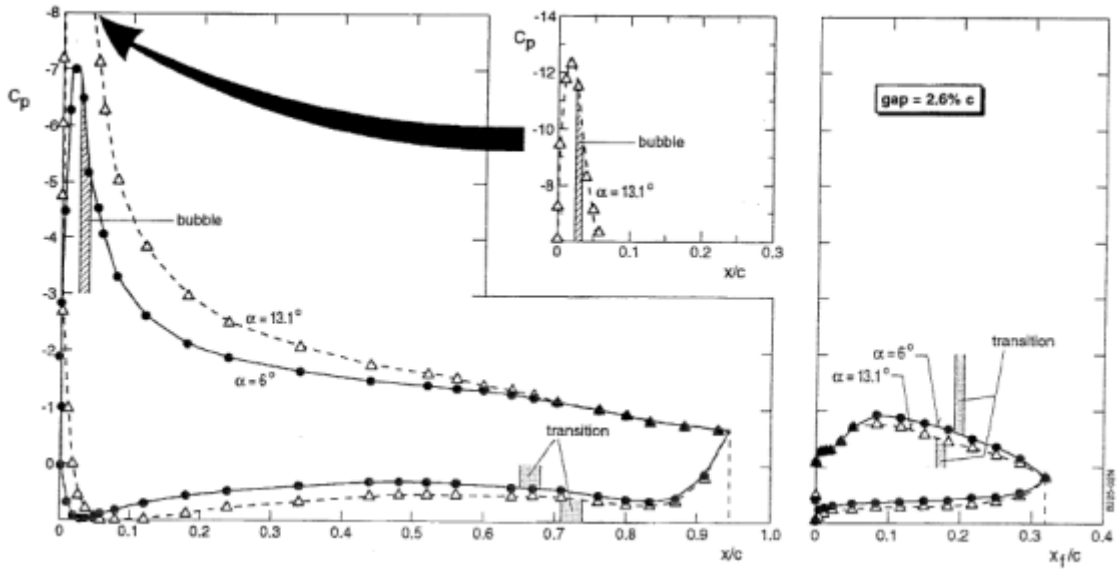

main element flap

Figure 31 The pressure distribution on the NLR 7301 airfoil [47]

After the completion of the test, the results were processed and two cases were chosen as the validation for CFD codes, which are:

1) 2.6% gap configuration at attack angle of 13.1 degree.

2) 1.3% gap configuration at attack angle of 6 degree.

It should be noted that the deformations were observed during the test. The real deflection angle in wind is about 19.75 degree rather than 20 degree; the gap was also decreased to about 2.4% from 2.6%. [47] These deformations may be taken into account when high fidelity CFD simulations run.

1.6.3 CFD studies on NLR 7301 high lift configuration

NLR 7301 two element airfoil is a high lift configuration dominated by mild and attached flow rather than separated flow. So it is not a big challenge to predict this case. It is a good case to be selected if the risks of complex separation are not wanted.

A great number of the computations were performed with different turbulent models and grids on NLR 7301 high lift configuration. The capability of prediction on this configuration is similar to typical 2-D cases we mentioned above. Rumsey had presented an excellent overview of the studies on this configuration in 2002. [22] The main investigations on NLR 7301 two elements airfoil in this overview are collected in Table 3, where the grids and models used are recorded and experiences obtained in these studies are highlighted.

Table 3 Statistics of CFD researches on NLR 7301 two-element airfoil

No	Researchers	grids	Models	Remarks
1	Arnold and Thiele [49]		Laplace interaction law & an IBL method	Lift was over predicted at CLmax.
2	Cantariti and Johnston	Unstructured 15000 cells	K-ε and a differential RSM	Skin friction levels were over predicted
3	Cao and Kusunose [52]	Structured 50000 cells	NASA INS2D code	Lower CL compared to experiments attributed fully turbulence
4	Cebeci [53;54]		IBL approach	Wake effects was important to get good results
5	Fritz [55]	structured	Lam-Bremhorst K-ε	Pressure on flap was not well predicted
6	Godin [56]	structured	SA and SST (Menter)	Transition and model deformation simulation can
7	Jahangirian and Johnston	unstructured	K-ε	Grid adaption can improve the prediction of skin friction
8	Jasper [58]	Structured	BL and BB turbulence	Drag levels were over predicted by a factor of 2-3.
9	Johnston and Stolcis [59]	Unstructured 12000cells	K-ε	Stall angle was over predicted; and velocity profile was not as good
10	Kim [60]	Structured 25000 cells	K-ε, K-ω and SST	Incompressible formulation led to worse prediction than compressible formulation
11	Kusunose and Cao [61]	Structured 70000 cells	S-A	Transition was good predicted only suck peak was under predicted.
12	Larsson [62]	Structured 37000 cells	K-ε	Far field extent at least 50c and far field circulation correction were needed to accurately predict drag.
13	Lien [63]	Structured 36000 cells	K-ε	Skin friction levels were somewhat high than experiments
14	Nelson [64]	Structured 90000 cells &180000	BB and SA	Deformation simulations of shape improved the prediction of velocity profile.

Surface pressure and lift can be accurately predicted by most studies, almost all the turbulence models can capture the pressure and lift coefficient fairly well. For pressure coefficients, the difference between calculations and experiments can be lower than 0.2 except on leading edge. The predictions of velocity profile and skin friction are generally good. [22] Fine grids and detailed considerations were helpful to predict the overall flow field more accurately. [56]

As with any other cases, drag is much more difficult to be predicted accurately. In some references the drag was 2 or 3 of the factor compared to experiment data. [58] Some studies pointed out that drag was sensitive to the far field grid extent and boundary conditions.

It can be found from the table that most turbulence models applied for NLR7301 2-element airfoil are Navier-Stokes methods. One equation method Spalart-Allmaras model and two equation K-ε model were widely selected by the researchers. Generally speaking, owing to its over modelling of the velocity profile near the wall, the K-ε model tended to over predict skin friction and give worse agreement with experimental velocity profiles than other models. [57, 59, 63] SA and SST models yielded generally similar results. In terms of solvers, Compressible RANS formulation gave better results than incompressible RANS near maximum lift. [60]

Structured meshes were more favourable to be selected than unstructured mesh. Cell numbers were ranged from 12000 to 180000. Grids larger than 90,000 points were required for grid independence of drag, but lift and surface pressures were less grid-sensitive. In terms of the dimensions of far-field, at least 50 chords out boundary away from the airfoil is recommended for this airfoil.[62] Grids density is also required in the region away from the airfoil owing to large circulation which affects further occurs in this case and coarse grids may introduce the failure solution in this area. [65]

Another excellent validation work for NLR7301 2-elements airfoil was from the study of European validation project (ECARP). By utilizing the simulation of

transition positions and circulation corrections, the outstanding prediction of drag had been reached with the accuracy of lower than 10% compared to experiment data, which improved the level of drag prediction in this case quite a lot. However, a limited far-field of about 10-15 chords were applied to control the cell numbers. [43]

Chapter 2 CFD Simulations

2.1 Navier-Stokes equations and Turbulence modelling

In CFD, different ways exist to handle the simulation of turbulence. Depend on the nature of the problem these approaches can be categorized as RANS method, detached eddy simulation (DES) or combined approaches between RANS model and large eddy simulation, large eddy simulation (LES) and direct numerical simulation (DNS). The RANS equations can be solved on coarser meshes and permit the simplification of steady flow. Consequently, solving the RANS equations is currently the only viable option for most practical aerodynamic computations.[66] In this study; three linear eddy viscosity turbulence models are selected: Spalart-Allmaras (SA), k-ω SST and k-ε Realizable.

2.1.1 Navier-Stokes equations

Navier-stokes equations which were derived independently by G.G.Stokes in England and M.Navier in France in the early 1800's are comprised of the continuity, momentum, and energy equations. These equations speak physics of the flow by relating how the velocity, pressure, temperature, and density of a moving fluid and are the mathematical statement of three fundamental physical principles upon which all of fluid dynamics is dependent. [67]

Continuity Equation: This mathematical equation applies the fundamental physical principle of conservation of mass.

$$\frac{\partial \rho}{\partial t} + \frac{\partial}{\partial x}(\rho u) + \frac{\partial}{\partial y}(\rho v) + \frac{\partial}{\partial z}(\rho w) = 0$$

Equation 2-1

Momentum Equation: This mathematical equation applies the fundamental physical principle of Newton's second law.

Momentum equation in x-direction:

$$\frac{\partial}{\partial t}(\rho u)+\frac{\partial}{\partial x}(\rho u^2)+\frac{\partial}{\partial y}(\rho uv)+\frac{\partial}{\partial z}(\rho uw)=$$

$$-\frac{\partial p}{\partial x}+\rho f_x+\frac{\partial}{\partial x}\left[2\mu\frac{\partial u}{\partial x}-\frac{2}{3}\mu\left(\frac{\partial u}{\partial x}-\frac{\partial v}{\partial y}-\frac{\partial w}{\partial z}\right)\right]$$

$$+\frac{\partial}{\partial y}[\mu\left(\frac{\partial v}{\partial x}+\frac{\partial u}{\partial y}\right)]+\frac{\partial}{\partial z}[\mu\left(\frac{\partial w}{\partial x}+\frac{\partial u}{\partial z}\right)]$$

Equation 2-2

Momentum equation in y-direction:

$$\frac{\partial}{\partial t}(\rho v)+\frac{\partial}{\partial x}(\rho uv)+\frac{\partial}{\partial y}(\rho v^2)+\frac{\partial}{\partial z}(\rho vw)=$$

$$-\frac{\partial p}{\partial y}+\rho f_y+\frac{\partial}{\partial x}[\mu\left(\frac{\partial v}{\partial x}+\frac{\partial u}{\partial y}\right)]$$

$$+\frac{\partial}{\partial y}\left[2\mu\frac{\partial v}{\partial y}-\frac{2}{3}\mu\left(\frac{\partial u}{\partial x}-\frac{\partial v}{\partial y}-\frac{\partial w}{\partial z}\right)\right]+\frac{\partial}{\partial z}[\mu\left(\frac{\partial w}{\partial y}+\frac{\partial v}{\partial z}\right)]$$

Equation 2-3

Momentum equation in z-direction:

$$\frac{\partial}{\partial t}(\rho w)+\frac{\partial}{\partial x}(\rho uw)+\frac{\partial}{\partial y}(\rho vw)+\frac{\partial}{\partial z}(\rho w^2)=$$

$$-\frac{\partial p}{\partial z}+\rho f_z+\frac{\partial}{\partial x}[\mu\left(\frac{\partial w}{\partial x}+\frac{\partial u}{\partial z}\right)]$$

$$+\frac{\partial}{\partial y}[\mu\left(\frac{\partial w}{\partial y}+\frac{\partial v}{\partial z}\right)]+\frac{\partial}{\partial z}[2\mu\frac{\partial w}{\partial z}-\frac{2}{3}\mu(\frac{\partial u}{\partial x}-\frac{\partial v}{\partial y}-\frac{\partial w}{\partial z})]$$

Equation 2-4

In this study, viscosity μ is represented with Sutherland law. It can be calculated with the equation listed below:

$$\mu = \mu_{ref}(\frac{T}{T_{ref}})^{\frac{3}{2}} \frac{T_{ref} + S}{T + S}$$

Equation 2-5

T_{ref} is a reference temperature. It is 273.15K.

μ_{ref} is the viscosity at the T_{ref} reference temperature. It is 1.716E-5$\frac{kg}{m.s}$.

S is the Sutherland temperature. It is 110.4 K.

Energy Equation: This mathematical equation applies the fundamental physical principle of conservation of energy:

$$\frac{\partial}{\partial t}(\rho H) + \frac{\partial}{\partial x}(\rho u H) + \frac{\partial}{\partial z}(\rho w H) =$$

$$\frac{\partial p}{\partial t} + \frac{\partial \dot{q}_x}{\partial x} + \frac{\partial \dot{q}_y}{\partial y} + \frac{\partial \dot{q}_z}{\partial z} + \rho u f_x + \rho v f_y + \rho w f_z$$

$$+ \frac{\partial}{\partial x}[2\mu u \frac{\partial u}{\partial x} - \frac{2}{3}\mu u(\frac{\partial u}{\partial x} + \frac{\partial v}{\partial y} + \frac{\partial w}{\partial z})] + \frac{\partial}{\partial x}[\mu v \left(\frac{\partial v}{\partial x} + \frac{\partial u}{\partial y}\right) + \mu w(\frac{\partial w}{\partial x} + \frac{\partial u}{\partial z})]$$

$$+ \frac{\partial}{\partial y}[\mu u \left(\frac{\partial v}{\partial x} + \frac{\partial u}{\partial y}\right) + 2\mu v \frac{\partial v}{\partial y}] + \frac{\partial}{\partial y}[\mu w(\frac{\partial w}{\partial y} + \frac{\partial v}{\partial z}) - \frac{2}{3}\mu v(\frac{\partial u}{\partial x} + \frac{\partial v}{\partial y} + \frac{\partial w}{\partial z})]$$

$$+ \frac{\partial}{\partial z}[\mu u \left(\frac{\partial w}{\partial x} + \frac{\partial u}{\partial z}\right) + \mu v(\frac{\partial w}{\partial y} + \frac{\partial v}{\partial z})] + \frac{\partial}{\partial z}[2\mu w \frac{\partial w}{\partial z} - \frac{2}{3}\mu w(\frac{\partial u}{\partial x} + \frac{\partial v}{\partial y} + \frac{\partial w}{\partial z})]$$

Equation 2-6

With

$$H = h + \frac{1}{2}(u^2 + v^2 + w^2)$$

Equation 2-7

In the above equations, t, ρ, p, T, h, H represent time, density, pressure, temperature, static enthalpy and total enthalpy, respectively. The three components of the velocity vector u in the x-direction, v in the y-direction and w in the z-direction.

The air in this study is defined as idea-gas. So the pressure p can be calculated by the equation listed below:

$$p = \rho RT$$

Equation 2-8

In the equation above R represents the individual gas constant. T is set up to 300K which is close to the ambient temperature of the wind tunnel.

2.1.2 Turbulence modelling

2.1.2.1 Spalart-Allmaras (SA) model

The Spalart-Allmaras one-equation model is one of the most widely-used turbulence models today. It was developed by Spalart and Allmaras in 1992. It has the advantages of robustness and can do well for bounded flow and 2-D mixing layers, wake flows, and boundary layer flows. Owing to its simplification, it has become a routinely used approach for design engineers [21].

The transported variable $\tilde{\nu}$ in the SA model transport equation is identical to the turbulent kinematic viscosity except in the near-wall region. The transport equation is given below：

$$\frac{\partial}{\partial t}(\rho\tilde{v}) + \frac{\partial}{\partial x_i}(\rho\tilde{v}u_i) =$$

$$G_{\tilde{v}} + \frac{1}{\sigma_{\tilde{v}}}[\frac{\partial}{\partial x_i}\left\{(\mu + \rho\tilde{v})\frac{\partial\tilde{v}}{\partial x_i}\right\} + C_{b2}\rho(\frac{\partial\tilde{v}}{\partial x_i})^2] - Y_{\tilde{v}} + S_{\tilde{v}}$$

Equation 2-9

Where, $G_{\tilde{v}}$is the turbulent viscosity production and $Y_{\tilde{v}}$ is the turbulent viscosity destruction that occurs in the near-wall region, μ is the molecular kinematic viscosity. $\sigma_{\tilde{v}}$ and C_{b2} are constants. $S_{\tilde{v}}$ is a user-defined source term. The last term in the above equation was ignored when estimating the Reynolds stresses since the turbulence kinetic energy is not calculated in the SA model.

2.1.2.2 k-ω SST model

During the 1970s-1990s of last century, great efforts were made to develop two-equation models that could handle separated flows around complex geometries, but with limited success. Wilcox created the original k-ω model which has an improved near-wall treatment compared to k-ω model but was still limited owing to its poor performance in practical problems. Finally, Menter developed a model that represented a blend of the K-ω and k-ε models, and included a shear stress transport term that improved the model's performance for adverse pressure gradient wall-bounded flows. This model is written in the K-ω form, and is referred to as the SST model. [21]

Transport equation for k is given as：

$$\frac{\partial}{\partial t}(\rho K) + \frac{\partial}{\partial x_i}(\rho K u_i) = \frac{\partial}{\partial x_i}\left(\Gamma_K \frac{\partial K}{\partial x_i}\right) + G_K - Y_K + S_K$$

Equation 2-10

Transport equation for ω is given as：

$$\frac{\partial}{\partial t}(\rho\omega) + \frac{\partial}{\partial x_i}(\rho\omega u_i) = \frac{\partial}{\partial x_i}\left(\Gamma_\omega \frac{\partial \omega}{\partial x_i}\right) + G_\omega - Y_\omega + D_\omega + S_\omega$$

Equation 2-11

Where, G_K represents the generation of turbulence kinetic energy due to mean velocity gradients. G_ω represents the generation of specific dissipation rate. Γ_κ and Γ_ω represent the effective diffusivity of *k* and ω. Y_κ and Y_ω represent the dissipation of *k* and ω due to turbulence. D_ω represents the cross-diffusion term, calculated as described below. S_κ and S_ω are user-defined source terms.

2.1.2.3 k-ε Realizable model

K-ε model was developed by Shih. This model contains a new transport equation for the turbulent dissipation rate ε and redefines the C_μ compared to standard model. This allows the model to satisfy certain mathematical constraints on the normal stresses consistent with the physics of turbulence. The realizable K-ε model is substantially better than the standard K-ε model for many applications, and can generally be relied upon to give answers that are at least as accurate. [68]

The transport equations for the realizable K-ε model are:

$$\frac{d}{dt}\int_V \rho k dV + \int_A \rho k(V - Vg).da =$$

$$\int_A (\mu + \frac{\mu_t}{\sigma_k})\nabla k.da + \int_V (G_k + G_b - \rho(\varepsilon + \gamma_M))dV$$

Equation 2-12

$$\frac{d}{dt}\int_V \rho\varepsilon dV + \int_A \rho\varepsilon(V - Vg).da =$$

$$\int_A (\mu + \frac{\mu_t}{\sigma_\varepsilon})\nabla\varepsilon.da + \int_V [C_{\varepsilon 1} S\varepsilon + \frac{\varepsilon}{k}(C_{\varepsilon 1}C_{\varepsilon 3}G_b - C_{\varepsilon 2}\rho\varepsilon)]dV$$

Equation 2-13

In the equation above, G_k represents the turbulent production term and G_b represents the production term. γ_M represents the dilatation dissipation. μ_t represents the turbulent viscosity.

2.2 Generation of Grids

2.2.1 Requirements for grids

Regarding the motivations of the study which the CFD calculation should convert into the whole optimisation system, the grids should fulfill the requirements listed below:

1) The grids should be of good quality to ensure accurate results, and

2) The grids should have acceptable time expense owing to there being maybe one thousand CFD iterations for optimisation.

Unstructured mesh is easy to generate but it needs much more time to calculate during the flow solution. Compared to unstructured mesh, structured mesh can reach high accuracy and lower computational cost, [69] though the time to generate the grids is much longer for structured mesh than for unstructured mesh.

Considering the criteria of the optimisation are time cost and optimal quality, structured mesh strategy was selected to generate the grids.

As discussed in [47], the blockage of the test model of NLR7301 2-element high lift configuration was very small and the correction of wall effects can be neglected in the wind tunnel, so this case can be simulated in free air without simulating the wind tunnel wall.

Following an initial evaluation of the effect of the domain size and reference to [48], a C-topology domain was selected with 25 chords in front, top and bottom of the airfoil and 35 chords in the rear direction (Fig 34). With this far field, it seems reasonable cell numbers and accurate results can be traded off.

Generally speaking, the size of far-field has impact on the quality of computation results and computation cost. Using a larger size with more grids, more accurate results can be reached but at a higher cost. Referring to the conclusion in [62], to reach accurate prediction on drag, a far-field of about 50 chords is necessary. But considering the objectives of the study, the priority is not to predict drag accurately but investigate the effects of optimisation which is a delta of the aerodynamics between new and old shape. Therefore it is not necessary to use a far-field of 50 chords. According to the introduction of [43], a far-field of 10-15 chords had been applied in the computations with the objectives to avoid usage of excessive grids. Using this limited domain size reasonable results can still be reached by focusing on improving the mesh quality and applying far-field corrections. Thus in this study, a medium size far-field of 25-35 chords is selected and the detail definition is shown in Figure 32.

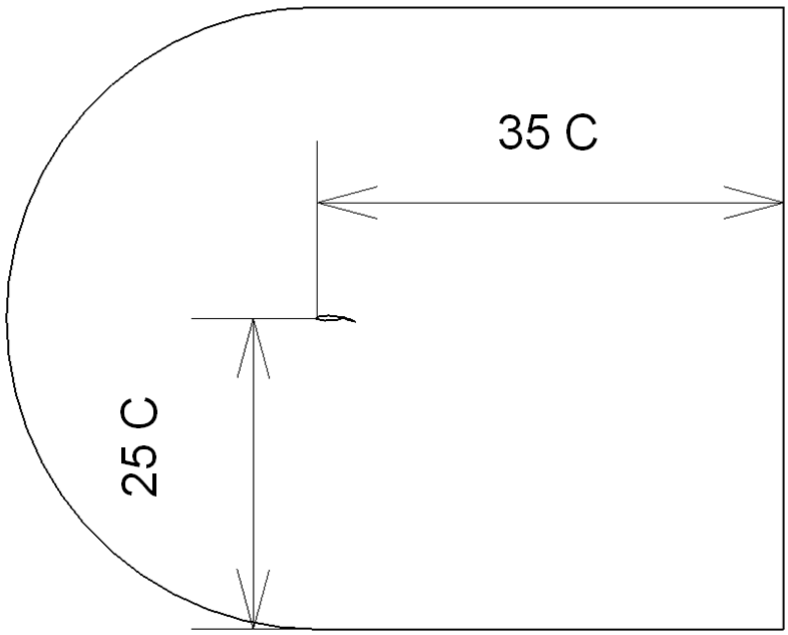

Figure 32 The far-field of the case

2.2.2 Generation of grids

In general, meshes were generated with a targeted y+=1 based on the flat plate turbulent boundary layer estimation. An online y+ calculator was used. [70] For a given Reynolds number which is 2.51 million based on retracted airfoil chord of 0.57 m and desired y^+ value about 1, the calculator estimates the spacing normal to a solid surface required to yield the first grid point in the sub-layer is 0.0000057 m.

To make an accurate prediction of drag, a gradual expansion of the grids in the normal direction of wall was executed by applying the growth ration less than 1.2, which guarantees 20-25 cells in the range of y+ less than 100. [48] On the other hand more density grids were generated in the wake area and gap area which is between main element and flap.

The whole field of grids is formed by several parts which are listed in Table 4. For flow fields, laminar flow zone and turbulent flow zone are set up respectively by naming “Laminar flow” and “Fluid” to simulate the transition of the flow. The

whole airfoil is also divided into main element and flap, with the objective of comfortably analyzing the aerodynamic contribution of each single part.

Table 4 Definition of the parts of the mesh

No	Parts	Boundary types
1	Fluid	Fluid
2	Laminar flow	Fluid
3	Main element	Wall
4	Flap	Wall
5	Far field	Pressure far field

Figure 33 shows the global view of block strategy and meshing. Figure 34 shows the detailed block strategy and meshing around airfoil. Figure 35 depicts the meshing near wall on leading edge. Figure 36 shows the meshes around flap.

To investigate the dependency of grids, except the basic mesh, coarse mesh and fine mesh are generated using the same block strategy. To simplify the name of different grids, coarse grids are named as G1, medium grids which is also the basic mesh is named as G2, fine grids is named as G3. Coarse mesh G1 and fine mesh G3 comprise 30000 and 120000 cells respectively.

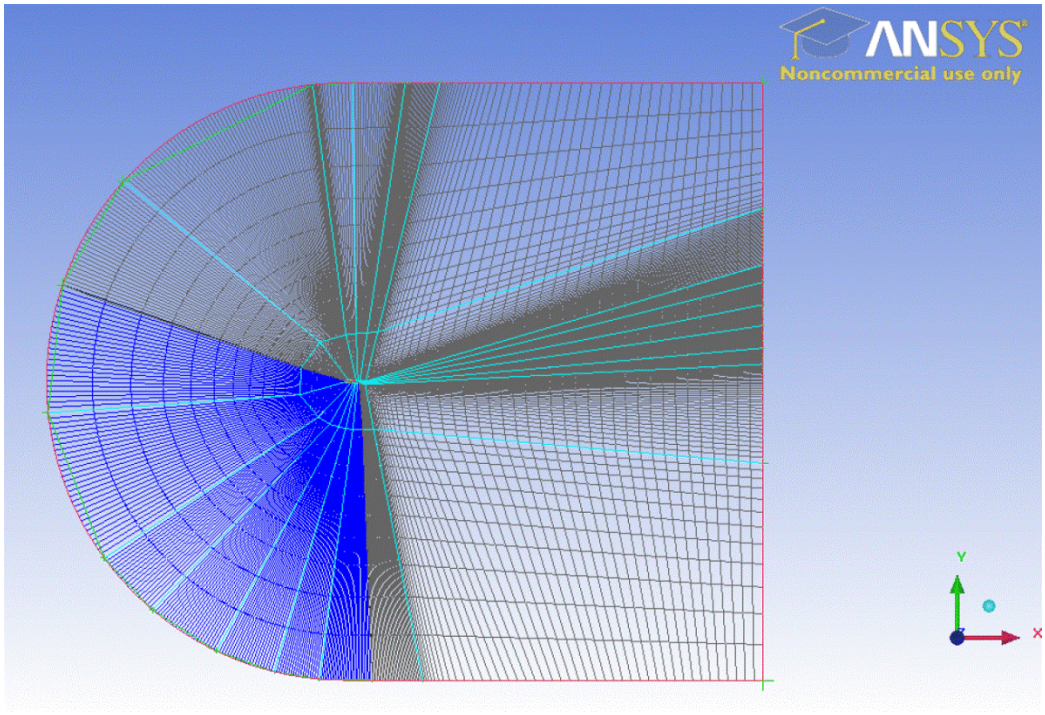

Figure 33 The global view of block strategy and meshing

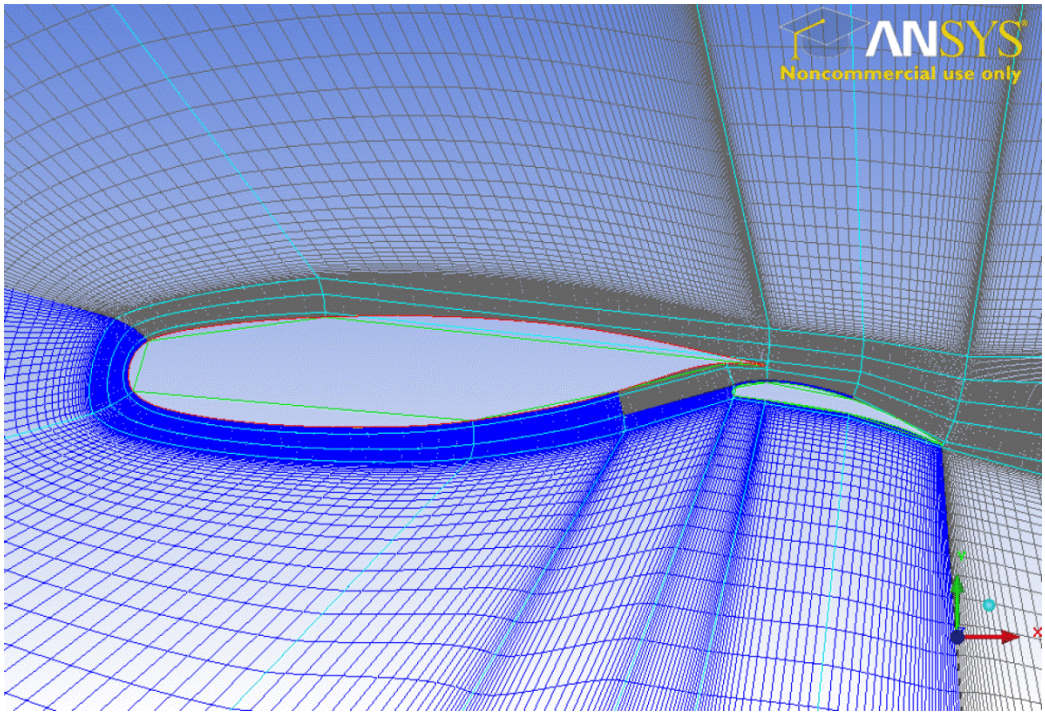

Figure 34 The block strategy and meshing around airfoil

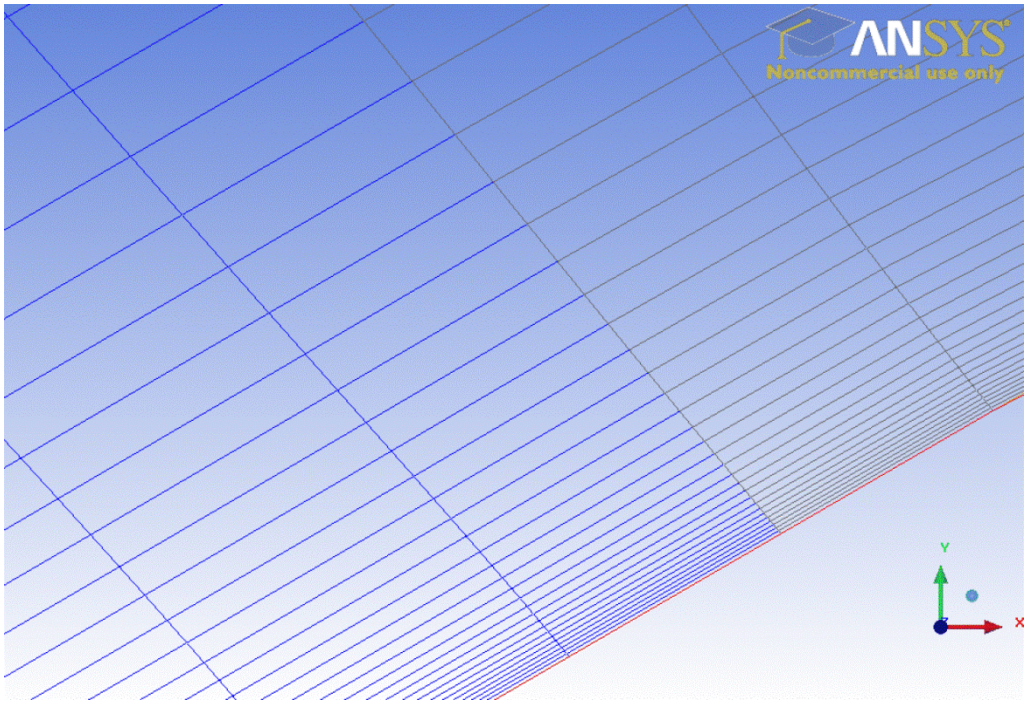

Figure 35 The near wall meshing on leading edge

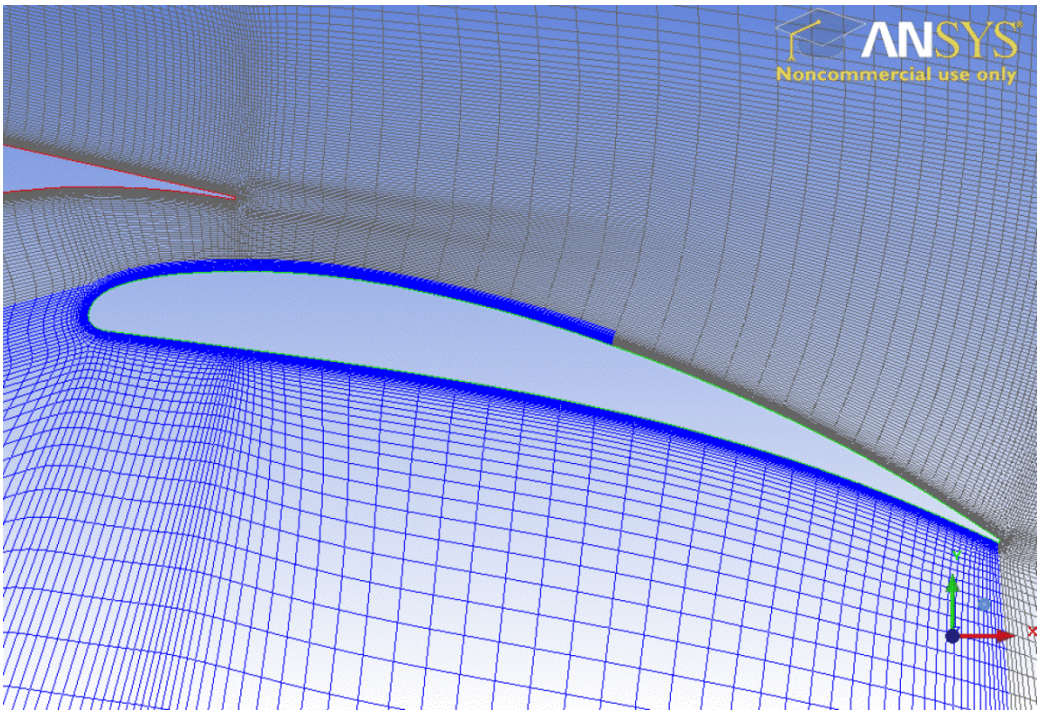

Figure 36 The meshes around flap

2.3 Set up for solvers and boundary condition

A leading commercial CFD software Fluent V12.1SP1 is selected to execute the CFD calculation. In the calculation, density based solver and implicit formulation is selected. Flux type is set up as Roe-FDS. Green-Gauss Node based item is selected for gradient discretization and second order upwind is selected for flow solutions. Courant number is set as 5 at the beginning of the calculation, and under-relaxation factors are modified to reach fast convergence.

Ideal gas law is selected to simulate air density and Sutherland law is selected to describe air viscosity. Temperature is set up at 300K which is close to the low speed ambient pressure wind tunnel temperatures. Based on the parameters above the gauge pressure is calculated as 108958.97 Pa. Mach number 0.185 is set up and attack angle of 13.1 degree is defined by the distribution of x velocity and y velocity. Turbulent viscosity characters, presented by viscosity density is set up as 0.2% which is identical to the value in experiments [47] and turbulence length scale is set up as 0.001 which is defined by the simulation of dimensions of the experiment wind tunnel and the adaption to experiment data.

To increase the convergence speed, for this implicit density based solver, solution steering is also operated during the calculation.

2.4 Results Analysis

All the simulations are performed on the Intel core 7 2.8G multi processors computer. Parallel calculations are applied and three processors are called for during the simulations. In total 9 cases are calculated containing three turbulence models of three grids. The results analysis starts from the introduction of convergence, then the flows between different turbulent models are analysed and finally the grid dependency.

2.4.1 Convergence

Not all cases can converge at the final attached flow statue by utilizing directly the second order upwind discretisation. For example K-ω SST model converge at an obvious separation state which is shown in Figure 37. It seems that the flows of this case are quite sensitive owing to the existence of leading edge laminar separation bubble. Decreasing the order of discretisation can suppress the occurrence of separation and make more probable the convergence at the final attached flow state.

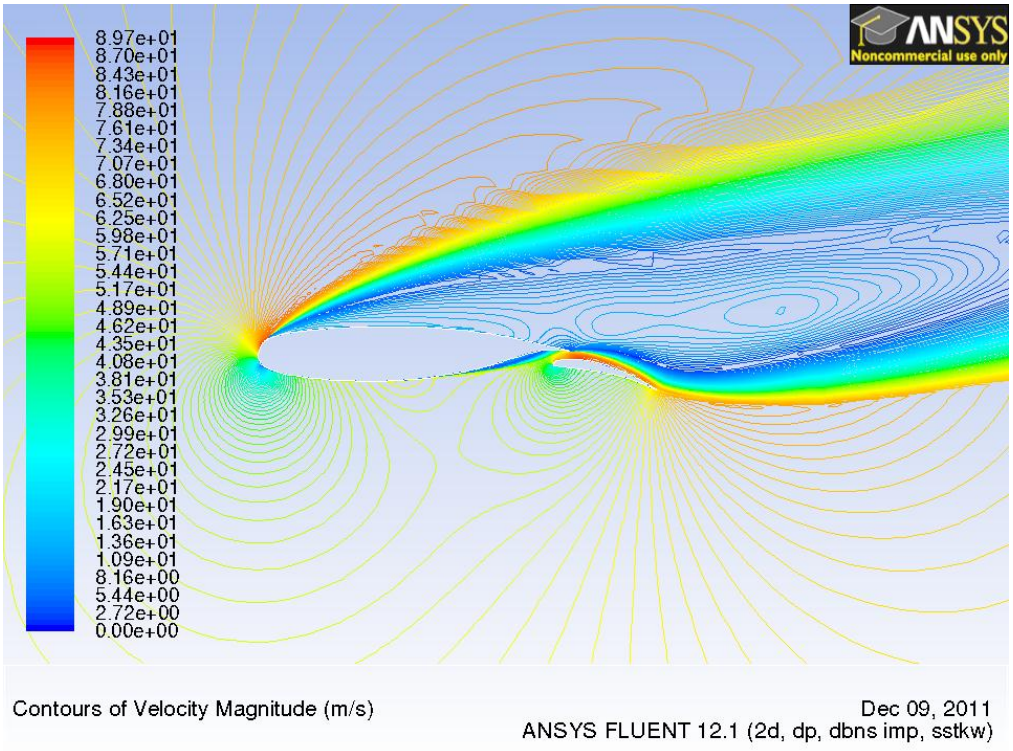

Figure 37 Velocity contours of K-ω SST model initial from 2nd order discretisation

The first order upwind discretisation is used to achieve a reasonable initial flow field, and the second order is for convergence. Figure 38 gives an example of the convergence history of residuals of SA model case. The convergence history of CL and CD of this case are shown in Figure 39 and Figure 40 respectively.

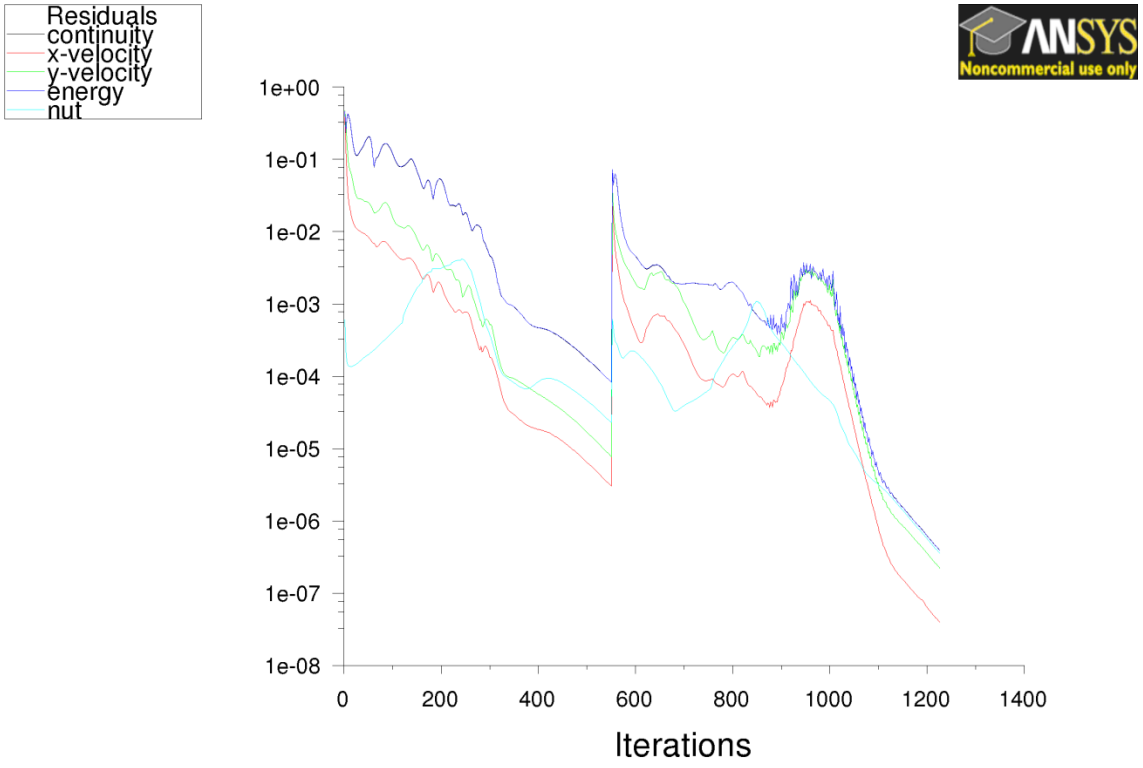

Figure 38 The convergence history of CL of SA model for different grids

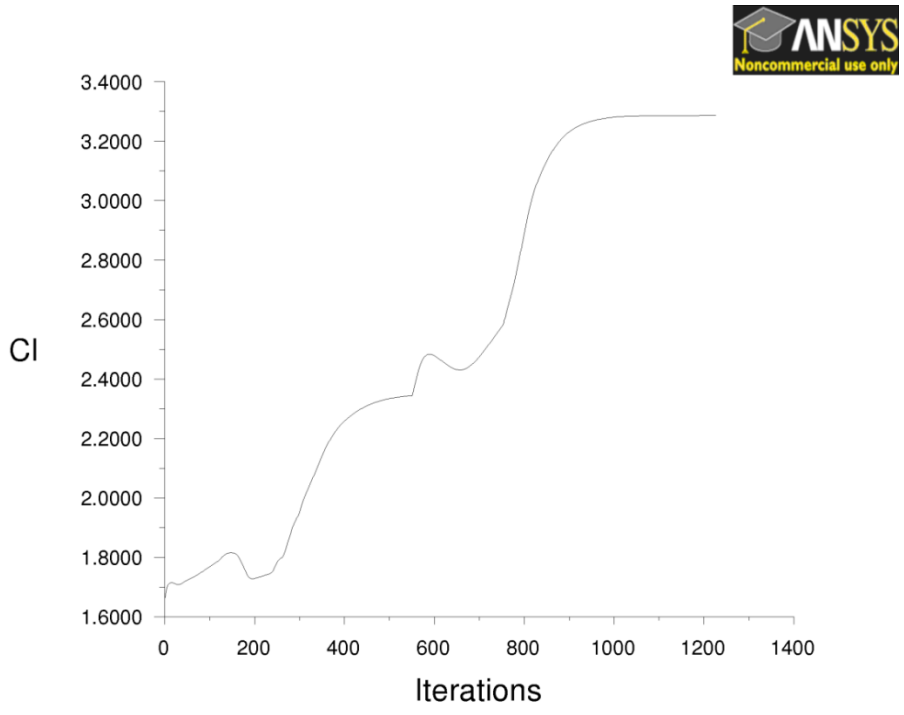

Figure 39 The convergence history of CL of SA model for different grids

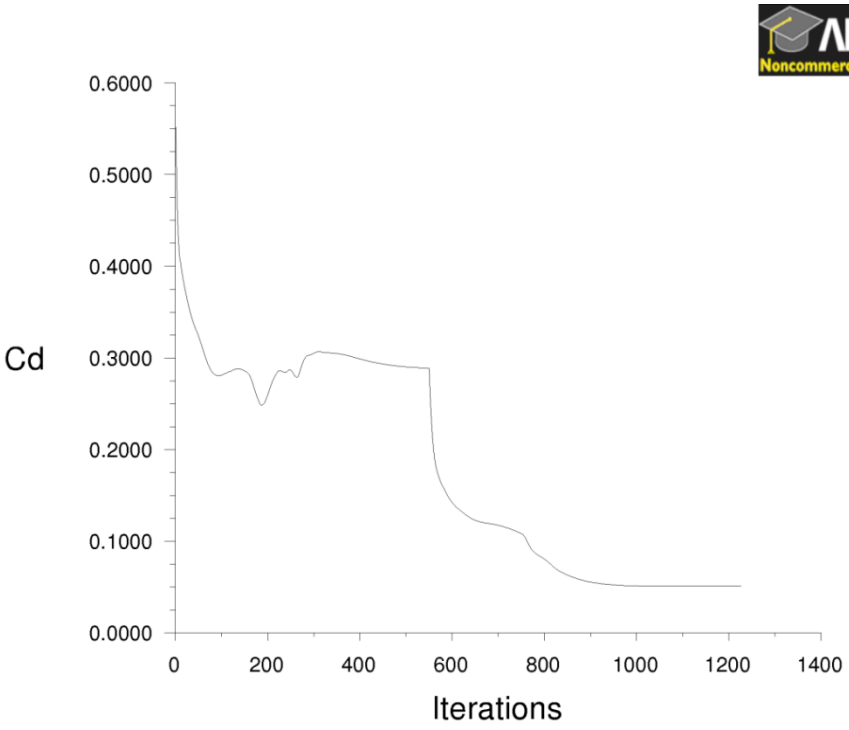

Figure 40 The convergence history of CD of SA model for different grids

The results of all cases are converged with the residuals less than 1E-4. The records of residuals of continuity, energy, X-Velocity, Y-Velocity, K, ω, ε and nut are shown in Table 5. The time costs are already recorded in Table 5. The variations of CL are less than 1E-3 level which is less than 0.03% of the whole CL (see Figure 41). The variations of CD are less than 1E-5 which is less than 0.02% of the whole CD (Figure 42).

Table 5 The residuals of simulations and time cost for different cases

Models	Grids	Continuity	Energy	X-Velocity	Y-Velocity	K	ω	ε	Nut	Time cost
SA	G1	3.8E-7	1.2 E-7	6.8 E-7	3.8 E-7	---	---	---	3.9 E-8	6mins
	G2	1.8E-7	2.1 E-8	1.1 E-7	1.8 E-7	---	---	---	1.8 E-8	10mins
	G3	6.3E-7	2.4 E-8	4.2 E-8	6.2 E-7	---	---	---	3.7 E-7	20mins
K-ω	G1	9.7E-8	2.9 E-8	9.8 E-8	9.6 E-8	9.7 E-8	1.5 E-8	---	---	7mins

SST	G2	7.5E-7	2.6 E-7	1.4 E-7	7.4 E-7	7.3 E-7	1.3 E-7	---	---	13mins
	G3	3.1E-7	1.5 E-8	2.9 E-8	3.1 E-7	7.2 E-8	1.4 E-8	---	---	32mins
K-ε Realizable	G1	1.4E-5	3.7 E-5	9.8 E-5	1.4 E-5	1.5 E-5	---	3.6 E-6	---	5mins
	G2	8.3E-6	8.8 E-6	3.8 E-6	8.3 E-6	6.2 E-6	---	2.2 E-6	---	8mins
	G3	2.7E-5	2.0 E-5	2.8 E-5	2.7 E-5	9.3 E-6	---	1.6 E-5	---	18mins

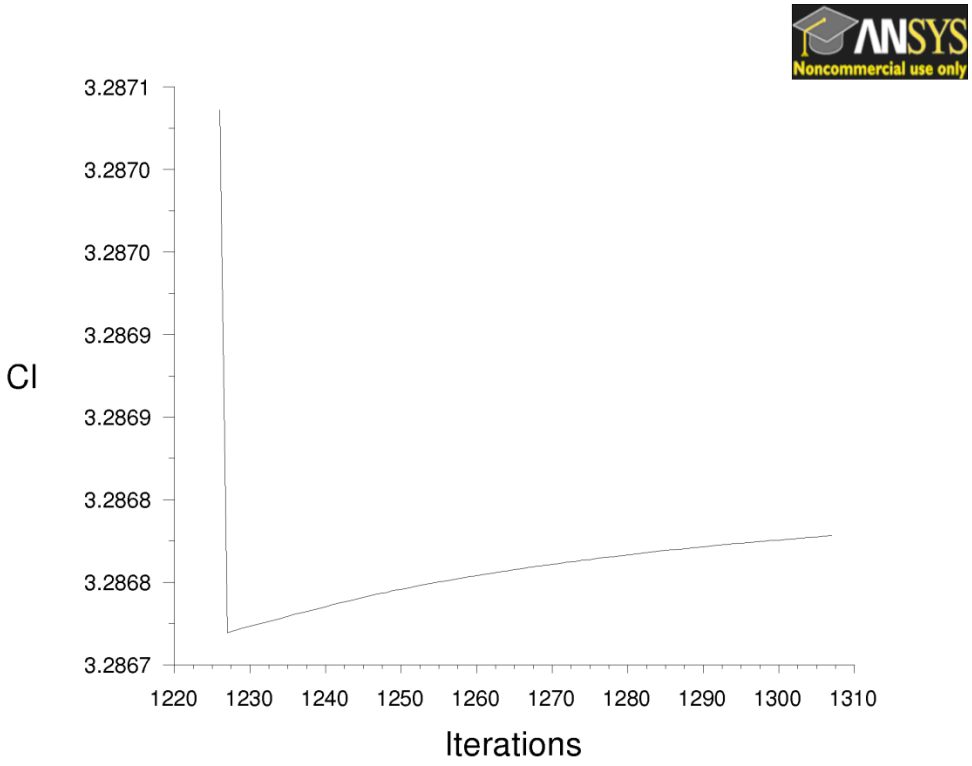

Figure 41 the variations of CL of SA case of G2 at converged state

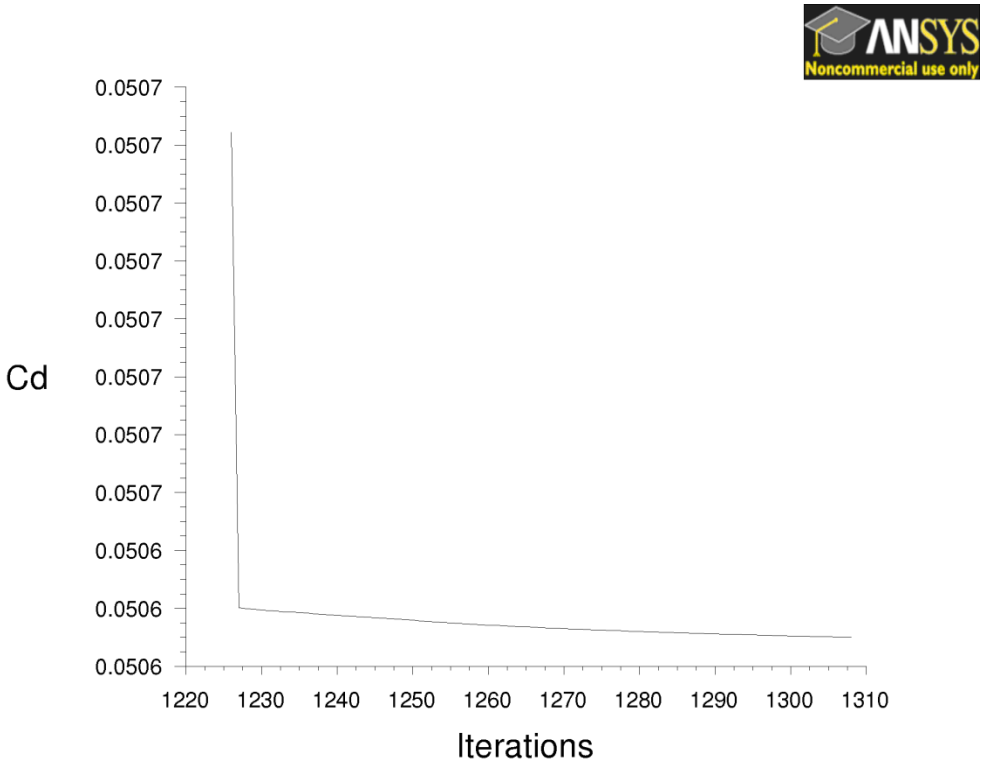

Figure 42 the variations of final CD of SA case of G2 at converged state

2.4.2 Results analysis between turbulence models

2.4.2.1 Flows

The medium mesh G2 is selected to execute the computations in this chapter. The results are then analysed and compared with experiment data for validation.

The application of laminar flow and turbulent flow area guarantee the transition position simulated correctly which can also be observed making sense in the contours of turbulence viscosity around airfoil shown by Figure 43. It can be found that laminar zone are kept correctly in the regions required and turbulence are started from the exact position defined and are developed in a reasonable way.

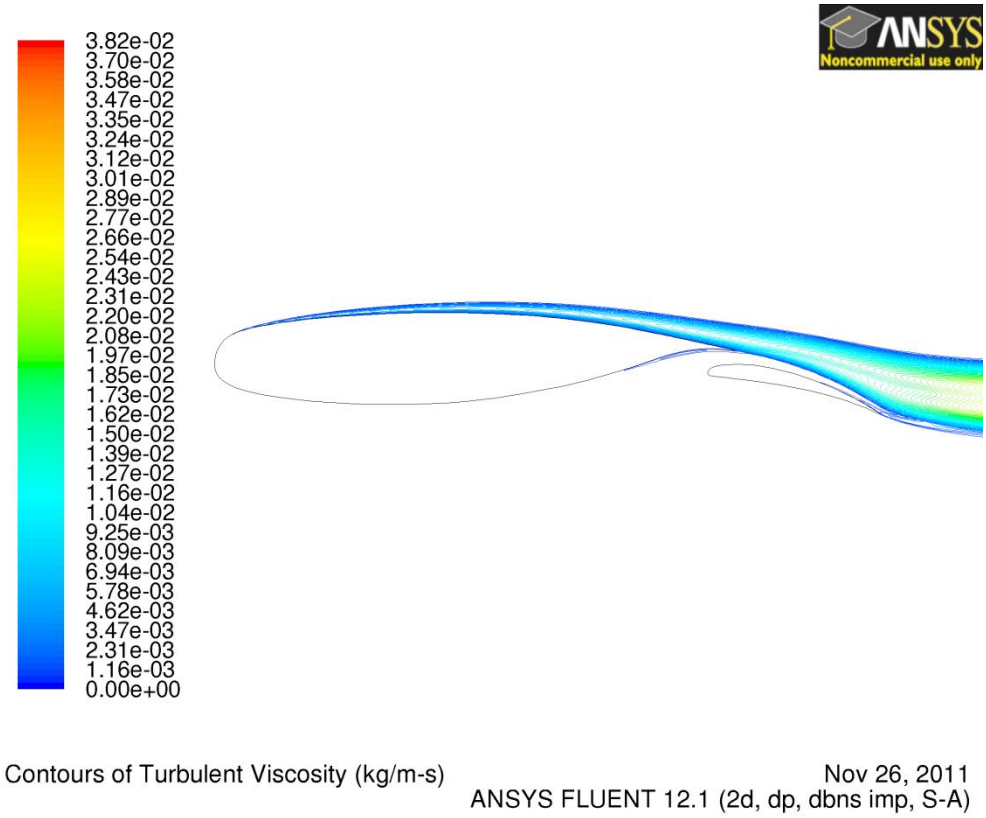

Figure 43 the contours of turbulence viscosity of SA model

As discussed earlier, in general the flows of this case are a mild attached flow. This can be found in the simulations of all three models. Figure 44 shows the velocity contours and Figure 45 shows the flow streamlines around the airfoil for SA model. These figures demonstrate that no obvious separations at the trailing edge of main element and flap have been observed.

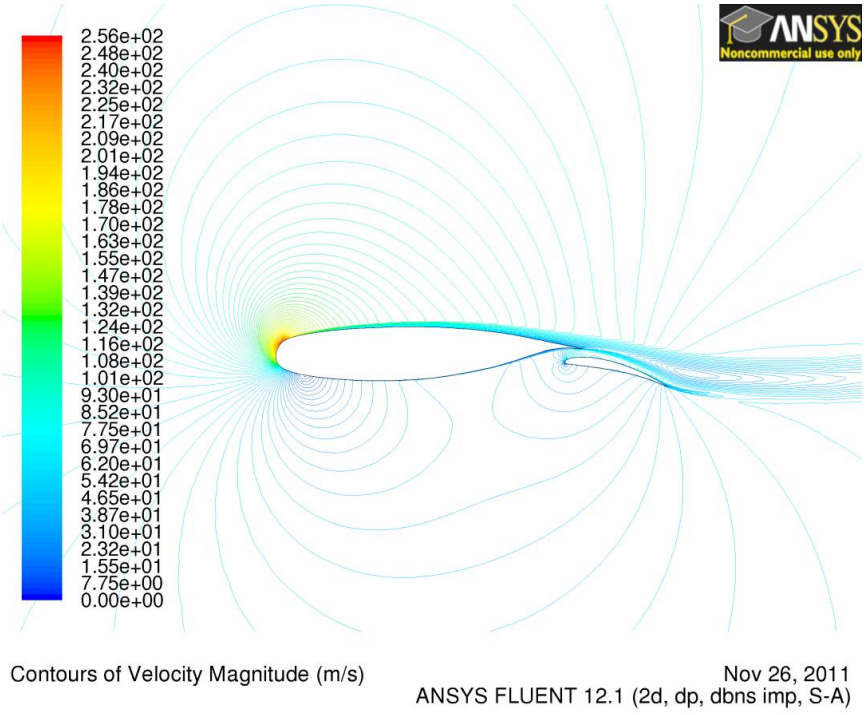

Figure 44 The velocity contours of the velocity of SA model

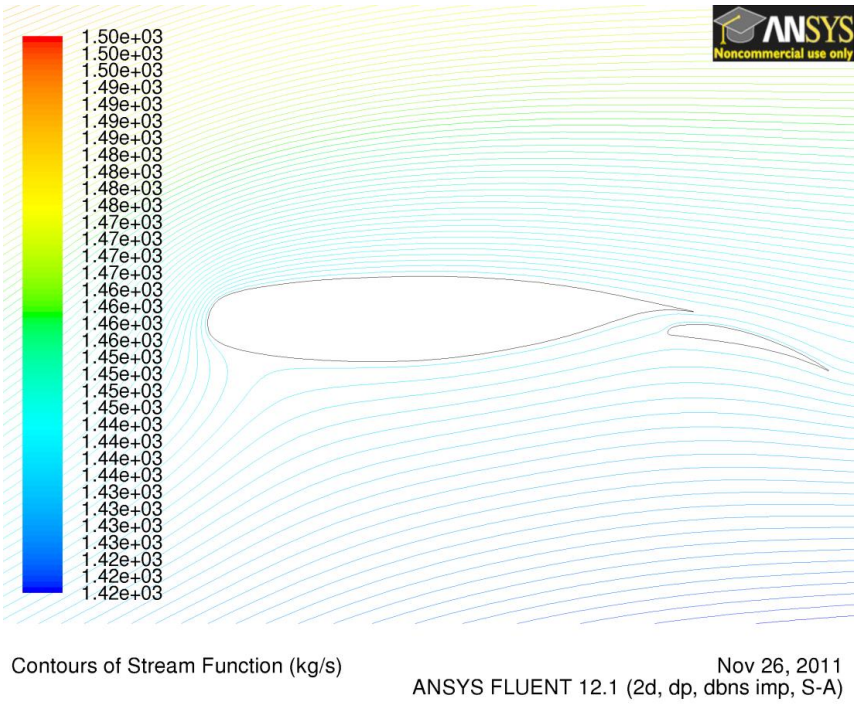

Figure 45 Streamline contours around the airfoil of SA model of G2

The main feathers of the flows include laminar separation bubble on leading edge, cove separations and confluents over flap.

Laminar bubble separation can be found by all three turbulent models at suction peak area which is on the upper surface of leading edge at the area of about 2.1%-3% chord. Figure 46shows the velocity profiles around this area of SA model and adverse flows can be observed.

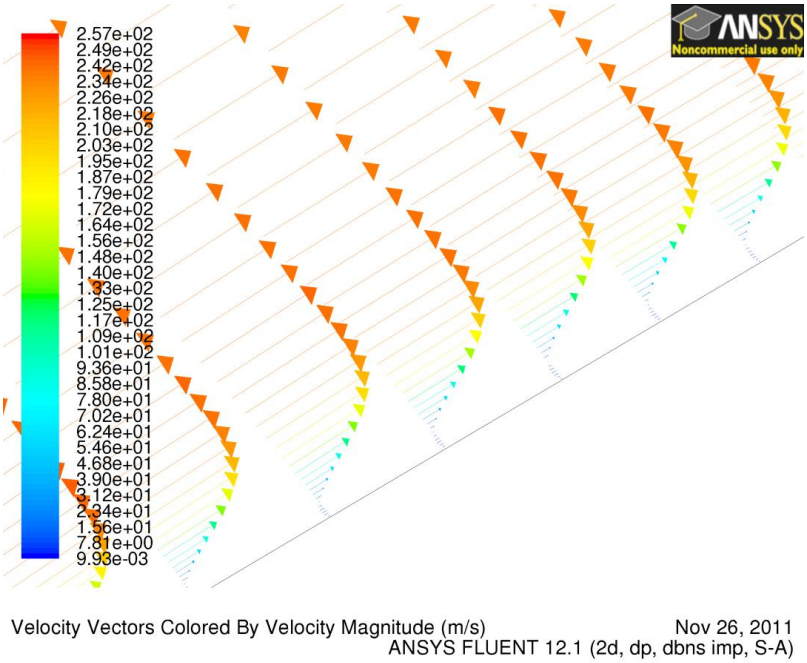

Figure 46 The velocity profile of SA models

Cove separation is another challenge to the prediction of this case. At the origin of the design of NLR7301 two-element airfoil, the cove area has been processed as smooth as possible to avoid cove separations, however, limited-intension cove separations have still been observed on the lower surface of main element of 71%-75% chord in the simulations. This separation can be captured by all three turbulent models. Figure 47 shows the cove separations captured by SA model.

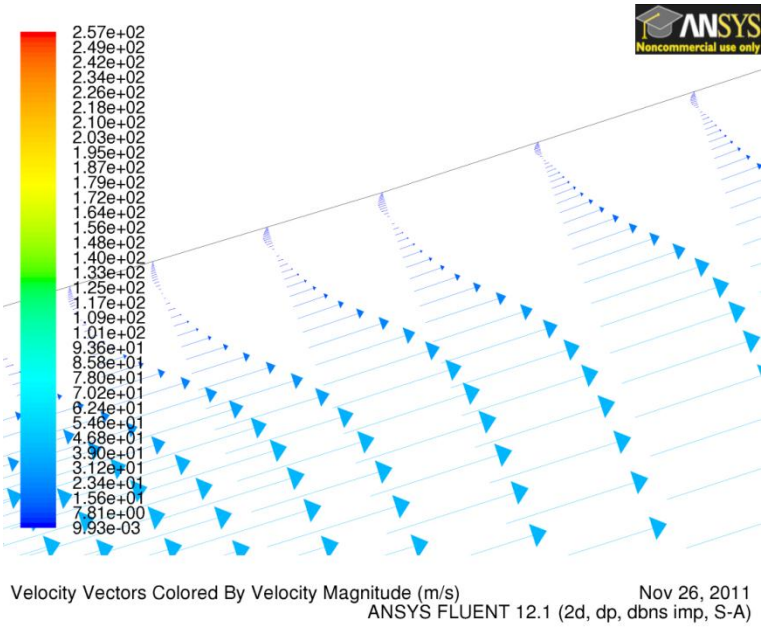

Figure 47 The cove separations captured by different turbulent models

Confluent flows over flap are the main flow feature of the case. Figure 48 shows the velocity profiles of SA model of G2 grids and confluent flows can be clearly observed.

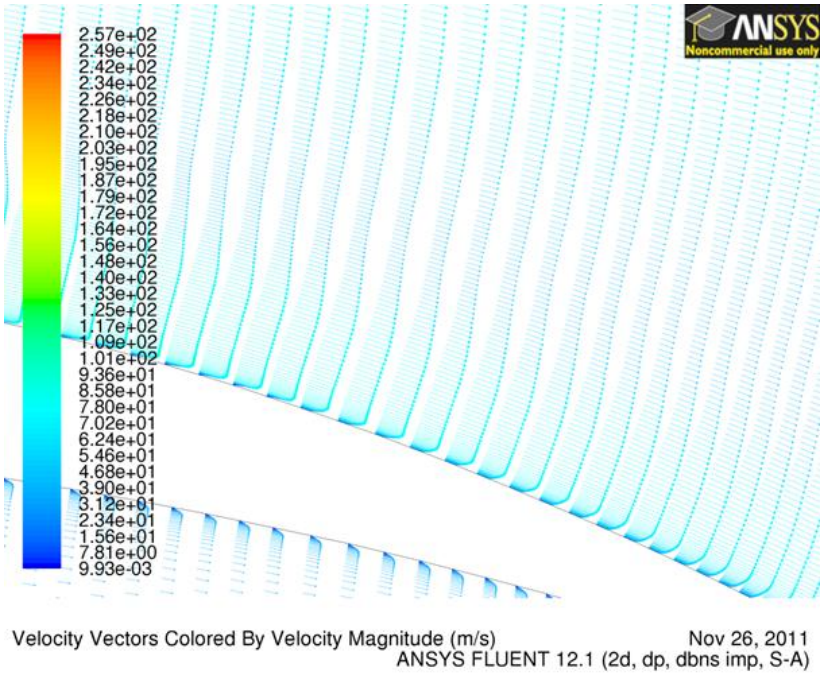

Figure 48 The confluent flows of SA models of G2 grids

All turbulent models can capture these typical flows. However, to clarify the differences between these models, focus has centred on the internal boundary layer. Different turbulent models predict different characters of the boundary layers. Though the global flow pattern predicted by turbulent models are quite similar, differences relating to the internal boundary layer are still observed owing to the different modelling of flow physics by different turbulent models.

Figure 49- Figure 51 shows the velocity profiles of several stations on the upper surface of main element. ST1 is at the end of laminar flow on upper surface and the 0.0295 chord in x direction. ST2 is at the biggest thickness point of upper surface of main element. ST8, ST12, ST13, ST14, ST16 are defined as the same position as in experiment which can also be found in Figure 30. Differences can be observed at every station. At ST1 the thicknesses of the boundary are quite close to each other, yet K-ε Realizable predicts a slightly thicker boundary layer than the other two models, thus its suction peak maybe the highest owing to the formation of a lager leading edge radius. The velocity gradient normal to the wall of K-ε Realizable model is greater than SA and K-ω SST model which will result in a higher friction coefficient. The “velocity losses” of three models at ST1 are very close to each other. At ST2 and ST3 similar results can be observed. The thicknesses of boundary layer of different turbulent models are very close to each other. So the pressure distribution of these areas may be very similar. In terms of the velocity gradient normal to the wall, K-ε Realizable model predicts the highest value and K-ω SST model predicts the second; this may reveal the sequence of friction coefficients between these models. In terms of velocity losses, K-ω SST model predicts the most serious losses which may introduce highest pressure drag. SA model has the least velocity loss and may have the lowest pressure drag.

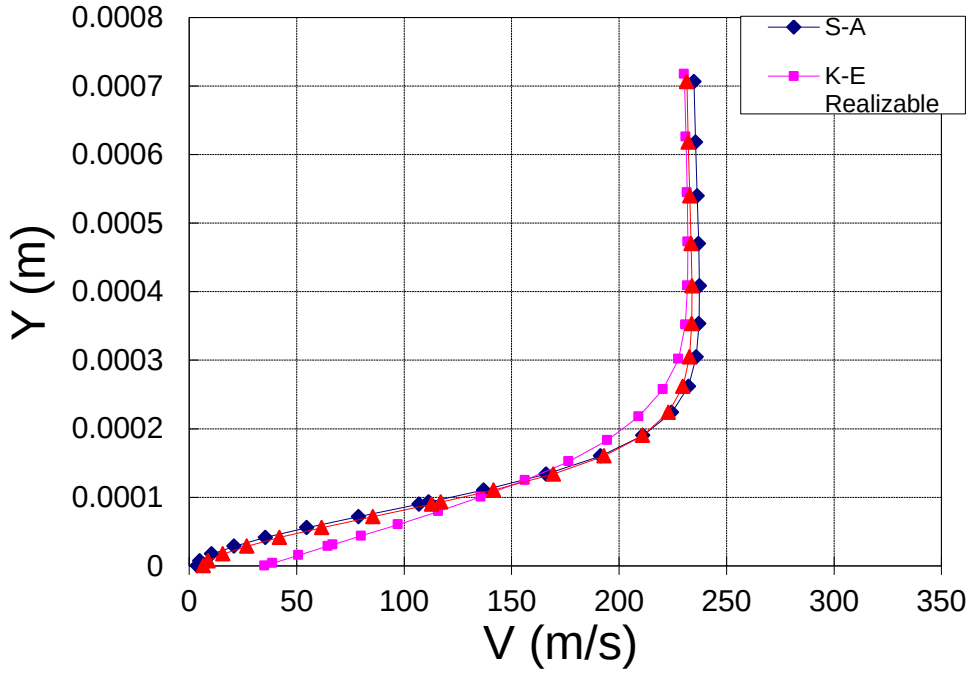

Figure 49 The velocity profile at ST1 between different turbulent models

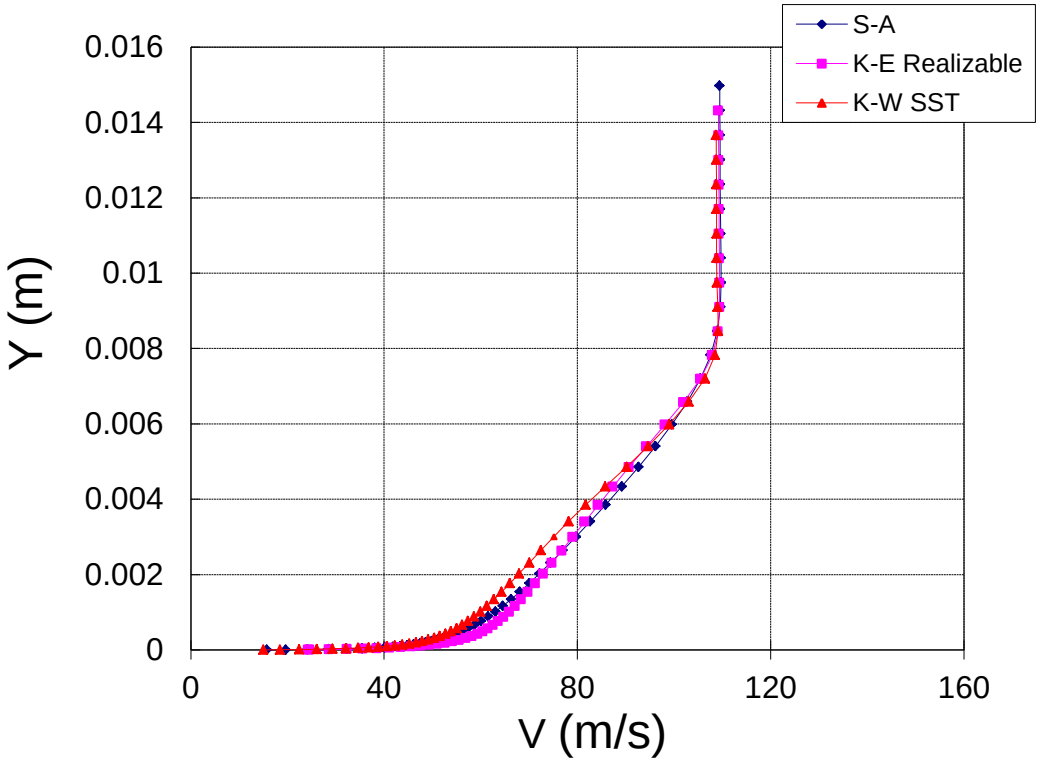

Figure 50 The velocity profile at ST2 between different turbulent models

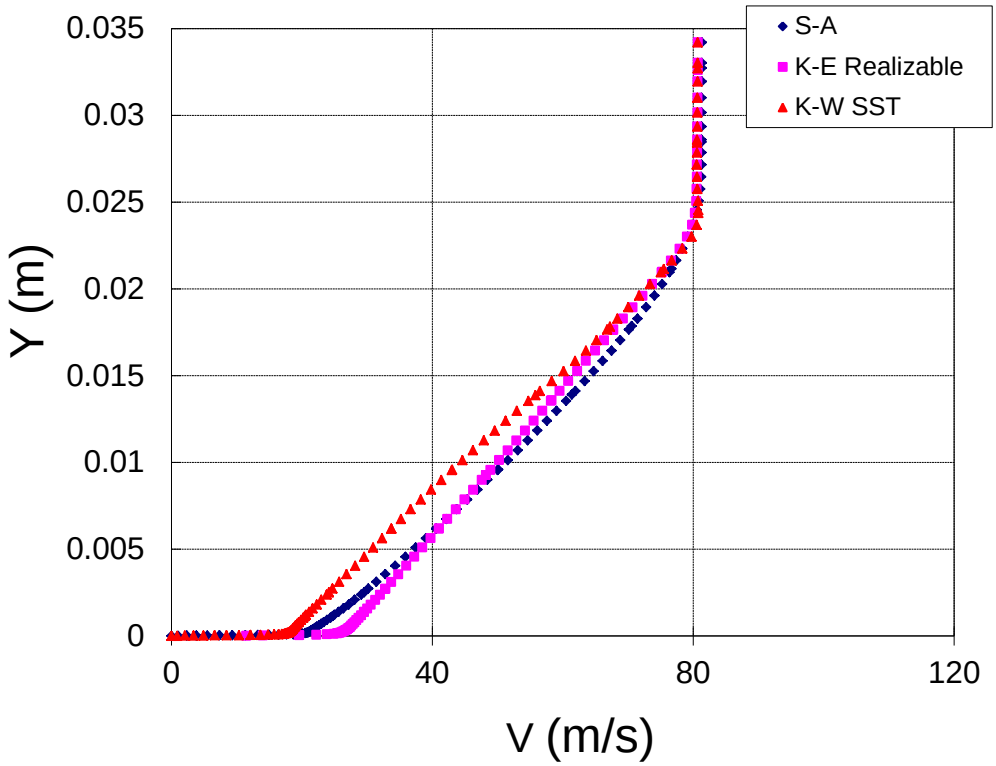

Figure 51 The velocity profile at ST8 between different turbulent models

In the areas above flap, confluent is the dominant flow. The velocity profile of several stations which are identical to the experiment has been abstracted and compared with each other (see Figure 52 – Figure 55). The obvious difference should be the velocity losses. At all stations K-ω SST model predicts the highest losses and SA model predicts the lowest losses. This results show that most probably K-ω SST model may have the highest pressure drag and SA model has the lowest. It can also be found that K-ω SST model and K-ε Realizable model predict a very similar flow through the gap and below, as the difference between them mainly arose from the shed of boundary layer of upper surface of main element.

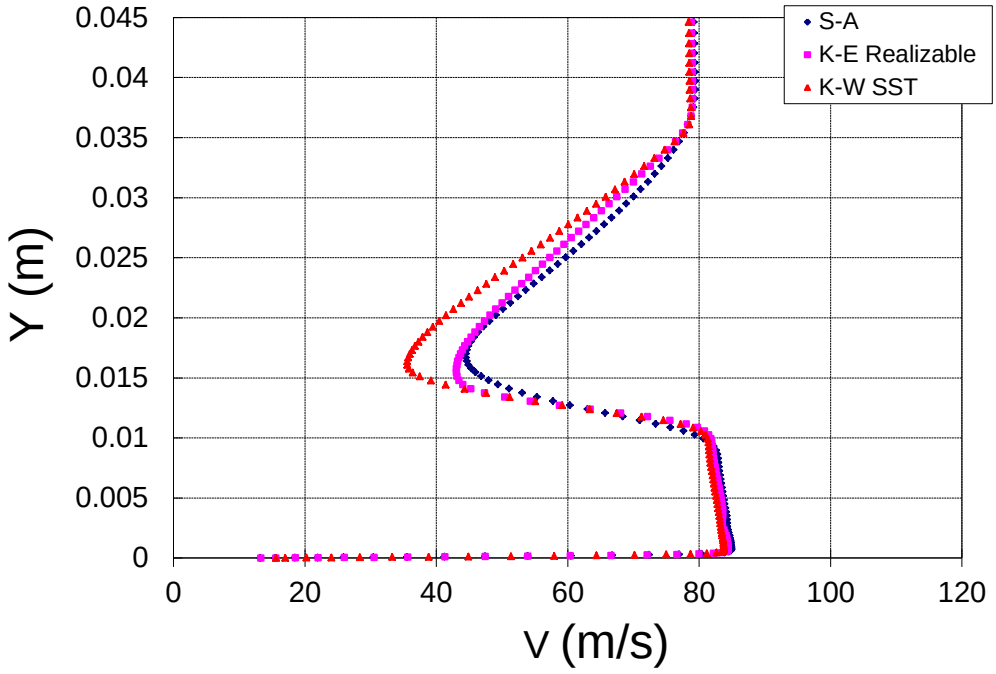

Figure 52 The comparison of the velocity profiles over flap between different turbulent models and experiments at ST12

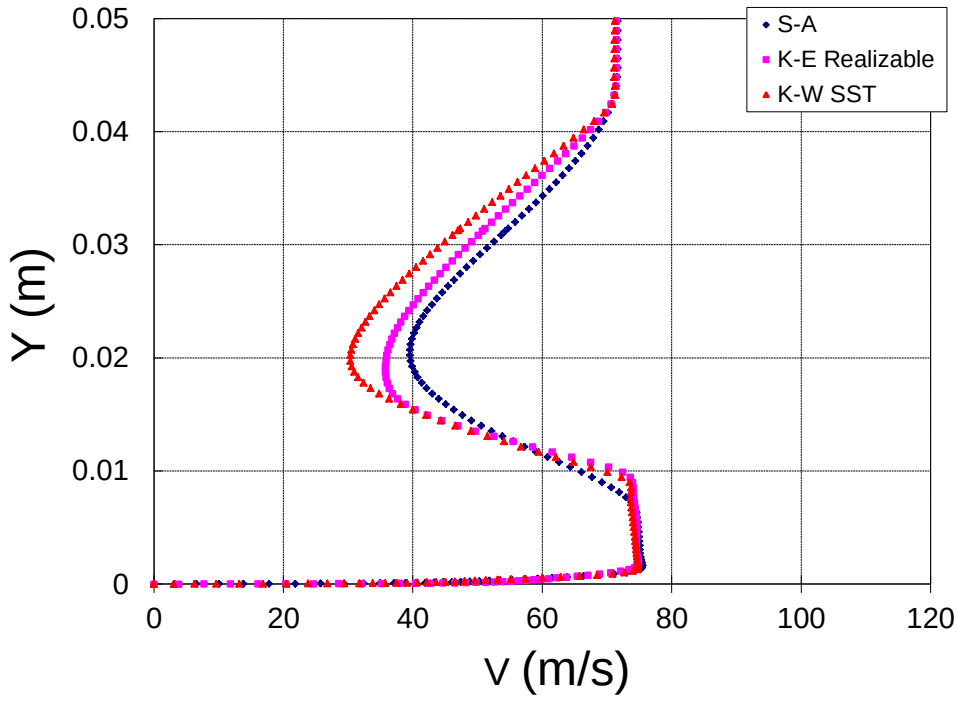

Figure 53 The comparison of the velocity profiles over flap between different turbulent models and experiments at ST13

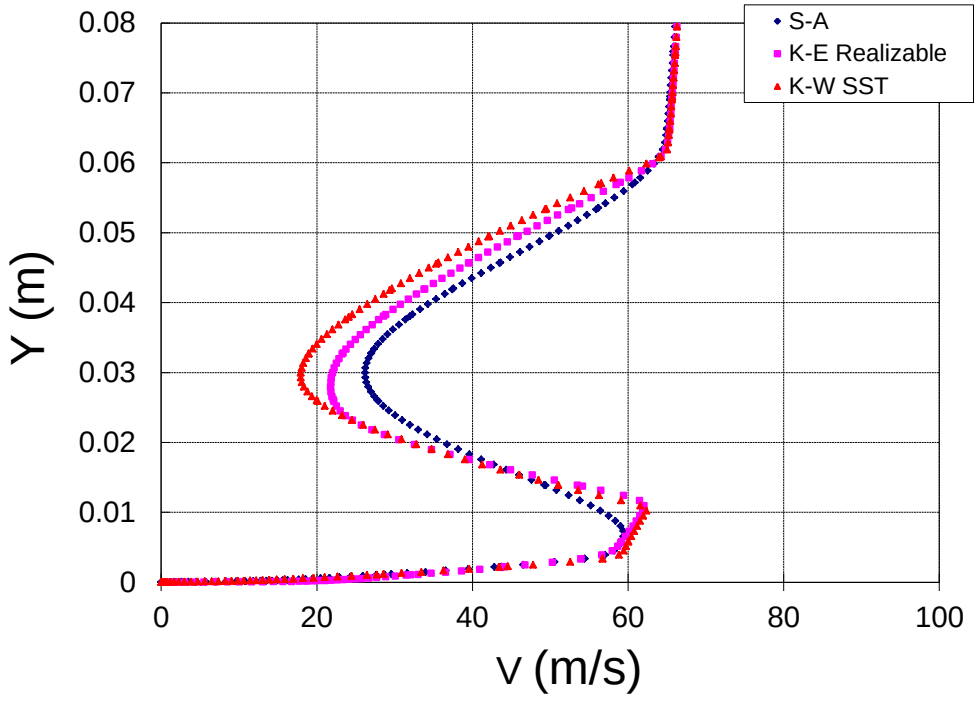

Figure 54 The comparison of the velocity profiles over flap between different turbulent models and experiments at ST14

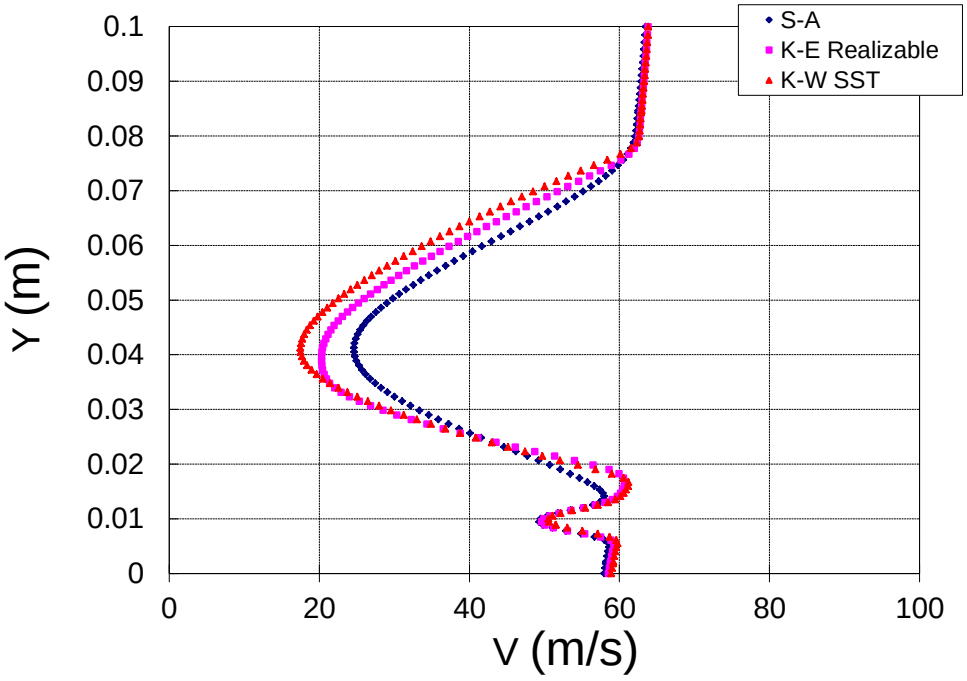

Figure 55 The comparison of the velocity profiles over flap between different turbulent models and experiments at ST16

2.4.2.2 Pressure distributions

Figure 56 shows the comparison between simulation results of different turbulent models and experiment data on pressure coefficient for G2 grid. Generally speaking, all three turbulent models can predict quite accurately on Cp. Figure 57 shows the detailed Cp distribution on the leading edge. It can be found that the differences of Cp between simulations and experiment are lower than 0.5 which may mean the suction peak can be fully captured by these turbulent models. Figure 58 shows the detailed comparison of Cp around flap. It can be found that the agreements of calculated results compared to experiment data are still good enough and the difference between turbulent models and experiment are lower than 0.3. The differences between models are the same level with differences between models and experiment data, which means three turbulent models can predict Cp accurately.

Between turbulent models, the simulation qualities on Cp of different turbulent models are of the same level. The differences between the results of different turbulent models cannot be obviously identified. This maybe because the boundary layer thickness predicted by different turbulent models are quite close to each other and, as discussed above, the difference of velocity profile have no effect on pressure coefficient.

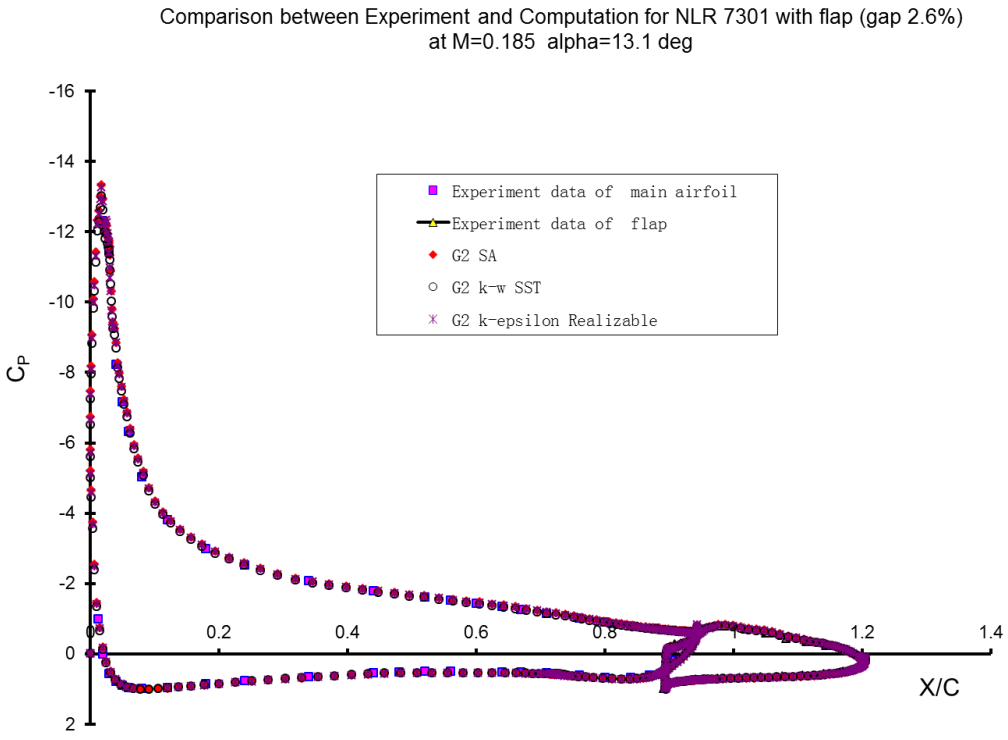

Figure 56 Comparison between simulation results of different models on modified G1 grids with transition simulated in main element

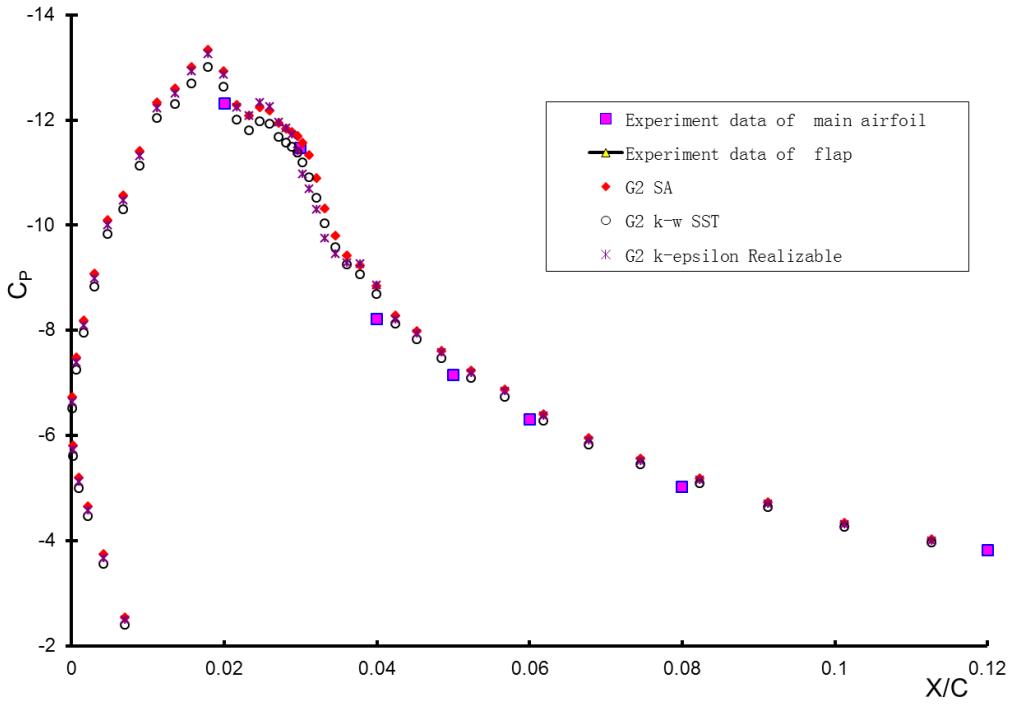

Figure 57 Detailed show in leading edge of Fig 56

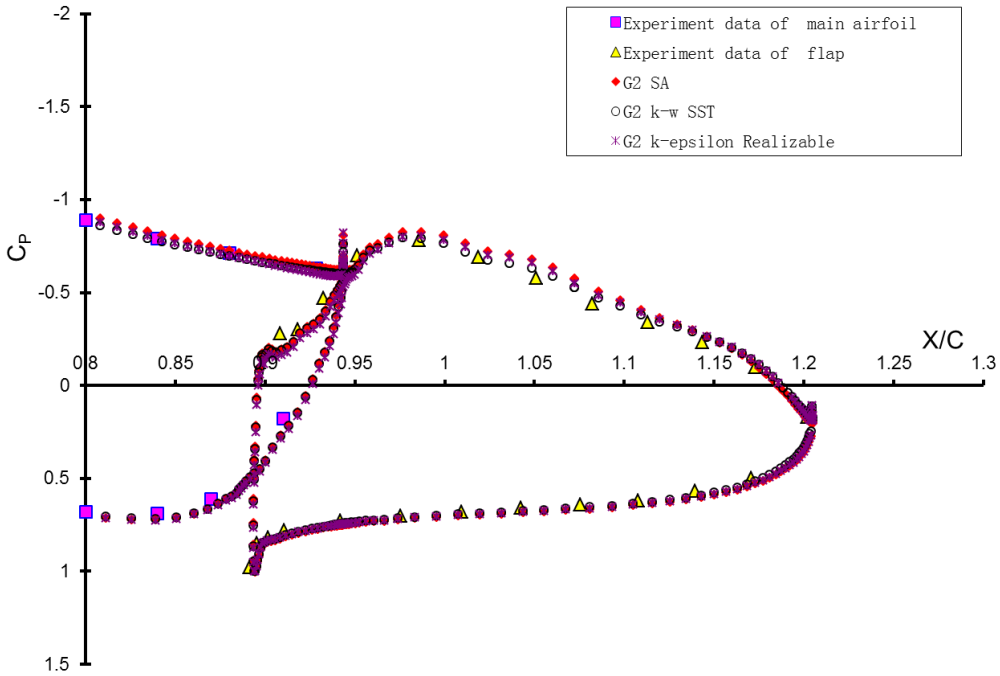

Figure 58 Detailed show in trailing edge of Fig 56

2.4.2.3 Skin friction distributions

Figure 59 shows the comparison of skin friction coefficient (Cf) between simulation results and experiment data. It can be found that the agreements between simulations and experiments are generally good. SA model and K-ω SST model are similarly accurate in predicting Cf. K-ε Realizable model over-predicts Cf to some extent which agrees with the conclusion in reference [20]. This might be from the reason mentioned above that enhanced wall functions over- predict velocity gradient normal to wall more intense which is shown in Figure 49 - Figure 55. The biggest difference between turbulent models and experiments is on the cove separation area on the lower surface of the main element where Cf is not fully captured.

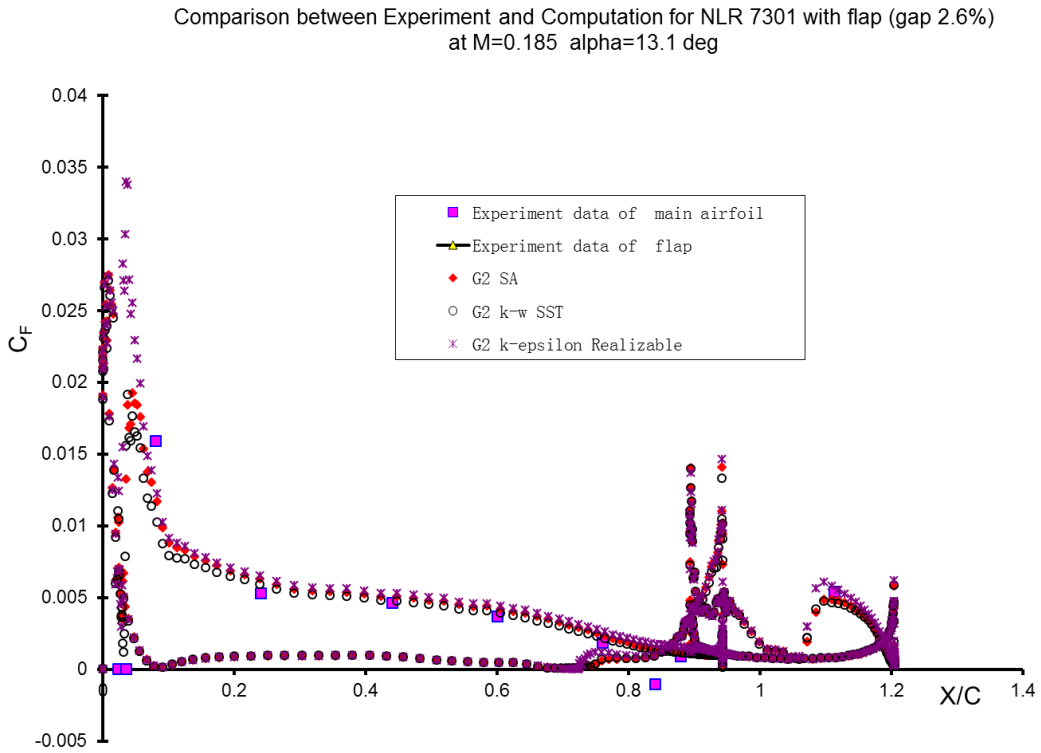

Figure 59 Comparison between simulation results obtained with different models on G2 grids and experimental data on Cf

2.4.2.4 Lift and drag

Table 6 gives the CL, CD and comparisons between three turbulent model results and experiment data for G2 grid. It can be found that SA models yield best results on the prediction of CD with the accuracy of 13.78%, but over-predict the CL with accuracy of 4.65%. K-ω SST model predict CL most accurately with the accuracy of 2.36% and over-predict the CD mostly. K-ε Realizable model has the moderate results for both CL and CD with the accuracies of 3.66% for CL and 16.58% for CD.

The relevance can be found that SA model has the most accurate CD and lowest velocity losses. This may reveal that the over-prediction of drag may originate mainly from the over-prediction of velocity losses for three RANS models.

Table 6 CL and CD of three turbulent models and their comparison with experiments

Models	CD	∆ CD% over experiments	CDP	CDf	CL	∆ CL% over experiments
SA	0.05062	13.78%	0.04362	0.00701	3.287	4.65%
KW –SST	0.05363	20.52%	0.04693	0.0067	3.215	2.36%
KE-Realizable	0.05188	16.58%	0.04411	0.00777	3.256	3.66%
Experiment	CD=0.0445				CL=3.141	

2.5 Grid dependency

Before coupling CFD solvers to multi-objective optimization, grids dependency is performed to pick up the proper grids to be used in the optimisation. In this study three different meshes which are G1, G2 and G3 and defined in chapter 2.2 are calculated with three RANS turbulent models, SA, K-ω SST and K-ε Realizable.

2.5.1 Sensitivity of fine mesh G3

Fine mesh in this study is found to be a fairly sensitive grid. It might be the leading edge laminar separation bubble which is highly sensitive and has the effect on the downstream boundary layer thickness that introduces the sensitivity to the whole flow field. A fine grid created which is quite close to the final fine mesh is found to converge at an unreasonable state and is presented in Appendix B with the calculation of K-ω SST model. The final fine mesh is generated by very careful adjustment from basic grid G2 and can be qualified to predict the correct flow of this case.

2.5.2 Cp

The comparisons between results of different cell numbers of SA model are shown in Figure 60. Generally speaking, the agreements between computations of all three grids and experiments are quite well. The difference of Cp between experiments and simulations are less than 0.5 in most areas and less than 1 in suction peak.

Between different grids, it can be found that the discrepancies mainly come from leading edge area and trailing edge area. Figure 61 gives the zoomed-in figures of the leading edge. However, the discrepancies are rather small and are less than the discrepancy between simulations to experiment. All pressure results are very close to experiments. The same result can also be found on the trailing edge area which is shown in Figure 62.

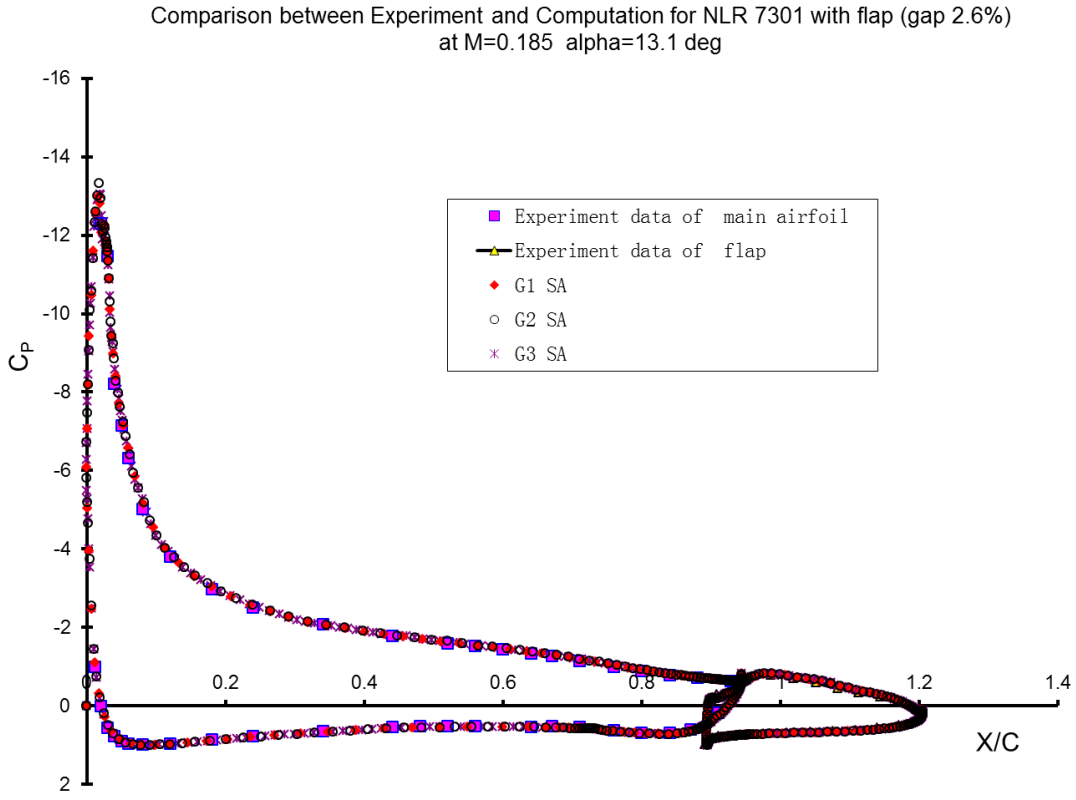

Figure 60 Comparison of CP between different grids and experiment for SA model

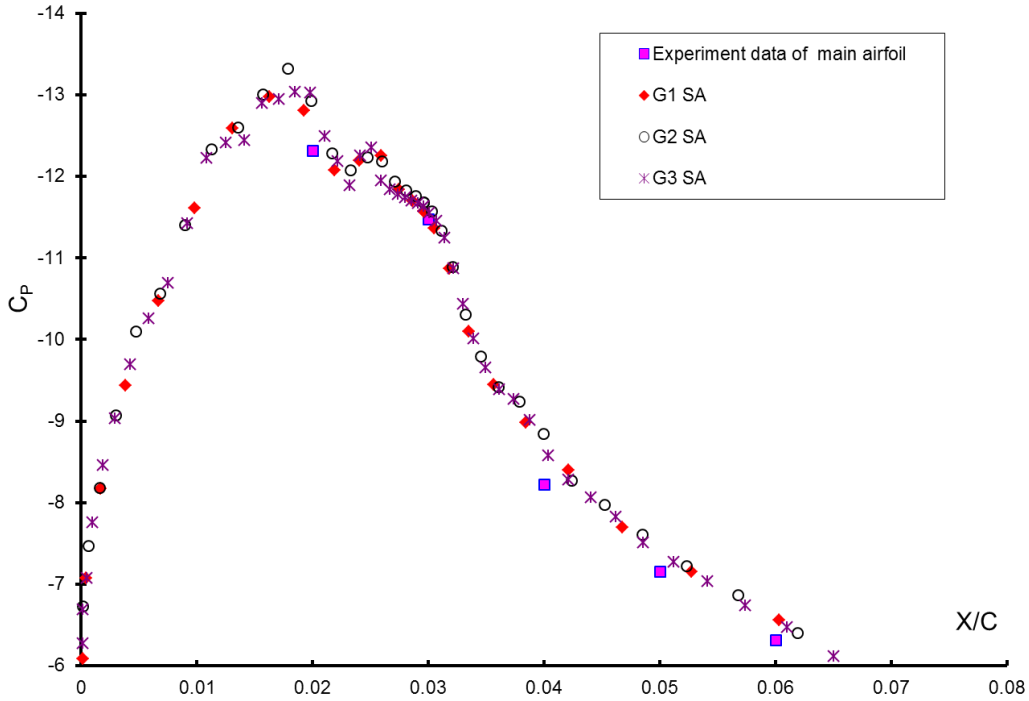

Figure 61 Comparison of CP on leading edge (zoomed in figure)

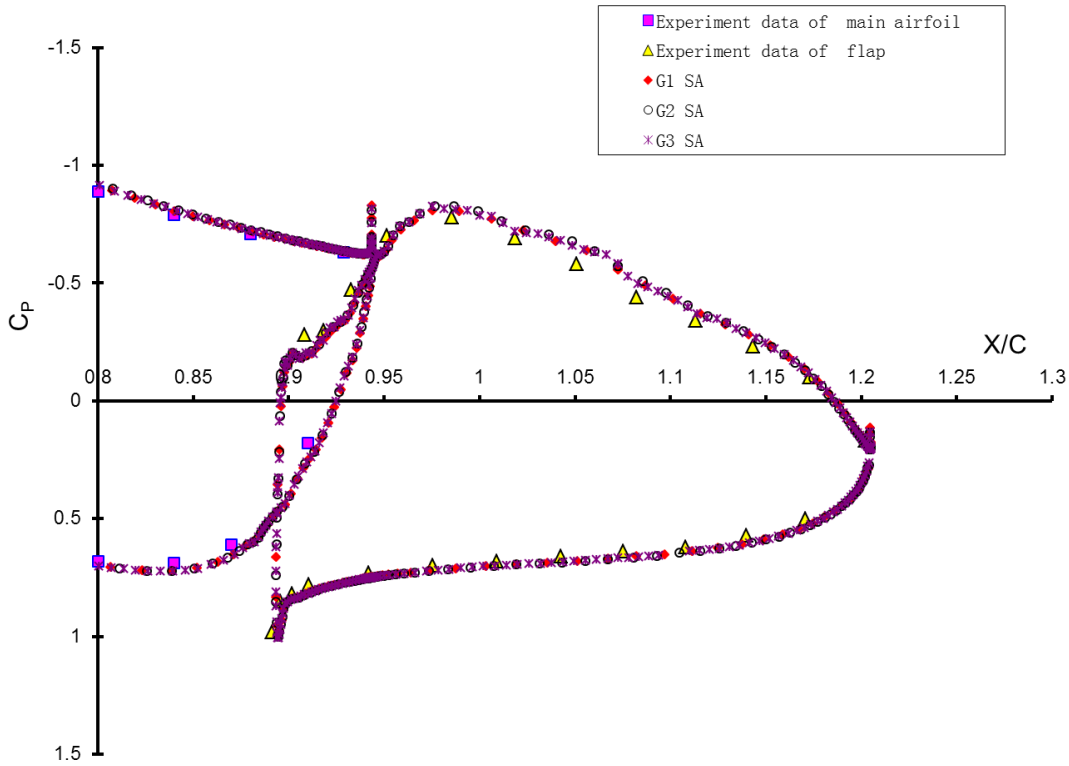

Figure 62 Comparison of CP on trailing edge (zoomed in figure)

From the perspective of pressure, the differences between grids are really small, even coarse grids can capture the pressure distribution around airfoil which suggests that all grids are converged to predict pressure.

2.5.3 Yplus and Cf

Yplus represents the first layer distance of the mesh. Figure 63 shows the comparisons of Yplus of different grids for SA model. It can be found clearly that the Yplus values decrease correctly when grids density increases. The maximum value of Yplus is about 2.15, in most areas the Yplus values are close to or lower than 1. So the target of Yplus of 1 can be seen as fulfilled.

Figure 64 - Figure 66 show the comparisons of Cf between different grids and experiments. It can be found that three grids have similar capacity to predict Cf, and medium grid has the very slightly higher value. However, the discrepancies between different grids are rather small as all have the same accuracy compared to experiment data.

Thus from the perspective of Cf, all three grids have similar reasonable results. It may mean that all grids are converged to predict Cf.

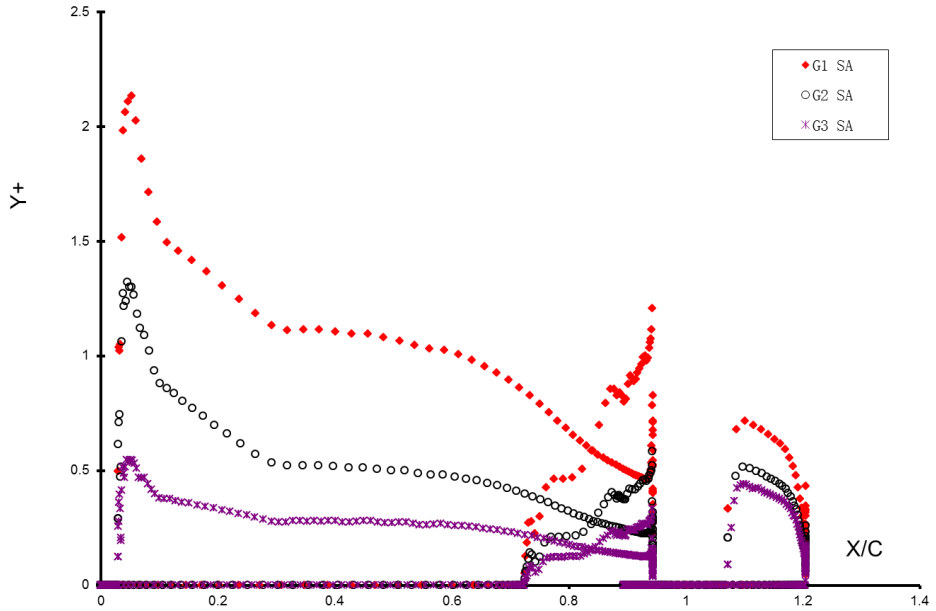

Figure 63 Comparison of Yplus between different grids for SA model

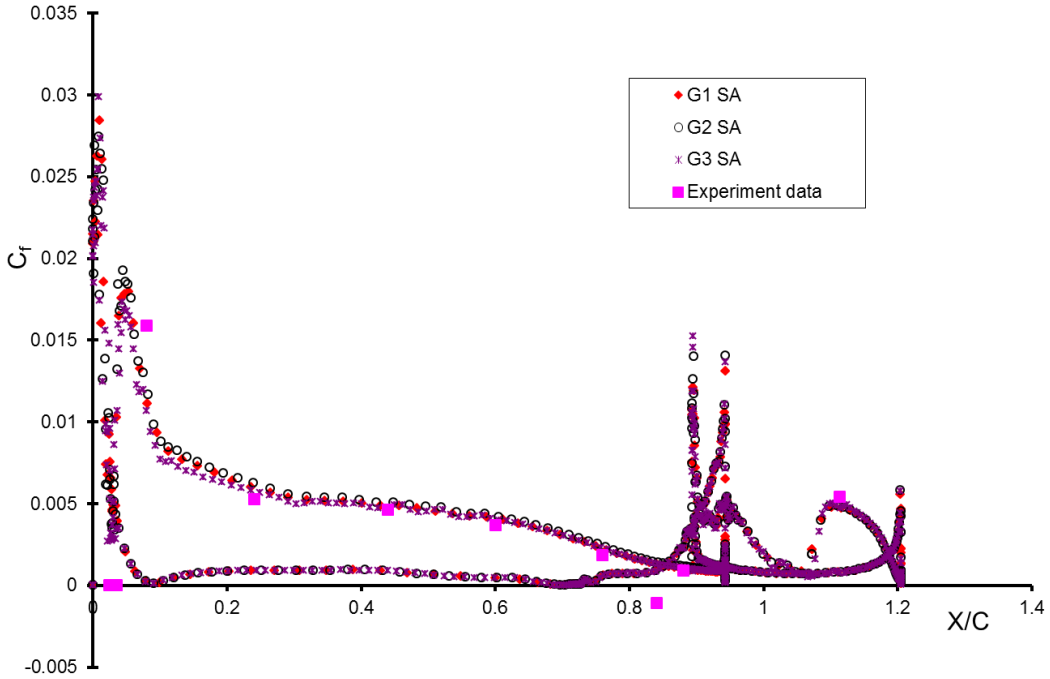

Figure 64 Comparison of Cf between different grids and experiments for SA model

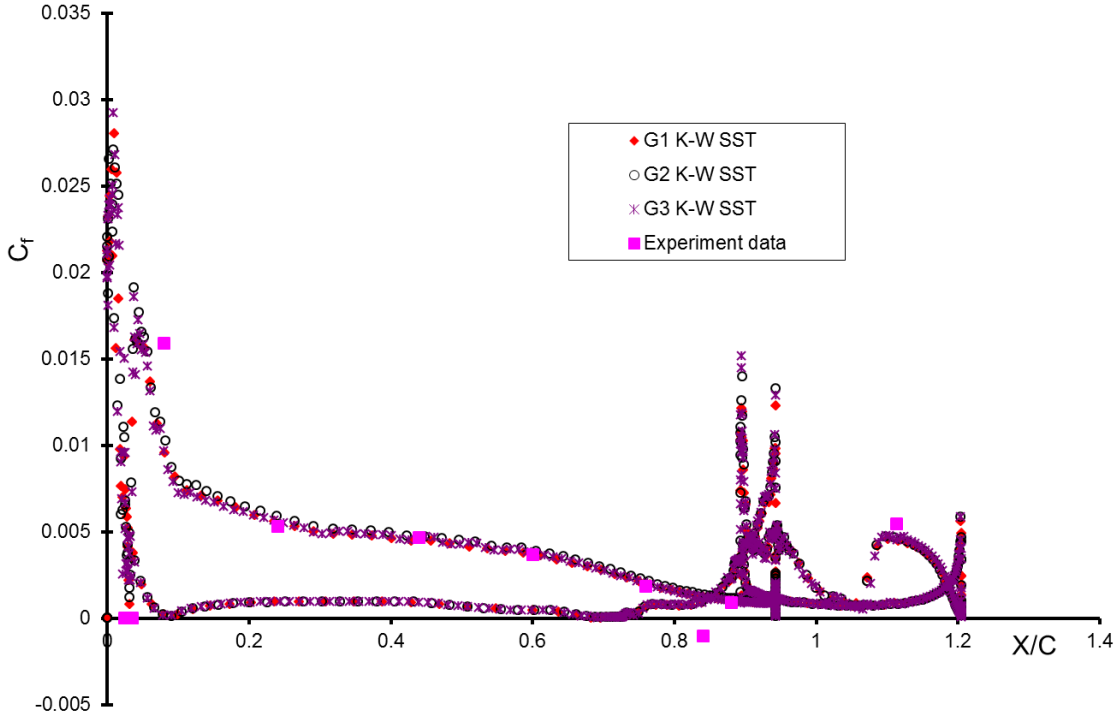

Figure 65 Comparison of Cf between different grids and experiments for k-ω SST model

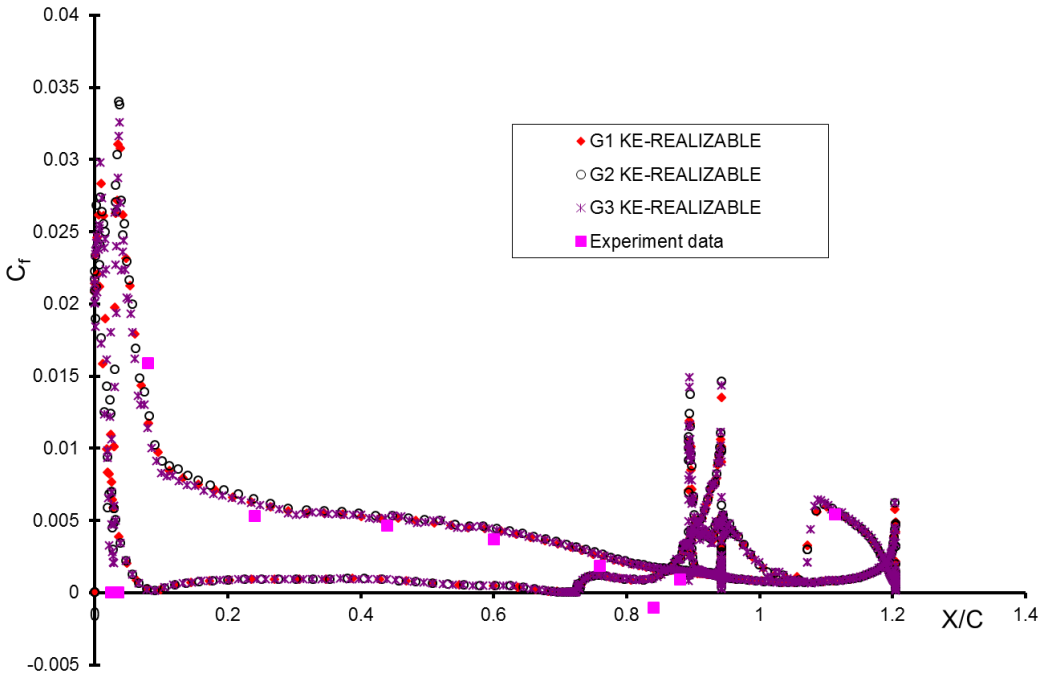

Figure 66 Comparison of Cf between different grids and experiments for k-ε Realizable model

2.5.4 CL and CD

The CL and CD results for different models and grids are collected in Table 7. For lift characters, it can be found that the CL values of all the grids and models are very close to experiment data with accuracies less than 5%. It can also be found that CL increases from G1 to G2 and then decreases from G2 to G3. For drag characters, the accuracies between computations and experiments are between 13.78% and 28.36%. It can be found that with the increasing cell numbers, CD and CDf firstly decreases from G1 to G2 and then increases from G2 to G3, which is the relevant pattern with CL. The difference between G2 and G3 is less than that between G1 and G2 for SA model and K-ε Realizable model and can be observed in Figure 67 - Figure 69.

Investigations have been applied to check the components of CD which includes CDp and CDf. Figure 70 –Figure 72 show the results of CDp and CDf with bar charter of SA model; K-ω SST model and K-ε Realizable model

respectively. It can be found that CDf remains relatively stable when cell numbers increase. For all three turbulent models, the difference between G2 and G3 are less than that between G1 and G2. And it can also be found that G2 has the lowest CDp which is relevant to it having the highest value of CL and highest suction peak.

Table 7 The CL&CD of different models and grids

Models	grids	CD	∆ CD% over experiments	CDP	CDf	CL	∆ CL% over experiments
SA	Grid1	0.0538	20.90%	0.04693	0.00687	3.264	3.92%
	Grid 2	0.05063	13.78%	0.04362	0.00701	3.287	4.65%
	Grid 3	0.05199	16.83%	0.04537	0.00662	3.273	4.20%
KW - SST	Grid1	0.05617	26.22%	0.04971	0.00646	3.2	1.88%
	Grid 2	0.05363	20.52%	0.04693	0.0067	3.215	2.36%
	Grid 3	0.05712	28.36%	0.05068	0.00644	3.175	1.08%
KE-Realizable	Grid1	0.05513	23.89%	0.04752	0.00761	3.229	2.80%
	Grid 2	0.05188	16.58%	0.04411	0.00777	3.256	3.66%
	Grid 3	0.05297	19.03%	0.04549	0.00747	3.243	3.25%
Experiment		CD=0.0445				CL=3.141	

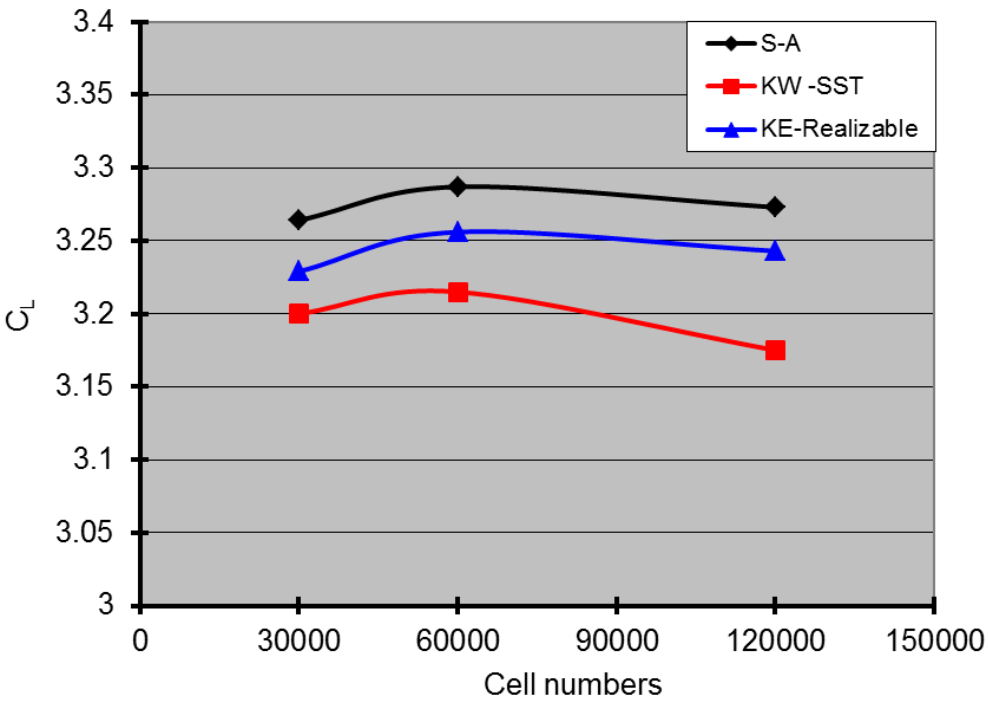

Figure 67 CL vs Cell numbers for different models

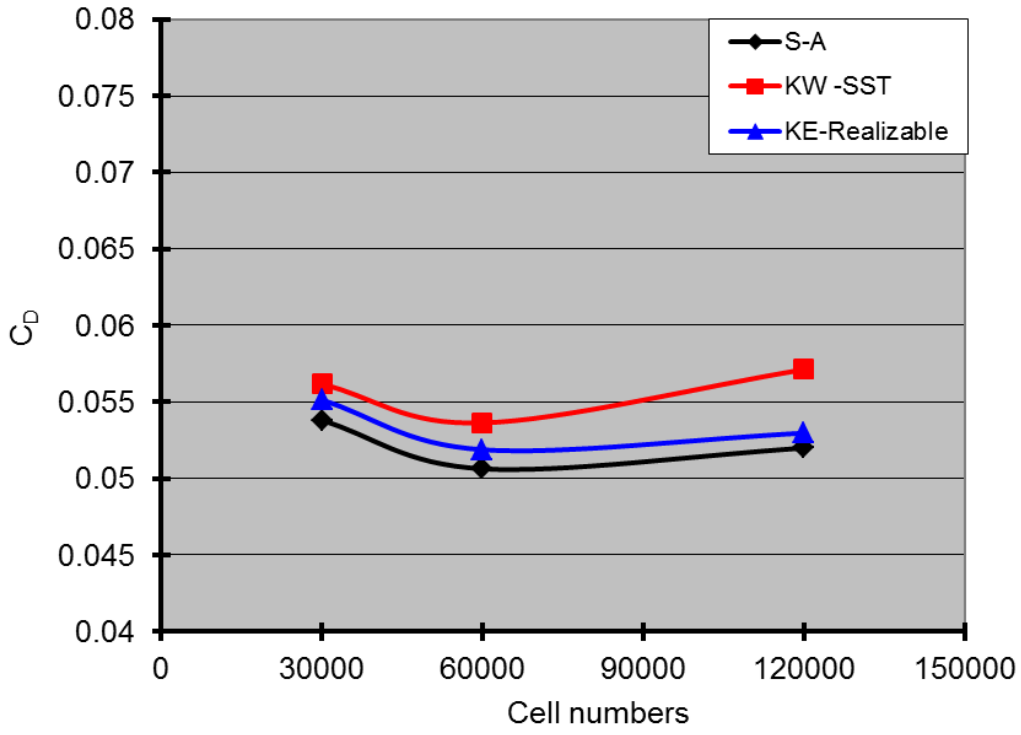

Figure 68 CD vs Cell numbers for different models

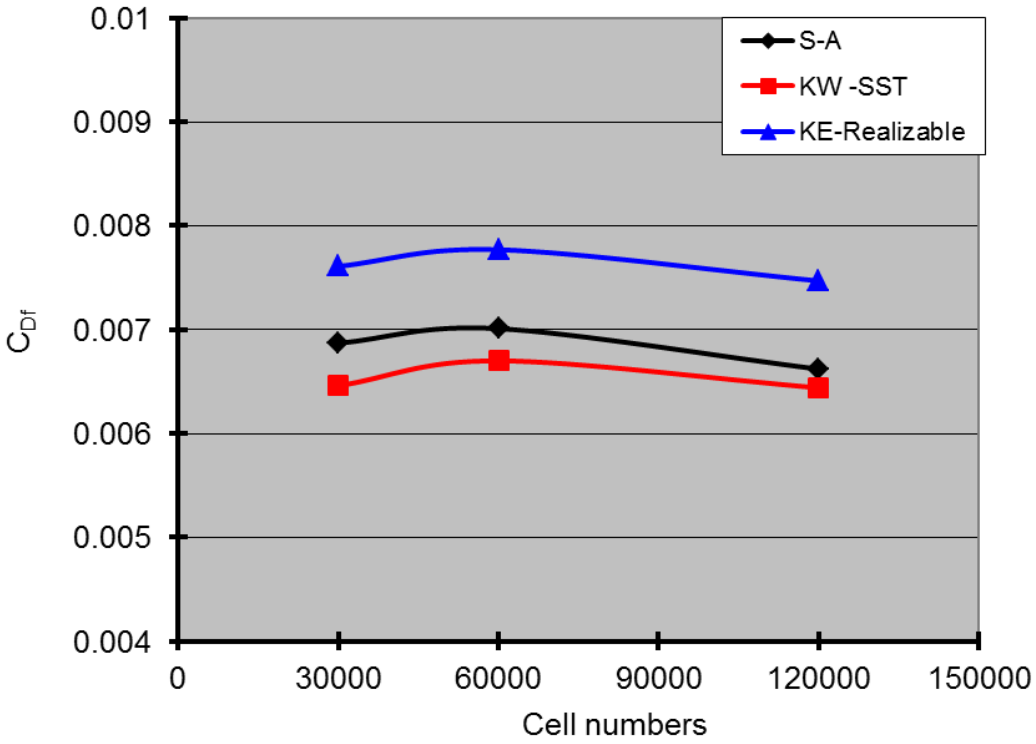

Figure 69 CDf vs Cell numbers for different models

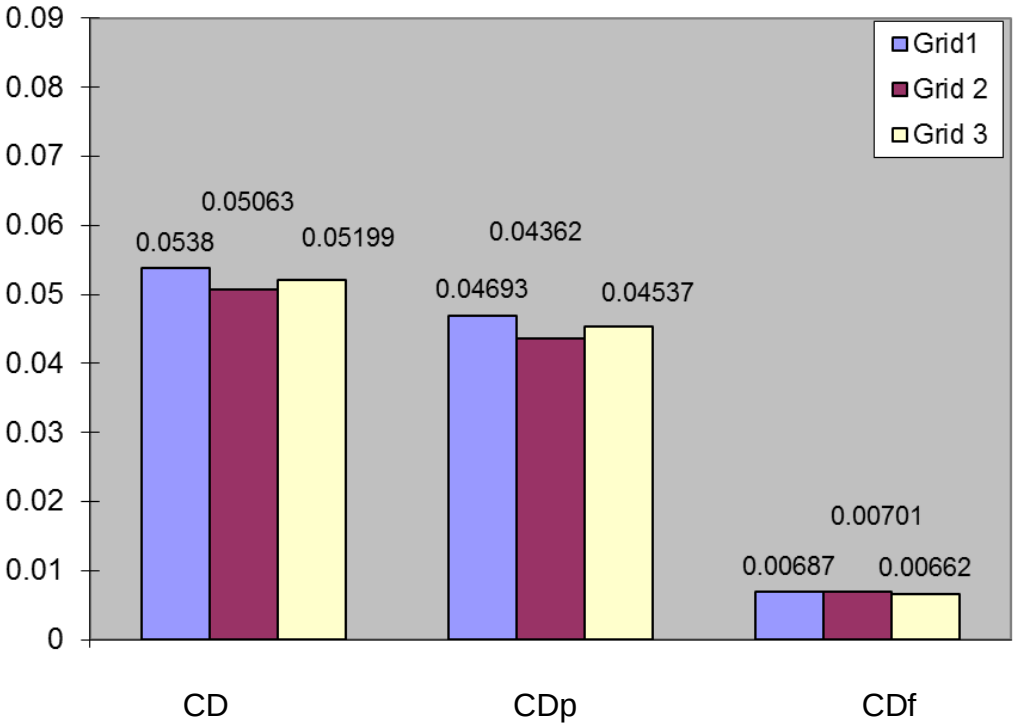

Figure 70 The CD, CDp and CDf for SA model results

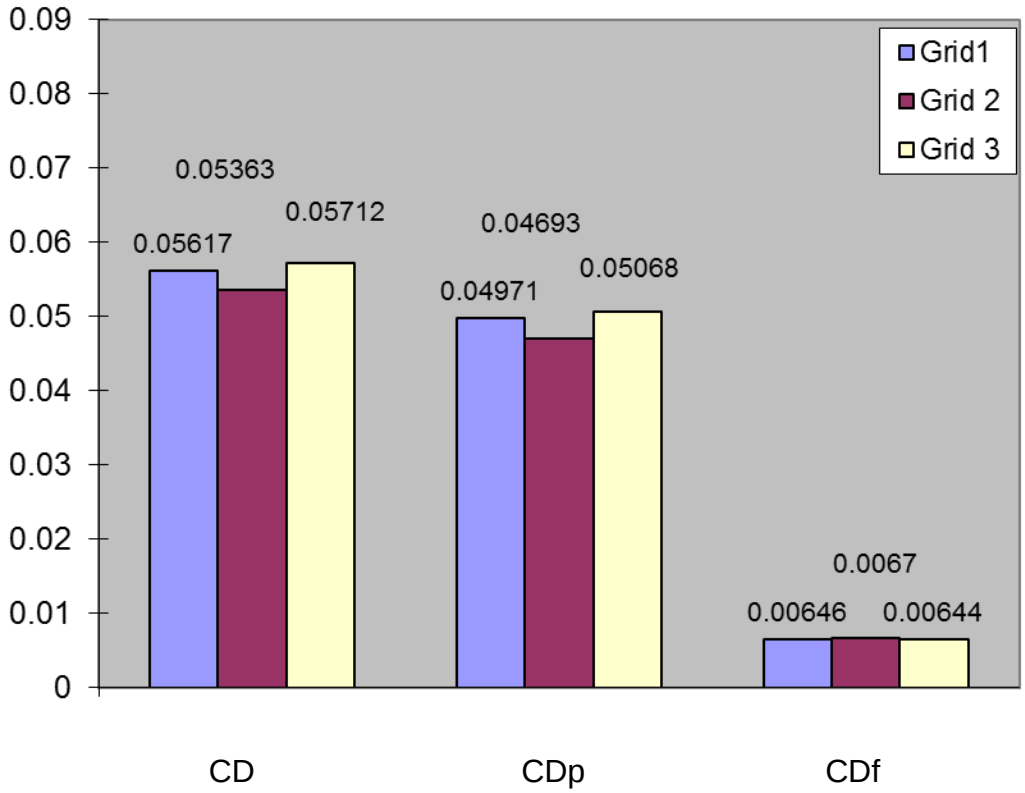

Figure 71 The CD, CDp and CDf for KW-SST model results

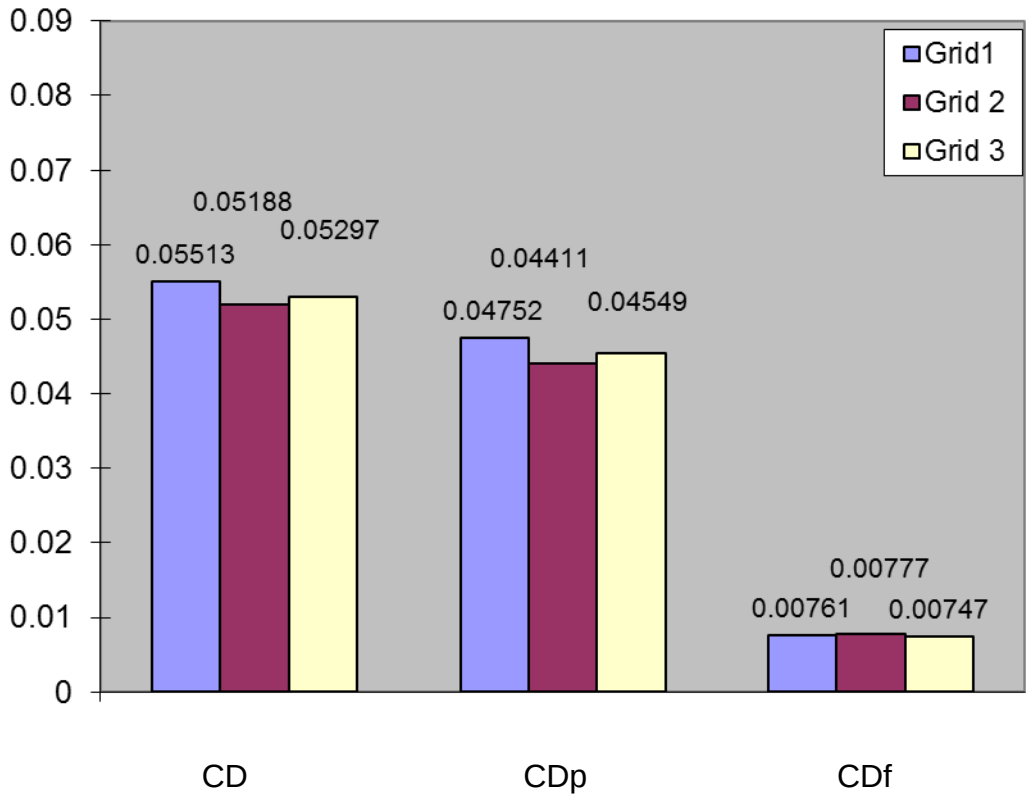

Figure 72 The CD, CDp and CDf for KE-Realizable model results

Generally speaking, G2 grids have the best results compared to experiments for CL and CD. On the other hand, the time cost increases from G1 to G3 which can be found in Table 5. It seems that G1 is a little too coarse and has the largest discrepancy compare to experiment data. G3 is most time consuming and discrepancy to experiment is still larger than G2. G2 has the best accuracy of CL and CD and has the medium time cost which can also be accepted by optimisation. Hence the conclusion can be made that G2 is the most favourable selection mesh for optimization.

2.5 Conclusions

From the above analysis, some conclusions can be abstracted:

1) All three RANS models which are SA, K-ω SST and K-ε Realizable can predict pressure and lift quite well with the accuracy of lower than 5%, which

may be relevant to the phenomenon that all three RANS models predict the same level of boundary layer thickness.

2) In general, drags are predicted by all turbulent models with accuracies of lower than 25% which are qualified for multi-objective optimization research for this case.

3) The modelling internal of boundary layer is different between turbulent models. K-ε Realizable model tends to predict the most intense velocity gradient normal to wall which result in the highest friction coefficient. K-ω SST model tends to over-predict the most serious velocity losses whereas SA model does the contrast. This can explain why SA model has the most accurate CD prediction and K-ω SST model has the biggest errors of CD prediction.

4) Three grids dependency are investigated and show that G2 grid has the best trade-off between the accuracy of results and time cost.

Chapter 3 Technical description of Multi-Objective Tabu Search Optimisation systems

3.1 Main process

An in-house Tabu search optimisation code is used to execute the optimisation. The CFD solvers including SA model, k-ε Realizable model and K-ω SST model are coupled with optimisation code by combining the scripts file of ICEM and FLUENT to the code.

Figure 73 shows the integration of the whole optimisation system which is comprised of shape parameterization, multi-objective algorithm and CFD tools. Coupled with ICEM and Fluent, a Tabu search multi-objective optimisation code (MOTS) create the new design vectors, which serve as the input for a new shape generator (FFD) to create new shape, and run the cycling of the optimisation.

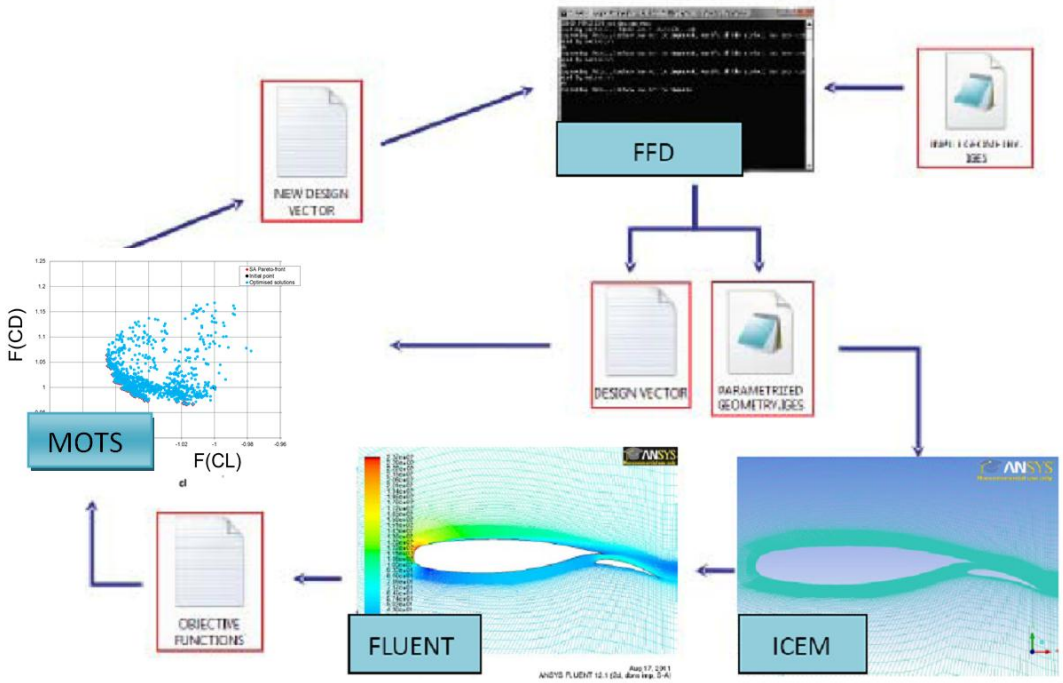

Figure 73 The optimisation process in the study

In general, the work flow and relationship between parameterisation tools, CFD tools and MOTS library are linked by mots_slave.cc and mots_master.cc, see Figure 74.

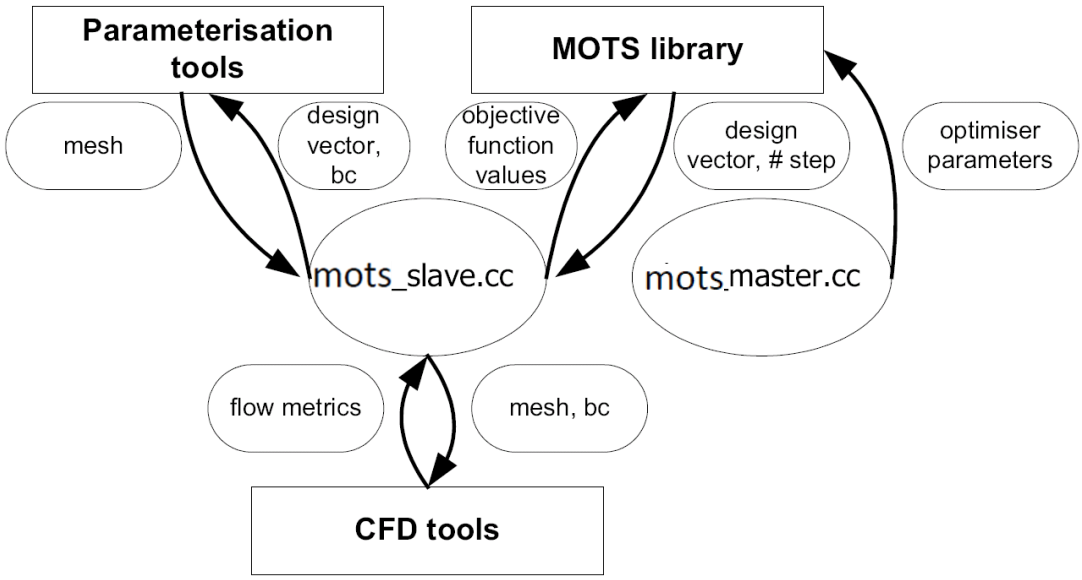

Figure 74 The functions of mots_slave.cc and mots_master.cc [33]

The first step is the parameterization of the datum geometry. The initial shape is converted to design vectors and then sent to mots_slave.cc. Geometry parameterization is realized by free form surface deformation method (FFD) in the system. FFD is a subset of the soft object animation algorithms used in computer graphics for deforming surfaces and solid models. The main advantage of FFD is its independence from the grid topology which makes it capable of deforming any type of surface or solid primitive and its non-intrusiveness (geometry is represented in terms of the movements of a number of control points from an initial position). FFD is also capable of generating radically new shapes, but its generality can also lead to large design spaces in applications. Highly specialized and efficient parameterization schemes are needed to reduce considerably the number of design variables. In this study the FFD uses eight points to control the generation of main element shape which can be shown in Figure 75. Among them the first two points and last two points

remain unchanged, as results, the leading edge shape, trailing edge thickness and the chord of the main element are kept the same as datum shape.

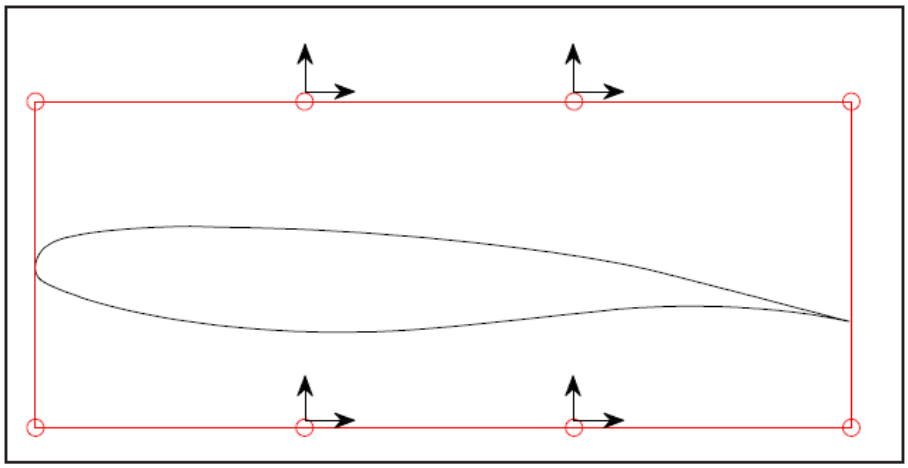

Figure 75 the location of the control points for the main element airfoil

After that, the geometry is sent to CFD tools for mesh generation and flow solution. CFD tools include grids generator ICEM and flow solver Fluent. ICEM and Fluent scripts are needed to ensure the automatic cycling of optimisation iterations. ICEM scripts control the generation of the mesh and fluent scripts control the calculation of CFD.

ICEM 12.1 is selected to create the mesh. It should be very careful to run the ICEM when record the scripts because the wrong identification of the number of nodes may easily happen, especially for the splitting of edges. One suggestion is to avoid the unnecessary operations as much as possible. In this study, the commercial N-S equations software Fluent V12.1SP1 is selected. Some journal files are necessary to put into the code to setup the solution method and apply the boundary condition automatically. Text user interface (TUI) versions of scripts are needed to create the jou files. Boundary conditions and all other solver set-ups should also be included in the jou files.

After the computations, the flow metrics are returned to mots_slave.cc and combined with objective functions are sent to an/the optimisation library to serve as the input for the design space exploration.

During the optimisation evolution stage, the mots_master.cc can search the optimizer parameters and send them back to the optimisation library; after that these parameters will be translated as new design vectors and step sizes to mots_slave.cc, and then sequentially sent to parameterization tools for the generation of new design vectors and new mesh.

3.2 The constraints handling and objective functions set-up

Since the objective of the study is concerned with how the CFD turbulent models impact optimisation, rather than the optimisation of airfoil shape itself, the flap of NLR7301 2-element airfoil is fixed and just the main airfoil is modified. As a result there is no need to change the flap shape. For the main element, as mentioned above, the leading edge shape, the trailing edge thickness and the chord of the main element remain unchanged. This strategy simplifies the optimisation problem without reducing the quality of the main objective.

Essentially every aerodynamic design is at least a dual objective optimisation. The common understanding for improving aerodynamic performance is to increase lift while reducing drag. It is the benchmark aerodynamic design problem for high-lift devices. The objective function of lift and drag are presented as following:

$$F(CL) = -\frac{CL}{CL_{datum}}$$

Equation 3-1

$$F(CD) = \frac{CD}{CD_{datum}}$$

Equation 3-2

The normalized functions F(CL) and F(CD) represents the lift and drag characters of optimized shapes and can be optimized by minimizing the value.

3.3 Process parallelization

The highly time-consuming nature of MOO makes the utilization of parallelization necessary. Thus the system should have the capability to be parallelized by computation resources. As mentioned in Chapter 1.2, the parallelization methods include Function decomposition, Domain decomposition and Multi-thread. In this case, the first two strategies have been applied in the optimisation to enable realization of multi-level parallelization.

3.4 The ASTRAL High performance computing cluster

The 856 processor HP XC Cluster, ASTRAL, is utilized to perform the optimisation. This high performance cluster sited at Cranfield University is an industrial-grade, production-ready system with a cluster system architecture for high-performance technical computing. Node structure is applied to the cluster and each grid node is a HP DL140 G3 server with two Intel 5160 Xeon 3 Ghz, dual-core processors. Each node has 8GB of shared memory between the 4-cores. Each dual-core CPU has a 4MB cache shared between the cores [29]. The system employs the state-of-the-art, DDR Infiniband, high-speed interconnection and uses the HP-MPI (Message Passing Interface) version of MPI due to its extremely good reputation for stability.

HP XC Clusters provide a comprehensive, supported solution for serial and parallel applications, complemented by a robust application development environment and extensive ISV application portfolio. Applications from the leading developers of software for CAE, EDA, Life and Material Sciences, and other disciplines are available on XC Clusters. [71]

Using ASTRAL, the job should be submitted to the system in batch model. The setup of the computation can be defined by the necessary script file. In this way the MOTS parallelization can be made compatible with ASTRAL architecture.

Chapter 4 Results and Analysis

In this chapter the results of optimisations of different turbulent models are presented and analysed and a comparison of results made.

4.1 Optimisation results

Prior to an analysis of results, it is first necessary to detail the amount of optimisations achieved and time consumed, as shown in Table 8. It seems that more than 800 CFD evolutions are needed to reach the complete Pareto-fronts. K-ε Realizable model is the most effective model in terms of wall clock time. K-ω SST model is the slowest model but very close to SA model.

Table 8 The amounts and time cost of optimisations

Models	Optimisation evolutions	CFD evolutions	Time cost
SA	92	1100	293hrs
K-ε Realizable	73	800	204hrs
K-ω SST	87	1000	300hrs

Another character of the optimisation is the number of infeasible solutions, which for optimisation is expected to be fewer. In general, the reasons to trigger collapse solutions are included below:

a) Violations of constraints;

b) Collapse of building mesh;

c) Divergence of the flow solutions.

The numbers of infeasible solutions in the study are particularly low: during the whole optimisation, there are less than 2 collapses for all three turbulent cases.

Owing to the less constrained environment, there is no infeasible solution caused by violations of constraints. The collapses of building mesh are also limited by applying an intelligent grid generating strategy which can control the grids to move correspondingly with the shape. Emphases have also been put on the quality of grids, so the numbers of divergence solutions are also limited.

Figure 76 shows the tabu-plots and optima-fronts of SA model. It can be found that optimisation solutions of F(CL) range from -0.9777 which is the most un-optimized to -1.0651 which is the most optimized. The optimisation solutions of CD are range from 1.1674, the most un-optimized and 0.9665, the most optimized. Pareto-fronts are obviously reached and shown with red colour in the figure. The best solution for CL is -1.0651 which means the increment of lift is 6.51%. The best solution for CD is 0.9665 which means the decreasing of drag coefficient is 3.35%.

Figure 77 and Figure 78 show the results of K-ε Realizable model and K-ω SST model. The range of optimisation solutions are shown in Table 9.

Table 9 The range of optimisation solutions of three turbulent models

Models	Min F(CL)	Max F(CL)	Min F(CD)	Max F(CD)
SA	-0.9777	-1.0651	0.9665	1.1674
K-ε Realizable	-0.9839	-1.0693	0.9715	1.2137
K-ω SST	-0.9718	-1.0668	0.9347	1.2248

Figure 79 shows the comparison of the Pareto-fronts of three models. From the perspective of optimisation quality of “paper value”, it can be found K-ε Realizable model capture the maximum CL and K-ω SST model is the best to optimize drag. SA model has the similar pattern of Pareto-fronts with K-ε Realizable model at the range where F(CL) is large than -1.06 but can be

dominated by K-ε Realizable fronts at the range where F(CL) is large than -1.06.

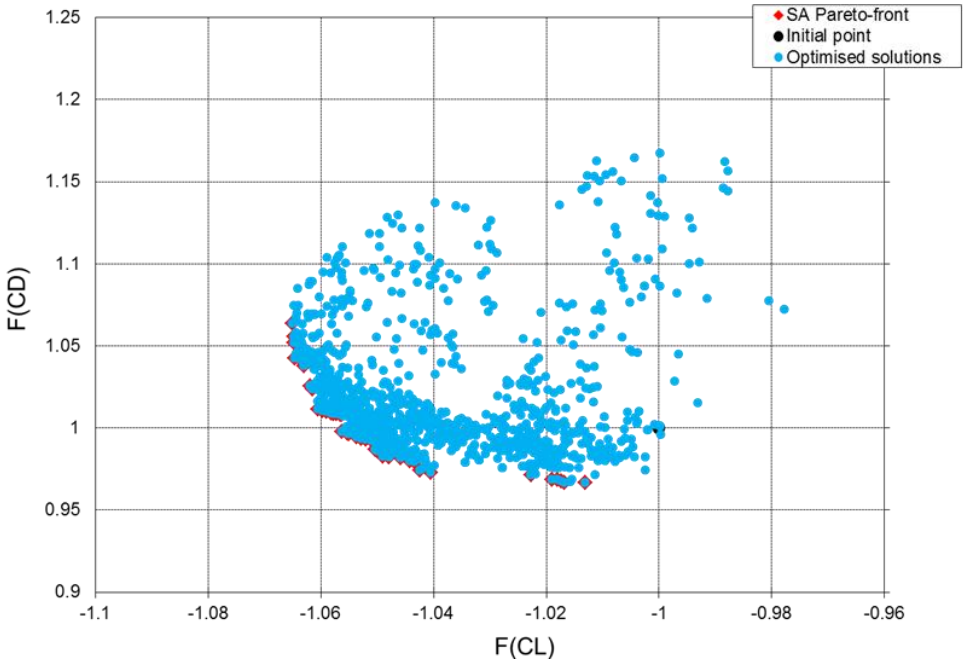

Figure 76 The tabu-plots and optima-fronts of SA model

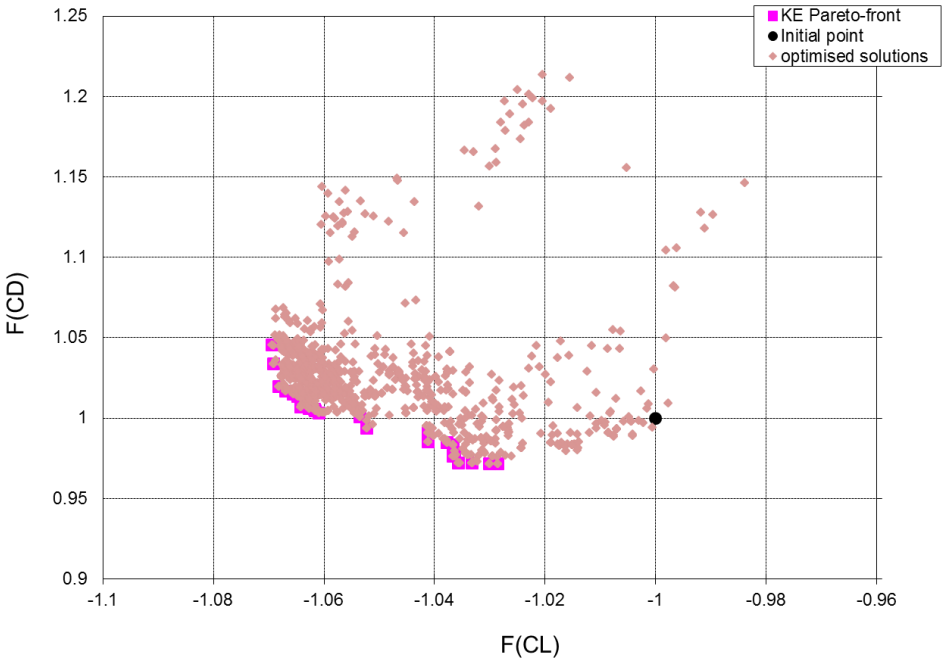

Figure 77 The tabu-plots and optima-fronts of KE model

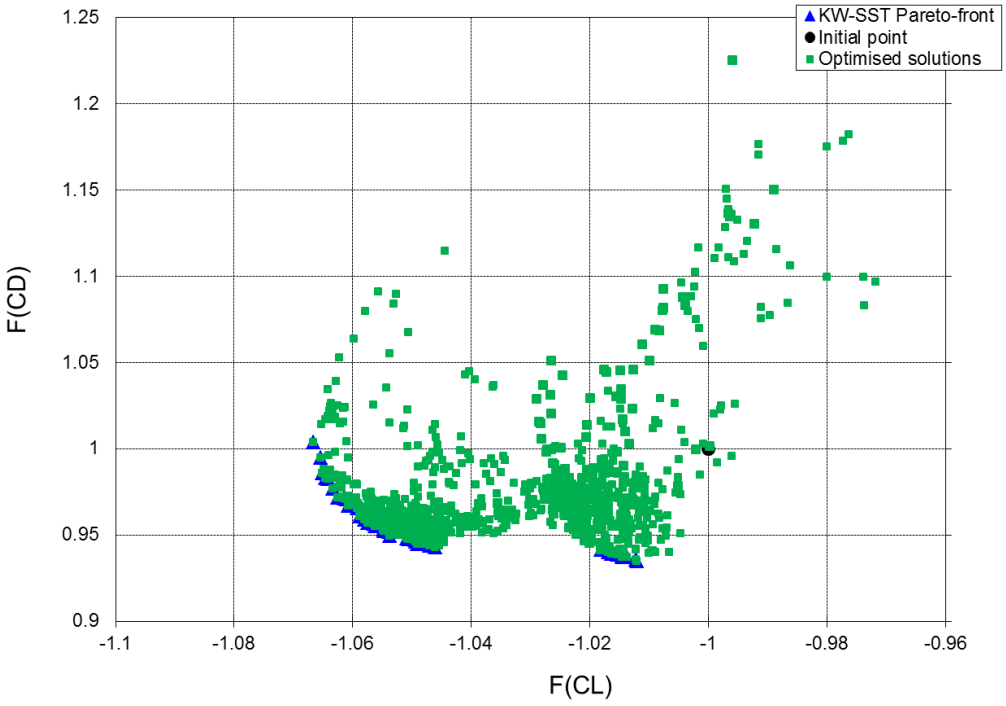

Figure 78 The tabu-plots and optima-fronts of K-ω SST model

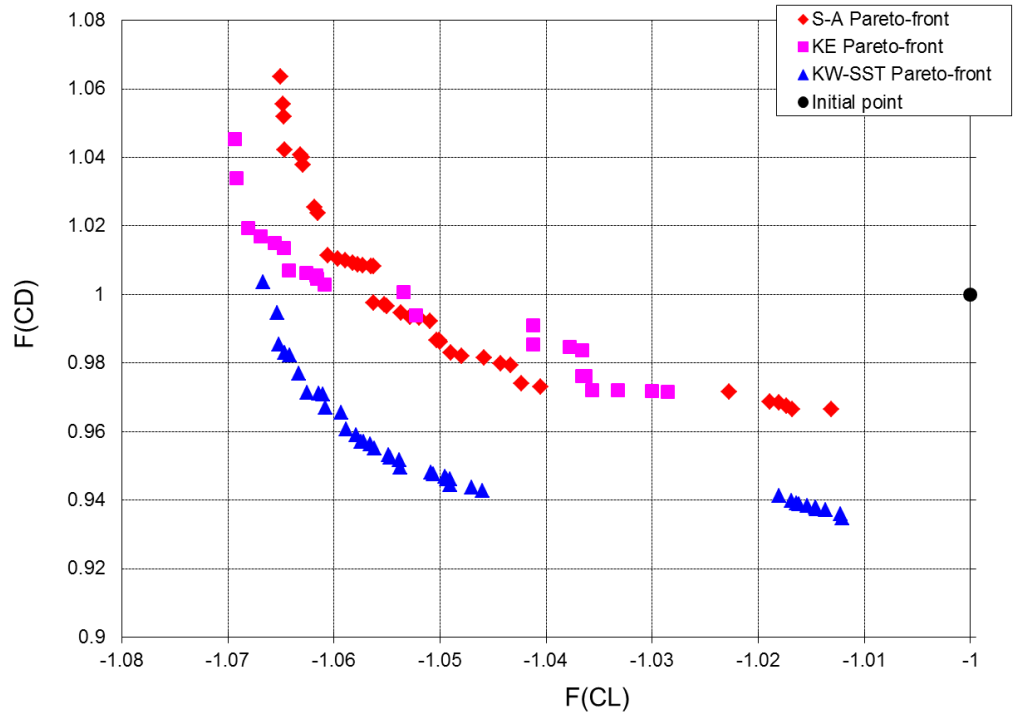

Figure 79 The comparison of Pareto-fronts of three turbulent models

4.2 The criteria of optimality of lift and drag

In this study, the performances of optimisation are measured by lift and drag which are the most important aerodynamic parameters in airfoil design. Considering that it is a high lift configuration for take-off condition, some typical cases are defined below to serve as the criteria to estimate the optimisation quality:

Case A: Considering the limitation of thrust, drag should be limited to fulfil the requirements of thrust. In this study F(CD) should be defined as not larger than 1 which means the drag of optimised shape can't beyond the drag of datum shape, then try to optimize lift to improve the performance.

Case B: The thrust of the engine is high enough to have a rich margin to overcome the drag and drag would not be limited; the focus can then be on the optimisation of lift.

Case C: The lift of the aircraft is good enough to fulfil requirements; the motivation of optimisation should be focused on drag. In this case, the minimum drag is the only target.

Case D: In this case both lift and drag can easily fulfil the requirements; the objective is therefore to try to optimize the performance of aircraft by increasing the L/D. In this case, a highest L/D value is the object to be optimised.

According to the criteria discussed above, it is possible to pick up the optimality of the optimisations from the Pareto-fronts which are shown in Figure 80. In this Fig, point A which is corresponding to case A represents a limited maximum CL; point B which is corresponding to case B represents an unlimited maximum CL; point C which is corresponding to case C represents the lowest drag. Point D which is corresponding to case D represents the best L/D. The normalised values of CL and CD for these points are listed in **Table 10**.

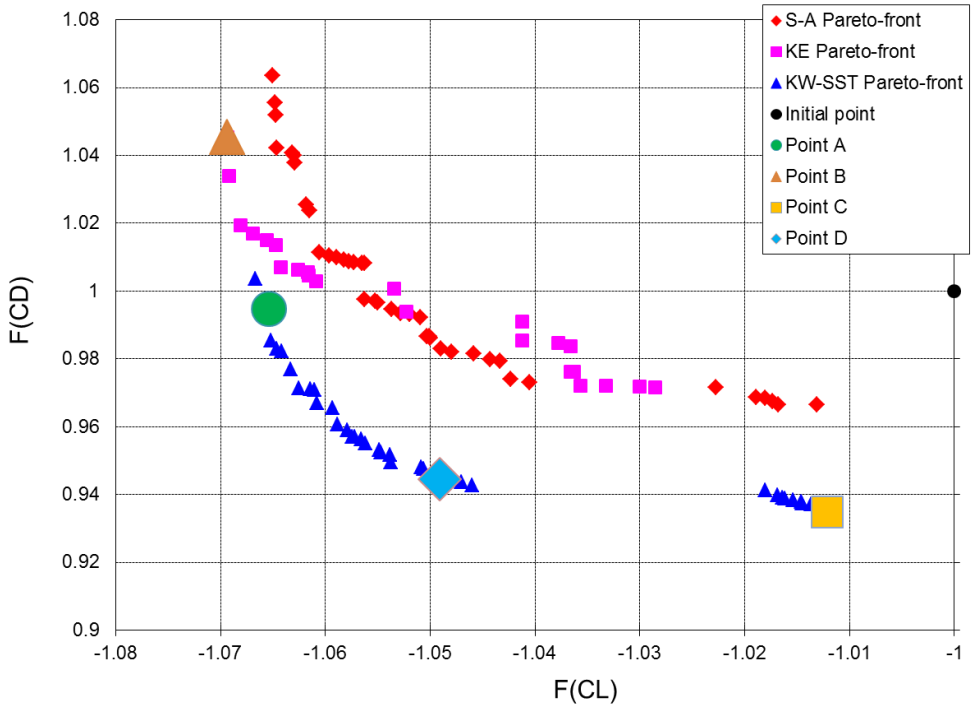

Figure 80 The selection of optimality points

Table 10 The optimality of different conditions

No.	F(CL)	F (CD)	Remarks
Point A	-1.0654	0.9947	Max CL limited CD
Point B	-1.0693	1.0453	Max CL
Point C	-1.0121	0.9347	Minimum CD
Point D	-1.0490	0.9445	Highest L/D

At point A, the F(CD) is limited to lower than 1 and in fact it decreases about 0.53% compared to datum configuration, following this a optimized CL of about 6.54% greater than datum shape has been reached. At point B, the highest CL

in the whole optimisation of about 6.93% greater than the datum data has been reached; however, the drag increases about 4.53% simultaneously. At point C, the lowest drag in the whole optimisation which is 6.53% lower than datum drag has been reached, in this case, CL is also about 1.21% greater than the datum data. At point D, both CL and CD are optimized and the highest L/D has been reached which is about 11% greater than the datum data.

The shapes of these optimized points are emulated and depicted in Figure 81. It can be found that the shape of “max lift” has the biggest camber, “best L/D” and “max lift limited drag” have the similar shape with “max lift”, and they can optimise the lift and drag simultaneously. High lift may come from the big camber and flow can be maintain attached as can be found in Figure 82 by the effects of “drop nose”, referred to in Figure 81. Low drag may come from the decreasing of thickness. The shape of minimum drag is the one most close to the datum shape. The decrease of drag seems to come from the reduction of thickness.

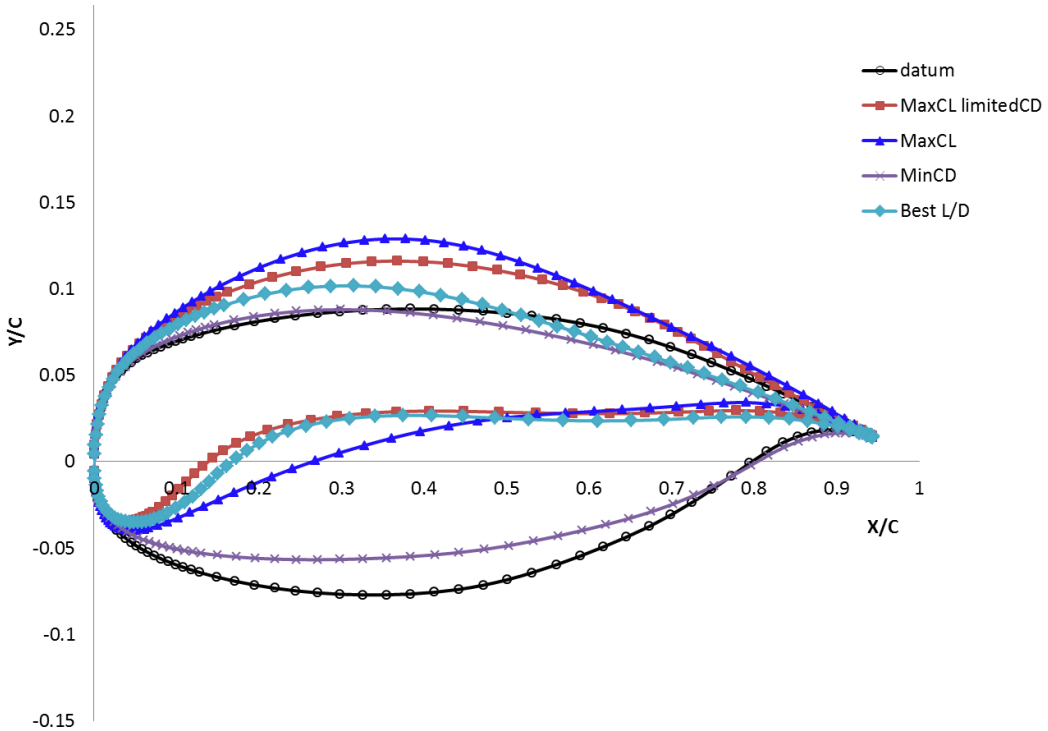

Figure 81 the comparison of optimised shape and datum shape

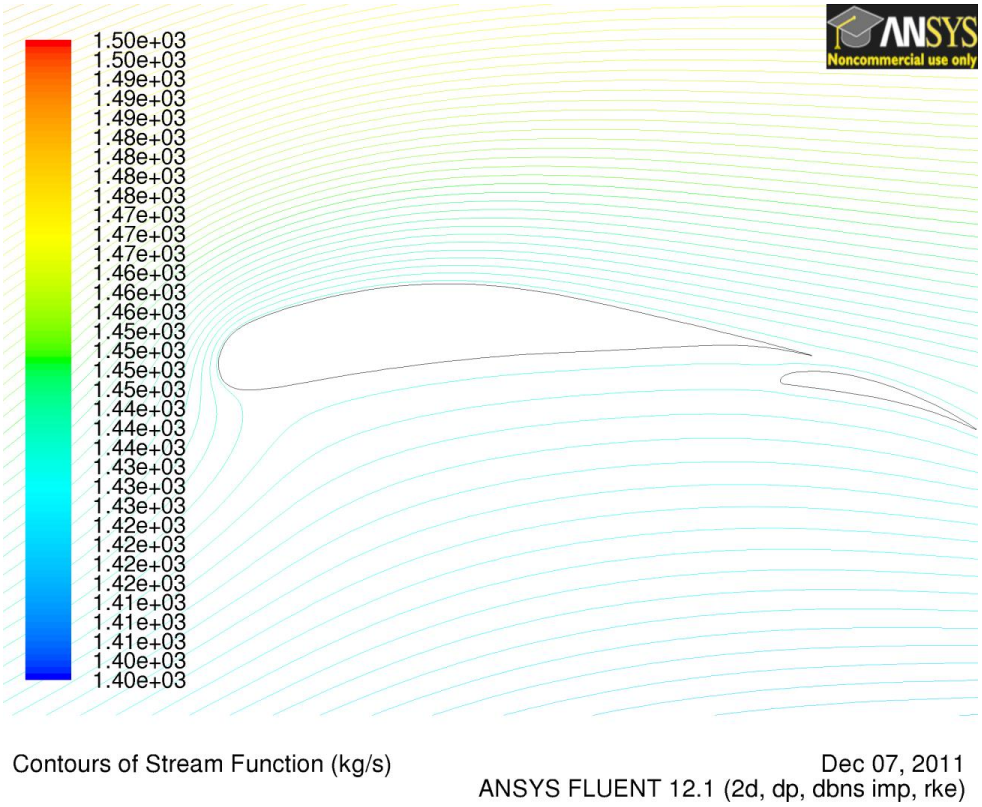

Figure 82 the streamline contours of the "MaxCL-KE" shape

4.3 The verification of the optimality and analysis

Until now the optimality has been discussed according to the "paper value"; it is necessary to verify the optimality by other methodology. In this study, considering the optimised cases are measured by the results of an individual turbulent model, so typical cases discussed above might be verified by the simulations of two other turbulent models. Based on this methodology, all the cases of optimality including points A, B, C and D are solved by all three turbulent models. Table 11 presents the values of CL and CD of optimality cases by different turbulent models. Based on these results, the optimised performance of CL and CD are recalculated with the normalised format of F(CL) and F(CD). The differences of these recalculated F(CL) and F(CD) and datum F(CL) and F(CD) are presented in Table 12.

Table 11 CL and CD values of optimality cases by different turbulent models

Models	Values	A	B	C	D
SA	CL	3.482	3.509	3.299	3.425
	CD	0.05179	0.05244	0.04915	0.04919
K-ε Realizable	CL	3.445	3.472	3.266	3.393
	CD	0.05360	0.05404	0.05115	0.05108
K-ω SST	CL	3.425	3.447	3.24	3.376
	CD	0.05382	0.05472	0.05138	0.05068

Table 12 The difference of comments on the optimality case

Models	Values	A	B	C	D
SA	F(CL)	-1.059	-1.068	-1.004	-1.042
	F(CD)	1.023	1.036	0.971	0.972
	dF(CL)	-0.56%	0.11%	-0.41%	-0.77%
	dF(CD)	1.93%	1.51%	1.33%	2.81%
K-E Realizable	F(CL)	-1.058	-1.066	-1.003	-1.042
	F(CD)	1.033	1.042	0.986	0.985
	dF(CL)	-0.68%	0.00%	-0.47%	-0.76%
	dF(CD)	2.95%	0.00%	2.91%	4.19%
K-W SST	F(CL)	-1.065	-1.072	-1.008	-1.050
	F(CD)	1.004	1.020	0.958	0.945
	dF(CL)	0.00%	0.55%	0.00%	0.00%
	dF(CD)	0.00%	-2.05%	0.00%	0.00%

Two interesting points can be found based on the results above. Firstly the effects of optimisation have been confirmed by the results of all turbulent models. Secondly it can be found that different turbulent models have different comments on the same optimality shape which introduces the argument about what is the real optimized performance and which model is the most accurate.

In terms of CL, three turbulent models have similar results. The differences between models are lower than 1%. However, it can also be found that K-ε Realizable model has the strictest results on the efficiency of optimisation though it is very slight.

In terms of CD, the comments of different models are much more varied. In general, K-ω SST model tends to have more positive prediction while K-ε Realizable model has the most conservative comments for the same optimized configuration. SA model is somewhat between. For example, for the CD of case A, K-ω SST model thinks that 4.07% optimisation has been reached while KE model thinks the optimisation is only 0.35%.

4.4 Comparison of the optimised shapes and optimisation effectiveness

In parallel, to clarify the difference of the optimisation capacity behaviours between turbulent models, shapes are abstracted for all turbulent models to compare with each other according to three tasks as listed below:

- Minimal CD
- Maximum CL
- Best L/D

Figure 83-Figure 85 show the comparison of “minimum CD” shapes, “maximum CL” shapes and “best L/D” shapes respectively. For “minimum CD” shapes, different models capture varied shapes which have not too much difference. K-ω SST model captures the shape with minimum thickness and may have the lowest drag. For “maximum CL” shapes, all models capture the similar upper

surfaces and much different lower surfaces, the difference between models are greater than that for “minimum CD” shapes. SA model captures the shape with lowest camber which may reduce CL and maximum thickness which may increase CL. K-ε Realizable model captures the shape with similar camber to K-ω SST model but have greater thickness. For “best L/D” shapes, significant difference can be observed between shapes. The differences of shapes are obviously the greatest and it might come from the reason that both CL and CD are targeted.

In general, different models capture different optimised shapes. For “MinCD” shapes where the optimised shape is not far from the datum shape, different models capture the similar shapes. The further the optimised shapes from datum shape, the greater the differences will be between different models. This can be observed from “Max CL” and “Best L/D” shapes.

Obviously, the comparisons performed above introduce once again the uncertainty of the optimisation which can be described as different turbulent models predict different optimised shapes for the same task.

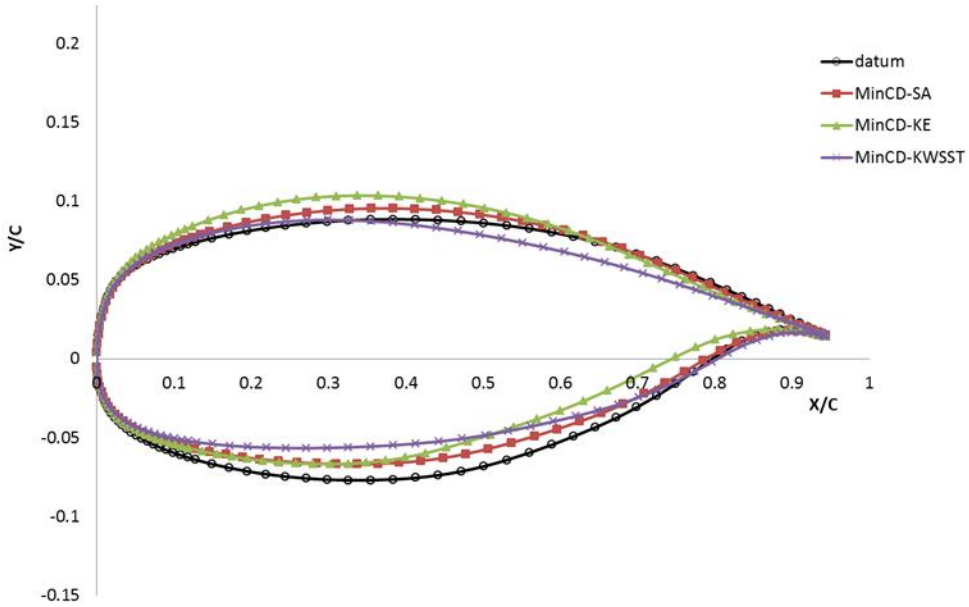

Figure 83 Comparison of “minimum CD” shapes between turbulent models

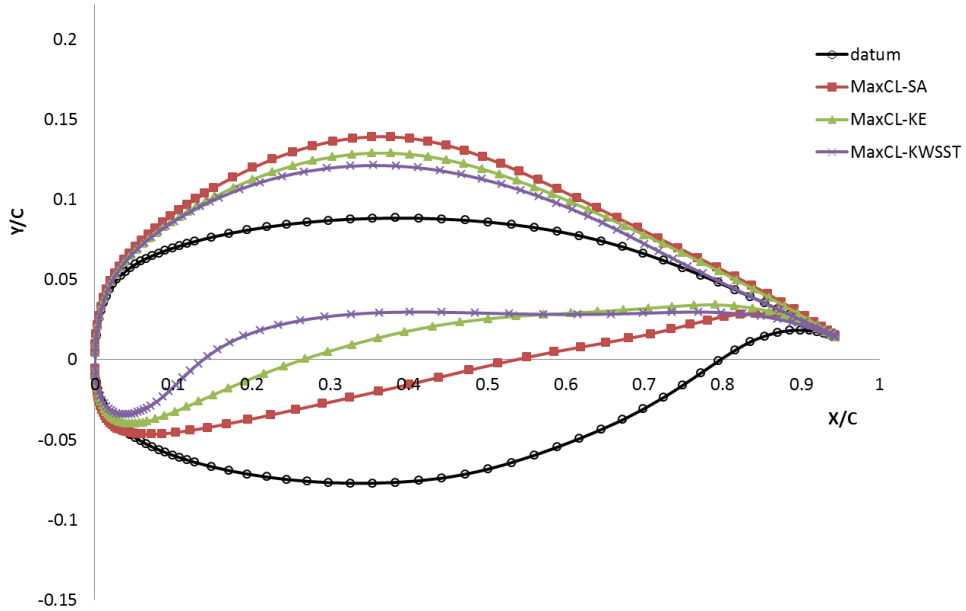

Figure 84 Comparison of "maximum CL" shapes between turbulent models

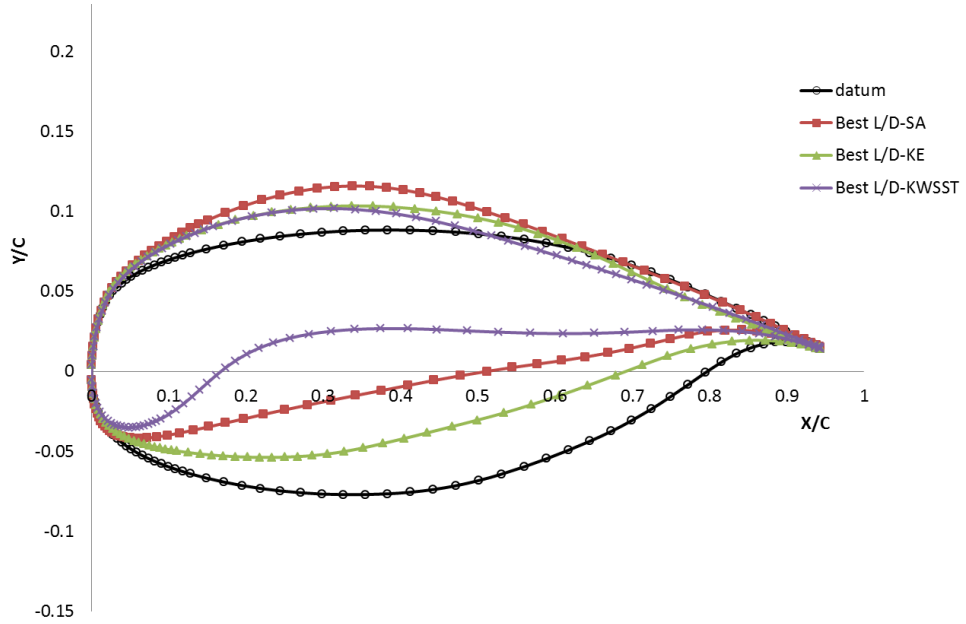

Figure 85 Comparison of "best L/D" shapes between turbulent models

Referring to optimisation quality, the "paper values" of the optimised shapes are presented in Table 13. From these "paper values" it can be found that K-ω SST

model captures the best shape for “MinCD” and “Best L/D”; K-ε Realizable model captures the best shape for “Max CL”.

Table 13 “Paper values” of optimised shapes

Shapes	F(CL)	F(CD)
MinCD-SA	-1.0131	0.9665
MinCD-KE	-1.0285	0.9715
MinCD-KWSST	-1.0121	0.9347
MaxCL-SA	-1.0651	1.0635
MaxCL-KE	-1.0693	1.0453
MaxCL-KWSST	-1.0667	1.0036
Best L/D-SA	-1.0489	0.9829
Best L/D-KE	-1.0357	0.9721
Best L/D-KWSST	-1.0490	0.9445

To verify the reliability of the “paper values” and compare the optimisation capacity between turbulent models, all optimised shapes are calculated by SA, K-ε Realizable and K-ω SST models. The results are compared with each other to judge the question “which model capture the most optimised shapes” and are shown in Table 14-Table 16.

Table 14 The comparison of CL&CD of optimised shapes of “Min CD” by different turbulent models

Models	MinCD-SA		MinCD-KE		MinCD-KWSST	
	CL	CD	CL	CD	CL	CD
SA	3.321	0.04966	3.347	0.05078	3.299	0.04915
K-E Realizable	3.286	0.05152	3.31	0.05278	3.266	0.05115
K-W SST	3.259	0.05202	3.284	0.05318	3.24	0.05138

Table 15 The comparison of CL&CD of optimised shapes of "Max CL" by different turbulent models

Models	MaxCL-SA		MaxCL-KE		MaxCL-KWSST	
	CL	CD	CL	CD	CL	CD
SA	3.5	0.05399	3.509	0.05244	3.487	0.05226
K-E Realizable	3.463	0.0557	3.472	0.05404	3.45	0.05401
K-W SST	3.422	0.05755	3.447	0.05472	3.429	0.05435

Table 16 The comparison of CL&CD of optimised shapes of "Best L/D" by different turbulent models

Models	Best L/D-SA		Best L/D-KE		Best L/D-KWSST	
	CL	CD	CL	CD	CL	CD
SA	3.446	0.04993	3.366	0.05106	3.425	0.04919
K-E Realizable	3.412	0.05172	3.329	0.05312	3.393	0.05108
K-W SST	3.392	0.0517	3.304	0.05347	3.376	0.05068

For "MinCD" shapes and "Best L/D" shapes, the verification results show that K-ω SST model captures the best shape, SA model captures the second and K-ε Realizable model captures the last. For "Max CL" shapes, the verification results show that K-ε Realizable model captures the best shape, argument occurs between SA model and K-ω SST model that they declare they capture the better shapes themselves between two. In general verification results agree with the optimality sequence of "paper values" quite well and confirm the reliability of the optimisation system.

Based on the conclusion above, K-ω SST model might be seen as the best turbulent model to capture the minimal drag and Best L/D in this study. Considering the shapes captured by K-ω SST model have the lowest thickness, they seem reasonable in aerodynamic view but they may cause the problem of structure design and system placement which must be considered in practical.

4.5 Discussions on the uncertainty of optimisation

Although the results shown above state that the “paper values” of optimisation are reasonable and confirm the reliability of the optimisation system, the uncertainties for the optimisation should not be neglected. Considering the high requirements for accurate prediction of aircraft performances, optimisation system should not only optimise but also optimise accurately, the uncertainties of optimisation should be highlighted and knowledge on this area should be built and enhanced.

The results in this study reveal that the uncertainties of CFD based optimisation system clearly exit. The uncertainties are arisen from two levels:

a) Different turbulent models observes the optimisation performance differently based on the same optimised shape;
b) Different turbulent models tend to capture different optimised shapes.

Considering that the same computational hardware and the same grids are used, the main reason causing the differences in this study should be from turbulent models. In general the real value of CL and CD can be comprised of the calculation value and its error which can be presented as following:

$$CL_{Real} = CL_{KE} + \varepsilon_{KE} = CL_{SA} + \varepsilon_{SA} = CL_{KWSST} + \varepsilon_{KWSST}$$

Equation 4-1

$$CD_{Real} = CD_{KE} + \varepsilon_{KE} = CD_{SA} + \varepsilon_{SA} = CD_{KWSST} + \varepsilon_{KWSST}$$

Equation 4-2

The errors for different turbulent models are varied. It is the difference of errors that make the “paper values” of the optimisation efficiency different. To optimise the shape accurately, it is necessary to take the error of the turbulent models into account.

Ideally if there are validation data from experiments for optimized configurations, it will be more convincing to analyse the uncertainty of the turbulent models on optimisation. Unfortunately for most optimised configurations there is no such validated data available.

One simple method to pick up the most accurate model is to select the most accurate model in CFD validations. It is reasonable for this simple methodology to be applied because the most accurate model has the lowest uncertainty in CFD validation, hence it may introduce the lowest optimisation uncertainty. In this study, SA model has the best accuracy on drag, so it might be the most probable accurate turbulent model for this Multi-Objective Tabu Search optimisation system.

This simple methodology is supported by Figure 86 which shows the CL and CD of the four optimised cases A, B, C and D mentioned in Figure 80. The systematic move of all turbulent models results reveals the consistent optimisation tendency which might state that the errors for optimised shapes are more or less the same level as datum shape. With this assumption SA model would have the best accuracy on optimised shapes; hence it may state the optimisation most accurately.

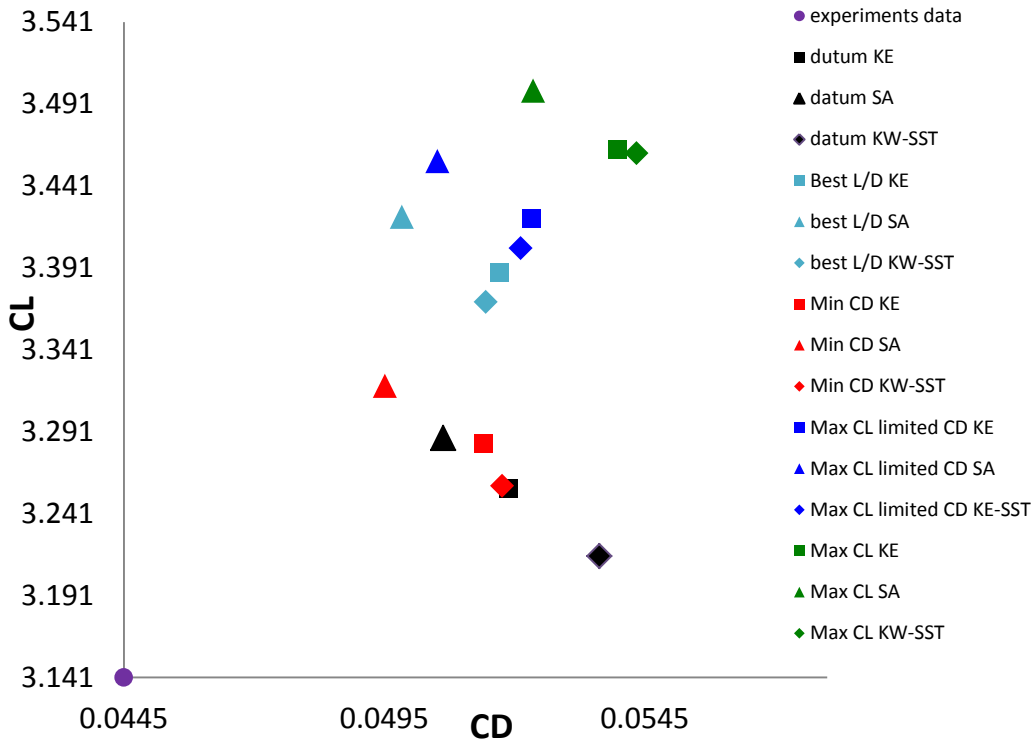

Figure 86 the distributions of optimality results

Chapter 5 Conclusions and Future works

5.1 Conclusions

In this study, three turbulent models which include SA model, K-ε Realizable model and K-ω SST model are selected to couple with a Multi-Objective Tabu Search system. Following analysis of the optimisation results for NLR7301 2-element high lift configuration, the behaviour of the three turbulent models in the optimisation environment is examined and interesting points highlighted.

Firstly the CFD validations of turbulent models were achieved. In general good agreements have been reached between CFD simulations of three turbulent models and experiment data. The flows are reasonable, Cp are predicted quite well and Cf are broadly good. In terms of lift and drag, CL are predicted within accuracies of below 5% and CD are predicted within accuracies of lower than 20%. However, differences can still be distinguished between turbulent models. In terms of drag prediction SA model has the best results and K-ω SST model has the worst results. In terms of CL prediction K-ω SST model has the best solution and SA model has the most over-predicted results. K-ε Realizable model is mid-way between SA models and K-ω SST models. From analysing the velocity profile internal of boundary layer, the difference of velocity losses predicted by different turbulent models may be the main reason for different drag.

Grids dependency has also been investigated in this study to ensure an efficiency CFD module to be linked with the optimisation system. Three grids which include coarse mesh, medium mesh and fine mesh have been generated with the same block strategy. By analysing CFD simulations, medium mesh is selected to be involved in the optimisation system which has achieved a good trade-off between mesh numbers and solution quality.

By producing the ICEM scripts file for grid generation and FLUENT journal file for flow solutions and combining them with an existed in-house Multi-Objective Tabu Search optimisation code, a complete MOTS optimisation system has been formed for NLR7301 two-dimensional high lift airfoil.

The optimisation results show something classical and new. Firstly, the consistent effects of optimisation can be observed by all turbulent models, all models can produce optimised geometries with optimised performance. These results confirm once again that optimisations effects can be clearly reached by utilizing CFD based optimisation. Secondly and more importantly, the results show that uncertainties are clearly present for the CFD based optimisation system. The uncertainty can be found in two levels. The first is different turbulent models observe the optimisation efficiency of the same optimised shape with significant differences; the second is that different turbulent models capture the different optimised shapes within the same task. These findings and the requirements of aircraft design calls for the necessity to estimate the uncertainties of optimisation accurately. For the first level uncertainty, one simple methodology has been applied to pick up SA as the best turbulent models for the accurate comments of optimisation extent. For the second level uncertainty, the verification results show that K-ω SST model capture the best aerodynamic shapes for “MinCD” and “Best L/D”, which reveals that K-ω SST might be the proper turbulence model to capture the most efficient aerodynamic shapes.

5.2 Future works

The investigation in this study has introduced the argument of the uncertainty of CFD based optimisation for a high lift airfoil. This can be served as a beginning and further works can be undertaken on how to estimate the uncertainty in a more convincing way. Systematic research is recommended as follows:

a) Return to a simper configuration such as a single element airfoil, try to use different RANS models to optimise them, and then undertake the

experiment validations for the optimised shapes. Following this the estimation of the uncertainty can be reasonably achieved for different turbulent models. The experiment of single airfoil will keep the cost of this research low and acceptable.

b) Consider theoretical methods in parallel, to estimate the uncertainty of optimisation.
c) After the completion of the optimisation uncertainty of single airfoil, work towards solutions for the similar problem for multi-element airfoil and wing.
d) Examine the effects of grids density on the uncertainty of optimisation.
e) Investigate the effects of uncertainty between RANS model and other turbulent models such as LES.

Excluding the suggestions about the uncertainty of optimisation, some applications of this intelligent CFD based optimisation can be achieved as follows:

f) The optimisation of the shapes will result in the changing of transition position, but in this study the changing of transition position has not been considered which may introduce uncertainty to the results. In the future this point should be considered and methodology of predicting the transition position should be also involved in the whole optimisation system.

g) In this study a 2-D case is selected owing to its simplicity and availability of experiment data. But as the tendency of optimisation now is obviously directed to solving real word practical problems, so it is more beneficial to investigate the possibility of applying this optimisation system to 3-D airfoil design if the accessibility of high performance hardware are available. It is recommended the trail can be started from 3-D single element wings and then turn to 3-D high lift wings.

References

[1] Zachariadis, Z. I.; High Resolution and High Order Methods for RANS Modeling and Aerodynamic Optimisation; Ph.D. Dissertation. University of Cranfield; 2008

[2] Van Dam, C.P.; The aerodynamic design of multi-element high-lift systems for transport airplanes; Progress in Aerospace Sciences 38; 2002

[3] Flaig A.; Hilbig R.; High-Lift Design for Large Civil Aircraft, AGARD-CP-515, 1992

[4] Garner, P.L; Meredith, P.T; and Stoner, R.C., Areas for Future CFD Development as Illustrated by Transport Aircraft Applications, AIAA Paper 91-1527; 1991

[5] Butter, D. J.; Recent Progress on Development and Understanding of High-Lift-Systems; AGARD-CP 365; 1984

[6] http://en.wikipedia.org/wiki/High-lift_device

[7] Introduction to the estimation of the lift coefficients at zero angle of attack and at maximum lift for aerofoils with high-lift devices at low speeds; ESDU 94026

[8] Kim, S.; Alonso, J.J.; Jameson, A.; Multi-element high-lift configuration design optimisation using viscous continuous adjoint method; Journal of Aircraft, Vlo.41,No.5; Sepermber-Octber,2004

[9] Rudolph, P.; High-Lift Systems on Commercial Subsonic Airliners; NASA-CR 4746; 1996

[10] Woodward, D.S.; Hardy, B.C.; and Ashill, P.R.; Some Types of Scale effect in Low-Speed High-Lift Flows; International Counsil of the Aeronautical Sciences Paper 88-4.9.3; 1988

[11] Smith, A.M.O.; High-Lift Aerodynamics; 37th Wright Bothers Lecture, Journal of Aircraft, Vol. 12, No. 6; 1975

[12] Sutcliffe, M.; Reckzeh, D.; Hicon Aerodynmics – High lift Aerodynmic Design for the Future; ICAS 2006

[13] http://blog.flightstory.net/268/airbuSA350-xwb-with-software-controlled-high-lift-flap

[14] Haines, A. B.; Scale Effects on Aircraft and Weapon erodynamics, AGARDOgraph 323; 1994

[15] Brune, G.W.; McMasters, J.H.; Computational Aerodynamics Applied to High-Lift Systems; Applied Computational Aerodynamics, Volume 125, Progress in Astronautics and Aeronautics; 1992

[16] Surface flow visualization in aircraft design; ESDU 03014

[17] Yuzuru.Yokokawa; Investigation of the flow over nacelle/pylon and wing controlled with a vortex generator in high lift configuration; ICAS 2008

[18] Reckzeh, D.; Aerodynamic Design of Airbus High-lift Wings in a Multidisciplinary Environment; ECCOMAS 2004

[19]. Johnson F.T, Tinoco E.N, Yu N.J; Thirty years of development and application of CFD at Boeing Commercial Airplanes, Seattle; Computers & Fluids 34 1115 – 1151 2005

[20] Kral LD. Recent experience with different turbulence models applied to the calculation of flow over aircraft components. Progress in Aerospace Sciences 1998; 34:481 – 541.

[21] Vosa J.B, Rizzib A., Darracqc D., Hirscheld E.H.; Navier – Stokes solvers in European aircraft design; Progress in Aerospace Sciences 38 (2002) 601 – 697

[22] Rumsey, C.L.; Ying, S.X.; Prediction of high lift: review of present CFD capability, Progress in Aerospace Sciences 38; 2002

[23] Godin, P., Zingg, D.W., Nelson, T.E.; High-lift aerodynamic computations with one- and two-equation turbulence models. AIAA J 1997, 35(2):237 – 43, Also AIAA Paper 96-0567; 1996

[24] Rumsey, C.L.; Gatski, T.B.; Ying, S.X.; Bertelrud, A.; Prediction of high-lift flows using turbulent closure models; AIAA J 1998,36(5):765 – 74, Also AIAA Paper 97-2260, 1997

[25] Tinoco E.N;Venkatakrishnan V.; Winkler C. ; Mani M.; Structured and Unstructured Navier–Stokes Solvers for the Third Drag Prediction Workshop; AIAA 2007-0255; 2007

[26] Moens,F.; Perraud, J.; Transition prediction and impact on 3D high-lift wing configuration; AIAA 2007-4302; 2007

[27] Crippa, S.; Melber-Wilkendingy, S. and Rudnik, R.; DLR Contribution to the First High Lift Prediction Workshop; AIAA 2011-938; 2011

[28] Frhr, H.; Geyr, v.1. and Schade, N.; CFD Prediction of Maximum Lift Effects on Realistic High- Lift-Commercial-Aircraft-Configurations within the European project EUROLIFT II; AIAA 2007-4299;2007

[29] Hirschel EH. Present and future aerodynamic process technologies at DASA military aircraft. ERCOFTAC Industrial Technology Topic Meeting, October 1999

[30] Lindblad I.A.A.; De Cock K.M.J.; CFD Prediction of maximum lift of a 2D high-lift configuration. AIAA Paper 99-3180; 1999

[31] Cebeci, T.; Shao, J. P.; Kafyeke, F.; Laurendeau, E.; Computational Fluid Dynamicsfor Engineers; 2005

[32] Argüelles,P.; Lumsden, J,; Bischoff, M.; EUROPEAN AERONAUTICS: A VISION FOR 2020; 2001

[33] Kiporous,T.; Multi-objective Aerodynamic design optimisation; Thesis for Doctor of Philosophy; Cambridge University; 2006

[34] Leovirijakit, K.; Jameson, A.; Aerodynamic shape optimisation of wings including planform variations; AIAA 2003-0210

[35] Kim,S.; Alonso, J.J.; Jameson,A.; Multi-element high-lift configuration design optimisation using viscous continuous adjoint method; Journal of Aircraft, Vlo.41,No.5; Sepember-Octber,2004

[36] Drive,J.; Zingg,D.W.; Numerical aerodynamic optimisation incorporating Laminar-Turbulent Transition Prediction; AIAA JOURNAL Vol.45, No.8; August 2007

[37] Zingg,D.W.; Elias, S.; Aerodynamic optimisation under a range of operating conditions; ; AIAA JOURNAL Vol.44, No.11; November 2007

[38] Peigin, S.; Epstein, B.; Multiconstrained aerodynamic design of business jet by CFD driven optimisation tool; Aerospace Science and Technology, 12 2008

[39] Vankan,W.J.; Lammen,W.; Maas, R.; Meta-modeling and Multi-objective Optimisation in Aeronautical MDO; Advances in Collaborative Civil Aeronautical Multidisciplinary Design Optimisation; Volume 233, PROGRESS IN ASTRONAUTICALS AND AERONAUTICS; 2010

[40] Parks,G.T.; Linear Algebra-Optimisation; Lecture Notes; Module 4M13; Cambridge University; Engineering Department; 2002

[41] Giannakoglou, K.C.; Design of optimal aerodynamic shapes using stochastic optimisation methods and computational intelligence; Progress in Aerospace Sciences 38 (2002) 43 – 76.

[42] Namgoong, H.; Crossley, W. A.; and Lyrintzis, A. S.; Global optimization issues for transonic airfoil design; AIAA 2002-5641;2002

[43] Parks,G.T.; Stachastic Process and Optimisations Methods; Lecture Notes; Module 5R1; Cambridge University; Engineering Department; 2003

[44] Jones, D.F.; Mirrazavi, S.K.; Tamiz, M.; Multi-objective meta-heuristics: An overview of the current state-of-the-art; European Journal of Operational Research 137 (2002) 1 – 9; 2002

[45] Jaeggi, D.M.; Parks, G.T.; Kipouros, T. P.; Clarkson, J; The development of a multi-objective Tabu Search algorithm for continuous optimisation problems; European Journal of Operational Research 185 (2008) 1192 – 1212; 2008

[46] Giuseppe Trapani; Multi-Objective Optimisation of 2D High-Lift Airfoil Configurations using Tabu Search; MSc Thesis; 2009

[47] Van den Berg, Gooden,J.H.M.; Low speed surface pressure and boundary layer measurement data for the NLR 7301 airfoil section with trailing edge flap;1979

[48] Arlinger, B.G,; Larsson, T.; NLR 7301 two-element airfoil at high lift. In: Haase, W; Chaput, E.; Elsholz, E.; Leschziner, M.A; Muller, U.R. editors. ECARP—European Computational Aerodynamic Research Project, validation of CFD codes and assessment of turbulence models; Notes on numerical fluid mechanics (NNFM), vol. 58. Braunschweig: Vieweg; 1997. p. 375 – 96; 1997

[49] Arnold F, Thiele F. LaPlace interaction law for the computation of viscous airfoil flow in low- and highspeed aerodynamics. AIAA J 1994;31(11):2178 – 85; Also AIAA Paper 93-3462

[50] Cantariti, F.J.J; Johnston, L.J.; High-lift Navier-Stokes computations on unstructured grids using a differential Reynolds stress model. In: Morton K.W.,

Baines MJ, editors. Numerical Methods for Fluid Dynamics V. Oxford, UK: Clarendon Press, 1995. p. 319 – 25.;

[51] Cantariti, F.J.J; Johnston, L.J.; Analysis of high-lift system aerodynamics using an unstructured flow solver and differential Reynolds stress modelling. Proceedings of the Seventh Biennial Colloquium on Computational Fluid Dynamics, University of Manchester Institute of Science and Technology, UK, May 1996. p. 3.7 – 3.8.

[52] Cao HV, Kusunose K. Grid generation and Navier – Stokes analysis for multi-element airfoils. AIAA Paper 94-0748, January 1994.

[53] Cebeci T. Calculation of multielement airfoils, wings at high lift. AGARD CP-515, September, 1993. p. 24.1 – 24.15.

[54] Cebeci T, Besnard E, Chen HH. An interactive boundarylayer method for multielement airfoils. Comput Fluids 1998;27(5 – 6):651 – 61.

[55] Fritz W. Calculation of maximum and high lift characteristics of multi element airfoils. AGARD CP-515, September, 1993. p. 5.1 – 5.12.

[56] Godin P, Zingg DW, Nelson TE. High-lift aerodynamic computations with one- and two-equation turbulence models. AIAA J 1997;35(2):237 – 43; Also AIAA Paper 96- 0567, January 1996

[57] Jahangirian AR, Johnston LJ. Calculation of high-lift aerodynamics on adaptive unstructured grids. International Council of the Aeronautical Sciences Proceedings, 20th Congress, vol. 2. Reston, VA: AIAA, 1996. p. 2221 – 31.

[58] Jasper DW, Agrawal S, Robinson BA. Navier – Stokes calculations on multi-element airfoils using a chimerabased solver. AGARD CP-515, September, 1993. p. 8.1 – 8.11.

[59] Johnston LJ, Stolcis L. Prediction of the high-lift performance of multi-element aerofoils using an unstructured Navier-Stokes solver. AGARD CP-515, September, 1993. p. 13.1 – 13.18.

[60] Kim CS, Kim C, Rho OH. Parallel computations of highlift airfoil flows using two-equation turbulence models. AIAA J 2000;38(8):1360 – 8; Also AIAA Paper 99-0542, January 1999.

[61] Kusunose K, Cao HV. Prediction of transition location for a 2-d Navier – Stokes solver for multi-element airfoil configurations. AIAA Paper 94-2376, June 1994.

[62] Kusunose K, Wigton L, Meredith P. A rapidly converging viscous/inviscid coupling code for multi-element airfoil configurations. AIAA Paper 91-0177, January 1991.

[63] Larsson T. Separated and high-lift flows over single and multi-element airfoils. International Council of the Aeronautical Sciences Proceedings, 19th Congress, vol. 3. Reston, VA: AIAA, 1994. p. 2505 – 18.

[64] Nelson TE, Godin P, Zingg DW. Multi-element airfoil computations with one-equation turbulence models. AIAA Paper 95-0357, January 1995.

[65] Murayama,M.; Yamamoto, K. and Kobayashi, K.; Validation of Flows on High-Lift Configurations by Structured- and Unstructured- Mesh Method; AIAA 2005-1226; 2005

[66] Zingg D.W.; Godin P.; A perspective on turbulence models for aerodynamic flows; International Journal of Computational Fluid Dynamics;2009

[67] Anderson J.D.; Computational Fluid Dynamics; Mcgraw-Hill International Editions; 1995

[68] http://www.kxcad.net/STAR-CCM/online/139-kEpsilonTurbulence-07.html

[69] Murayama M.; Imamura T.; Yamamoto K.; Kobayashi K.; Comparison of Reynolds Averaged Navier-Stokes Simulations of Multi-Element High- Lift Configurations; Journal of Aircraft; 44 No.1 January-February 2007

[70] http://geolab.larc.nasa.gov/APPS/YPlus/

[71] http://www.cranfield.ac.uk/it/cranfield/stateofart/page8652.html

Appendix A

Coordinates of NLR7301& Flap

Table 17 Coordinates of main element

x	y
0.94360	0.01499
0.94267	0.01519
0.93988	0.01580
0.93524	0.01690
0.92878	0.01830
0.92051	0.02008
0.91047	0.02241
0.89870	0.02512
0.88524	0.02819
0.87015	0.03162
0.85349	0.03536
0.83532	0.03941
0.81572	0.04368
0.79476	0.04814
0.77253	0.05273
0.74911	0.05735
0.72459	0.06191
0.69908	0.06628
0.67267	0.07038
0.64547	0.07410
0.61758	0.07737
0.58912	0.08015
0.56019	0.08248
0.53092	0.08438
0.50141	0.08590
0.47178	0.08704
0.44216	0.08781
0.41265	0.08826
0.38337	0.08838
0.35444	0.08818
0.32598	0.08768

Table 17 Coordinates of main element (continued)

0.29809	0.08687
0.27098	0.08577
0.24448	0.08440
0.21897	0.08276
0.19445	0.08087
0.17103	0.07874
0.14880	0.07638
0.12784	0.07381
0.11786	0.07245
0.10824	0.07103
0.09897	0.06958
0.09007	0.06807
0.08155	0.06650
0.07341	0.06488
0.06567	0.06317
0.05832	0.06137
0.05139	0.05943
0.04487	0.05731
0.03877	0.05506
0.03309	0.05268
0.02786	0.05009
0.02305	0.04717
0.01870	0.04373
0.01479	0.03978
0.01133	0.03544
0.00832	0.03076
0.00577	0.02582
0.00368	0.02064
0.00206	0.01516
0.00089	0.00959
0.00019	0.00422
-0.00004	-0.00080
0.00019	-0.00552
0.00089	-0.00992
0.00206	-0.01417
0.00368	-0.01804
0.00577	-0.02173
0.00832	-0.02521
0.01133	-0.02851
0.01479	-0.03158
0.01870	-0.03445

Table 17 Coordinates of main element (continued)

0.02305	-0.03717
0.02786	-0.03972
0.03310	-0.04215
0.03877	-0.04443
0.04487	-0.04661
0.05139	-0.04873
0.05832	-0.05073
0.06567	-0.05263
0.07341	-0.05446
0.08155	-0.05622
0.09007	-0.05791
0.09897	-0.05954
0.10824	-0.06109
0.11786	-0.06259
0.12784	-0.06402
0.14880	-0.06672
0.17103	-0.06917
0.19445	-0.07132
0.21897	-0.07317
0.24448	-0.07470
0.27089	-0.07585
0.29809	-0.07666
0.32598	-0.07704
0.35444	-0.07701
0.38337	-0.07652
0.41265	-0.07550
0.44216	-0.07385
0.47178	-0.07144
0.50141	-0.06819
0.53092	-0.06417
0.56019	-0.05959
0.58912	-0.05459
0.61758	-0.04921
0.64547	-0.04355
0.67267	-0.03750
0.69908	-0.03080
0.72459	-0.02362
0.74911	-0.01597
0.77253	-0.00824
0.79476	-0.00080
0.81572	0.00585

Table 17 Coordinates of main element (continued)

0.83532	0.01115
0.85349	0.01472
0.87015	0.01702
0.88524	0.01818
0.89870	0.01843
0.91047	0.01807
0.92051	0.01733
0.92878	0.01645
0.93524	0.01530
0.93988	0.01460
0.94267	0.01423
0.94360	0.01410

Table 18 Coordinates of flap

x	y
1.205092	-0.102133
1.204014	-0.101411
1.200754	-0.099373
1.195420	-0.095931
1.188106	-0.091056
1.178790	-0.085249
1.167564	-0.078726
1.154588	-0.071662
1.140013	-0.064282
1.124077	-0.056694
1.106992	-0.049135
1.098093	-0.045428
1.088996	-0.041798
1.079729	-0.038286
1.070330	-0.034929
1.060832	-0.031728
1.051260	-0.028701
1.041673	-0.025861
1.032094	-0.023205
1.022570	-0.020749

Table 18 Coordinates of flap (continued)

1.013137	-0.018508
1.003821	-0.016532
0.994643	-0.014820
0.985653	-0.013410
0.976874	-0.012269
0.968366	-0.011407
0.960148	-0.010799
0.952264	-0.010473
0.944743	-0.010407
0.937624	-0.010583
0.930955	-0.010922
0.924783	-0.011390
0.919139	-0.011985
0.914029	-0.012722
0.909442	-0.013659
0.905415	-0.014812
0.901946	-0.016156
0.899047	-0.017719
0.896720	-0.019522
0.895009	-0.021474
0.893925	-0.023517
0.893589	-0.025374
0.893925	-0.027199
0.894976	-0.028901
0.896887	-0.030054
0.899614	-0.030749
0.903046	-0.031232
0.907107	-0.031741
0.911738	-0.032320
0.916920	-0.032993
0.922644	-0.033757
0.928889	-0.034582
0.935621	-0.035469
0.942821	-0.036418
0.950452	-0.037440
0.958495	-0.038526
0.966901	-0.039670
0.975646	-0.040906
0.984677	-0.042203
0.993974	-0.043586

Table 18 Coordinates of flap (continued)

1.003479	-0.045045
1.013157	-0.046609
1.022976	-0.048257
1.032883	-0.050011
1.042829	-0.051865
1.052791	-0.053820
1.062706	-0.055875
1.072539	-0.058038
1.082262	-0.060300
1.091824	-0.062652
1.101185	-0.065091
1.119166	-0.070188
1.135943	-0.075465
1.151267	-0.080787
1.164948	-0.085915
1.176820	-0.090662
1.186673	-0.094993
1.194459	-0.098572
1.200104	-0.101159
1.203556	-0.102670
1.204699	-0.103214

Appendix B

A sensitive G3 case of K-ω SST model simulation

This sensitive G3 is very close to the final G3 but converge at an unreasonable state which introduces large discrepancy compared to the experiment. Figure 87 shows the comparison of velocity vectors around the trailing edge of main element and flap between sensitive G3 case and final G3 case which reveals clearly the thicker boundary layer on the upper surface of main element and heavier velocity losses internal of the boundary layer can be found in sensitive G3 case. Figure 88 and Figure 89 show the comparison of the Cp between sensitive G3 case and final G3 case. Figure 90 shows the comparison of Cf. Finally a much lower CL=3.034 and a much higher CD=0.07021 have been predicted by this high sensitive G3 case.

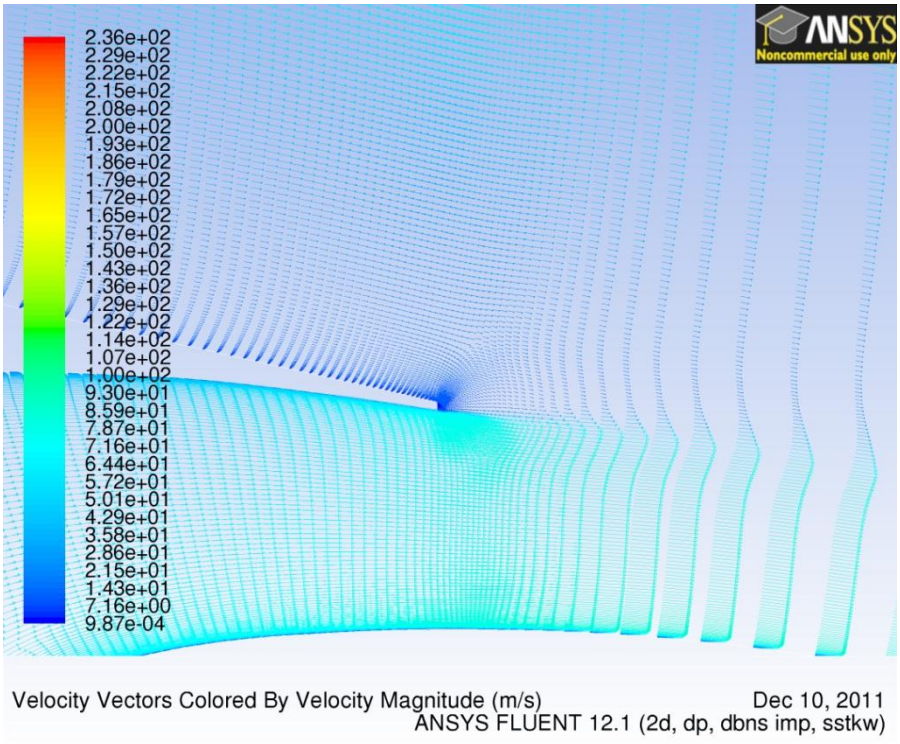

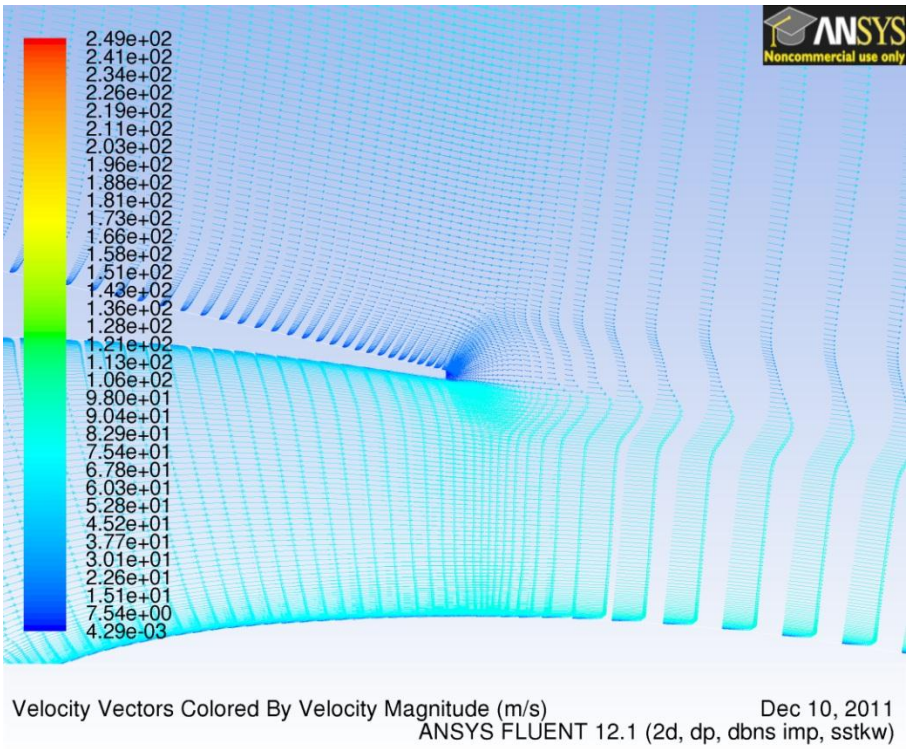

Figure 87 Comparison of the velocity vectors between sensitive G3 (upper one) and final G3 (lower one)

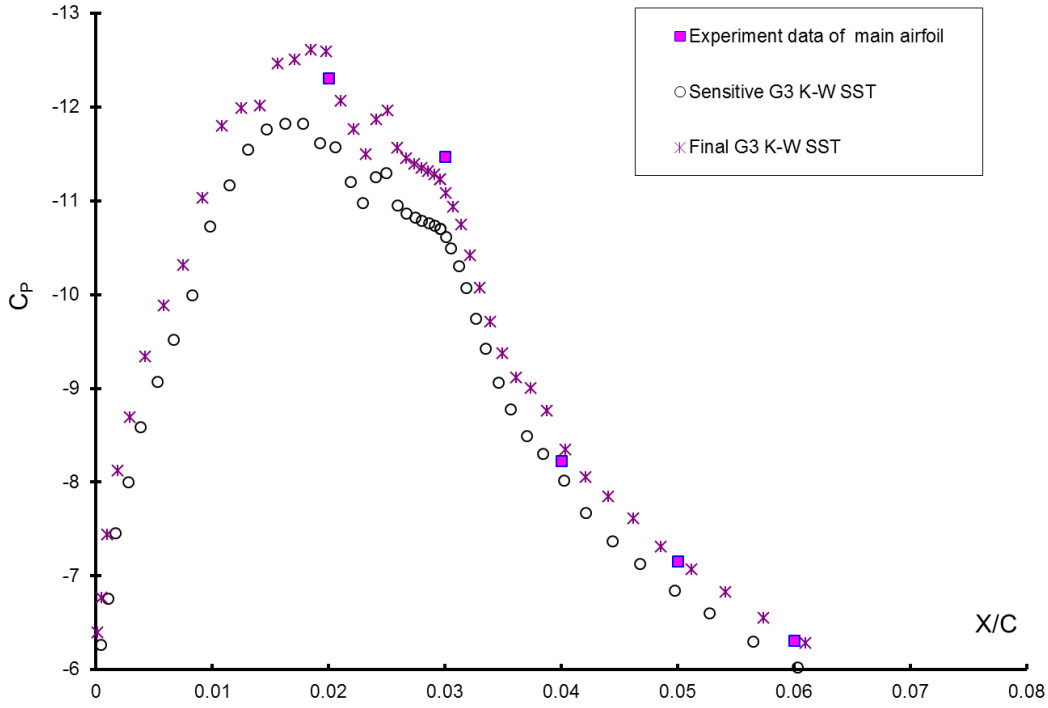

Figure 88 Comparison of the leading edge Cp between sensitive G3 and final G3

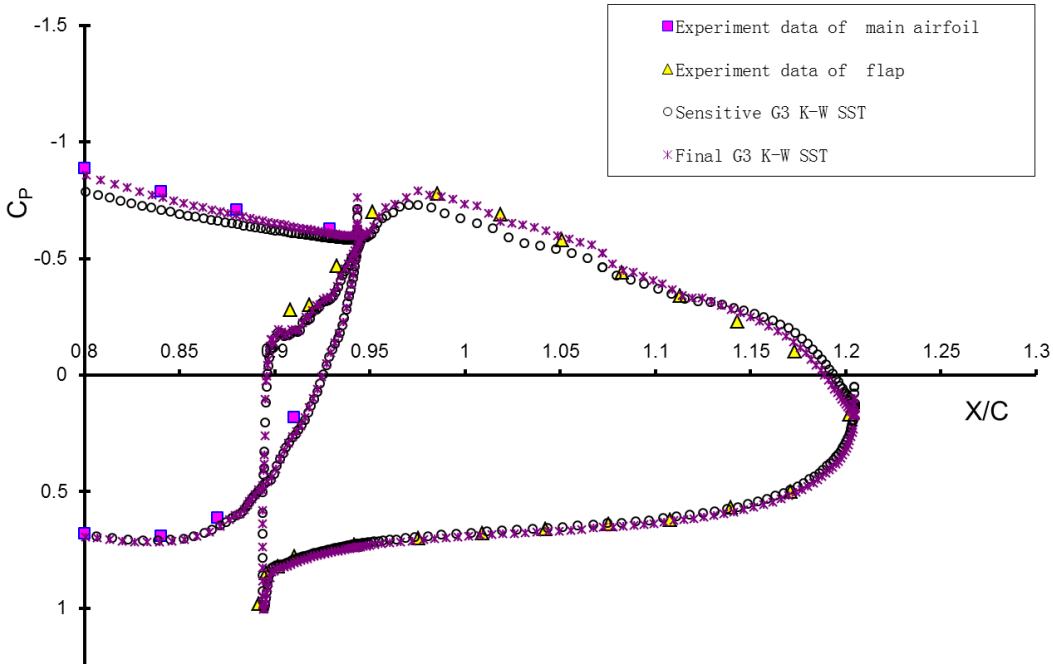

Figure 89 Comparison of Cp around flap between sensitive G3 and final G3

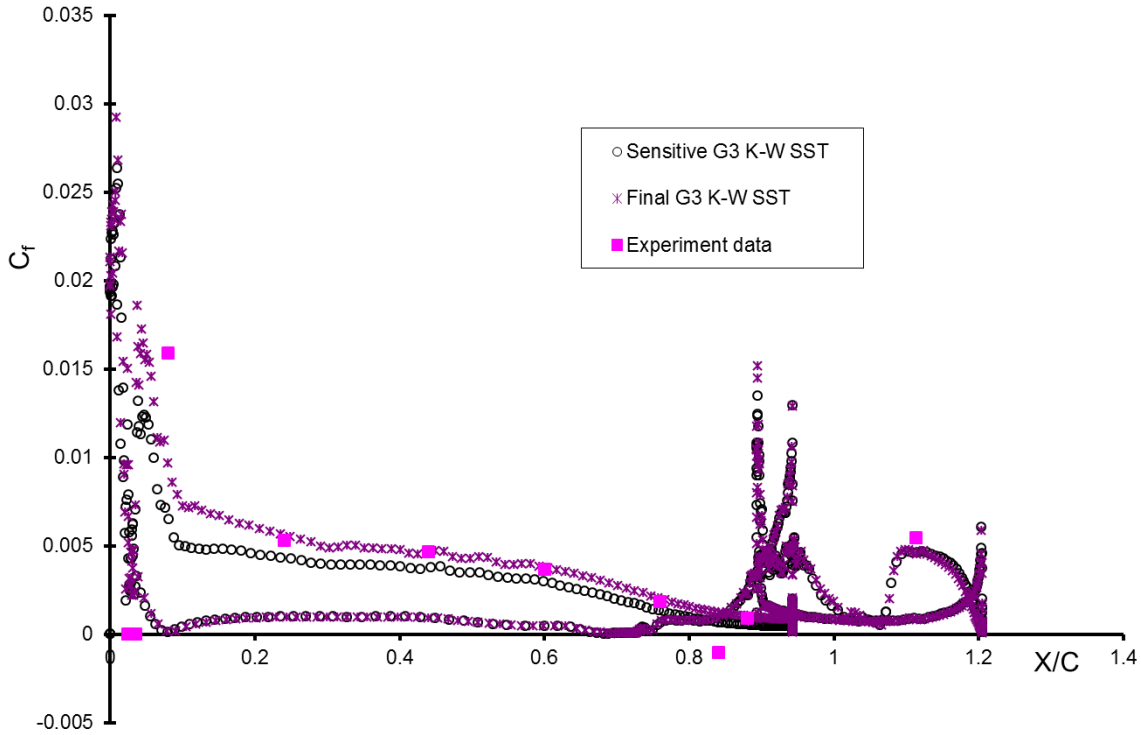

Figure 90 Comparison of Cf between sensitive G3 and final G3